UNIVERSITÀ DEGLI STUDI DI PADOVA

Dipartimento di Ingegneria Industriale

Corso di Laurea in Ingegneria Aerospaziale

Tesi di Laurea Magistrale

Aerodynamic and structural design of some components of an ultralight aircraft

Relatore
Prof. Ugo Galvanetto

Correlatori
Prof. Mirco Zaccariotto
Ing. Francesco Picano

Laureando
Matteo Scalchi
Matr. N° 1040030

Anno Accademico 2013/2014

Contents

Introduction

The work presented in this thesis focuses on the design layout and analysis of some components of the "Merlo", an experimental ultralight aircraft conceived by Professor Marco Sambin at the University of Padova. Although he is not an engineer, professor Sambin has a lifetime experience as a pilot of light aircrafts and gliders. In addition, he recently deepened his knowledge of aircraft construction, and he applies to this subject with creativity and passion. On this work, some of Sambin's ideas have been put to the test with analytical calculations and computer-aided design and analysis.

Merlo's layout

The Merlo has been conceived to be a very light one-seat plane, much lighter than the majority of one-seat ultralights on the market today. It must be safe and easy to handle, and its construction easy enough so that most of the building and assembling phases can be carried out in a homemade laboratory by one person (professor Sambin himself). In addition, it must be easily transported from the place where it is kept to the flying field with a common van. In order to do this, the wings must be detachable, keeping the maximum safety conditions during flight and landing.
The majority of Merlo's parts are built using composite materials to achieve maximum structural performance with low weight. For the inner structure of the wings the choice has been wood, which can be easily crafted "at home". Aluminum and other metals have been used for the landing gear and other small parts.

Previous works

The Merlo aircraft has already been investigated in three previous works. Ferus [10] did some preliminary sizing, mostly following Anderson's *Aircraft performance design* [3]. In his work, some cfd simulations have been carried out, then the wing structure has been analyzed with a FEM software, using the flight envelope to calculate the critical loads in different phases of the flight.
Baldon [7] examined the composite fuselage structure, modeled it with a FEM software

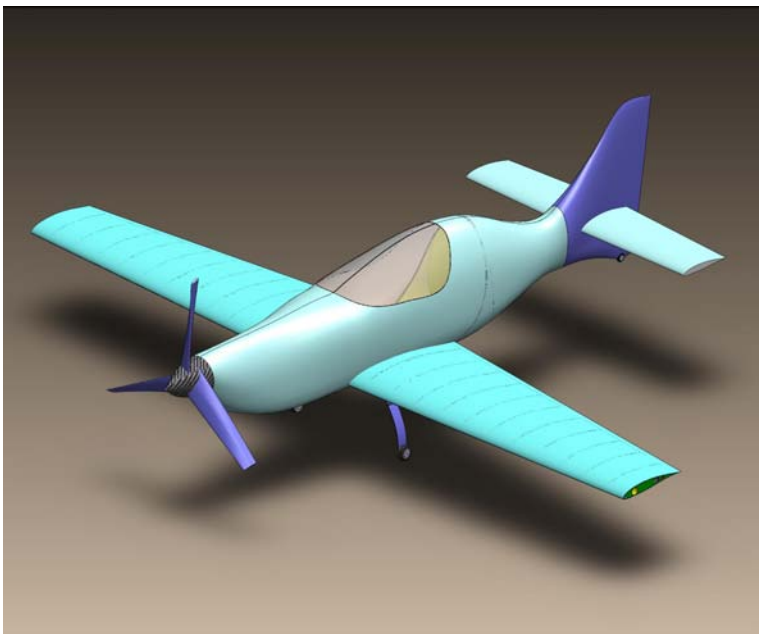

An early sketch of Merlo, by Ferus [10]

and showed some different solutions for the fuselage design.
Gori [13] analyzed the structure of some parts of the aircraft, including the motor mount, the landing gear and the control system. In his work, three different engine mounts have been validated and solid pipe landing gear has been designed.
After these three works, professor Sambin adopted some major changes to the wing structure and material design, and proposed to investigate a more flexible solid spring landing gear.

Purposes of the present work

In the first chapter, the wing geometry and structure has been presented, drawn with the CAD software SolidWorks® and the software for model aircraft builders Profili2®. The wing relevant parameters have been calculated, and a first sizing of the tail has been carried out. The minimum margin between the aircraft center of gravity and the aerodynamic center has been calculated to grant the longitudinal stability of the aircraft. A new flight envelope has been drawn, following the normative, and the coordinates of the relevant points have been found. The stability of the aircraft in different conditions has been investigated, calculating the required loads at wings and tails. A gliding performance estimate has been presented, calculating the maximum gliding ratio of the aircraft.

Again, SolidWorks have been used to create geometries for the models that have been inserted in the cfd and structural simulations. A new aerodynamic analysis on wings and tail has been carried out, using Ansys Workbench® and the FLUENT® solver. The results have been analyzed and then the pressure distribution has been exported into to a FEM structural analysis, using ANSYS® Mechanical APDL interface.
In the second chapter, the structure layout is presented. A 3D model of the inner structure of the wing and of the wingtip has been drawn with SolidWorks. The materials chosen for the construction of Merlo have been described, and their choice has been justified. An analytical calculation has been carried out to obtain a first size of the main spar. Then, a detailed finite elements analysis has been done with the APDL interface. All the phases of the analysis have been presented in detail, and the results have been presented and commented. The results have brought to an accurate sizing of the wing main structural components, including the spars, the ribs and the skin.
In the third chapter, a new landing gear has been designed. First, the requirements of the shock-absorbing system have been described. The tires have been sized, and the geometry of the landing gear has been presented, based on landing gears that are already used by commercial ultralight aircraft. Two landing gear geometries have been sized with analytical calculations. A first finite element analysis led to the choice of one of the two geometries discussed. Then, a more accurate model of the selected landing gear has been done, and a non-linear static structural fem analysis has been done to optimize the design of the landing gear leg. Finally, the fatigue life of the landing gear leg has been estimated with an analytical method.
The fourth and last chapter regards the conclusions of this work and the possible future developments.
The author of the present work attempted to give a clear explanation of all the calculations that have been carried out, in order to give reader the possibility to understand not only the mathematics, but also the method and the solution of practical problems found on the way. In particular, since the project in which this work is included will not be over after the analysis that is presented here, the aim is to give to future students that will join the project the instruments to start their work properly, without the need of re-doing calculations that have been badly explained. The details of the numerical simulation are reported in the appendix, and the codes are commented for a more immediate understanding.
The layout of this work has been done with LaTeX[1], the open source typesetting system. All the figures, except where indicated, have been created by the author. To modify the bitmap files, the basic MS Paint has been used. For vector graphics sketches, very good results have been obtained with the open source software Inkscape[2].

[1] www.latex-project.org
[2] www.inkscape.org

Chapter 1

Aerodynamic analysis

In this chapter, a complete new design for Merlo's wings and tail is described. Most of the design followed Professor Sambin's guidelines, which have been integrated with the study of some specific books on aerodynamics and airplane design. First, the sizing phase of wings and tail is presented and the complete wing layout is reported. The flight envelope for the Merlo has been investigated, and a relation has been found between the limit load and the angle of attack of the aircraft. Then, an estimate of gliding performance has been carried out, predicting the drag coefficients by analytical calculations. Finally, a cfd analysis has been carried out in order to investigate some flight conditions taken from the $V - n$ diagram in which the worst load cases are expected.

1.1 Geometry

1.1.1 Airfoils and wing geometry

Merlo has been conceived to be a very small airplane. Actually, it measures $4m$ from the nose (the propeller edge) to the end of the vertical tail. The total wing span measures $5m$, and the fuselage width at the wing location is about $0.6m$, so that the effective lenght of a single wing is $2.2m$. Two different airfoils has been chosen for the wing (effective) root and the tip. The effective wing root, in the present work, is assumed to be the section created by the intersection of fuselage and wing, located at $300mm$ from the aircraft plane of simmetry. Although this is the real wing root, the aerodynamic calculations consider the imaginary wing root at the center of the fuselage (the literature defines "wing root" this imaginary airfoil at the aircraft's plane of simmetry [24]).
The HQ airfoil family has been the choice of Prof. Sambin. These airfoil have been designed properly for sailplanes by Helmut Quabeck [15], and match Sambin's ideas for the inner structure of the wing. For the effective wing root, a HQ $3.5/10$ with a chord of $800mm$ has been selected. The code means that the airfoil has a maximum thickness

of 10% at the 35% of the chord length, and a maximum camber of 3.5% at the 50% of the chord length. For the tip, a HQ $3.5/12$ with a chord of $433mm$ has been chosen. The airfoil at the tip is slightly thicker in order to leave more space for the wing spars. The wing is swept afterward so that the leading edge for the airfoil located at $1800mm$ from the effective wing root is $200mm$ after the root leading edge. This leads to a leading edge sweep angle of

$$\Lambda_{LE} = tan^{-1}\frac{200}{1800} = 6.34^{\circ} \tag{1.1.1}$$

The tip airfoil is rotated by a negative angle of 2°: the wing is twisted in order to prevent tip stall when close to the stall angle. In other words, the root section enters the stall condition before the tip section. A tip stall leads to a very unstable behavior of the aircraft, making it very difficult to be recovered. If the stalls occurs first at the root, then it is much more controllable, and the aircraft may be easily recovered by a skilled pilot.
In addition, the wing has a dihedral angle of 2°. The dihedral is the wing angle with respect to the horizontal when the airplane is seen from the front. A positive dihedral increases roll stability during turns and turbulences.
The aircraft has a low-wing configuration, so the wing is located approximately at $100mm$ to the fuselage floor. The wing is mounted with a 2° incidence. This means that during level flight (or cruise phase) the root will have a 2° attack angle, while the tip will have a zero angle of attack.
The wing has only one control surface that grants the attitude control and the required variations of lift coefficient. For simplicity, instead of a separate aileron-flap configuration, the functions of these two control surfaces have been summed into only one "flaperon".

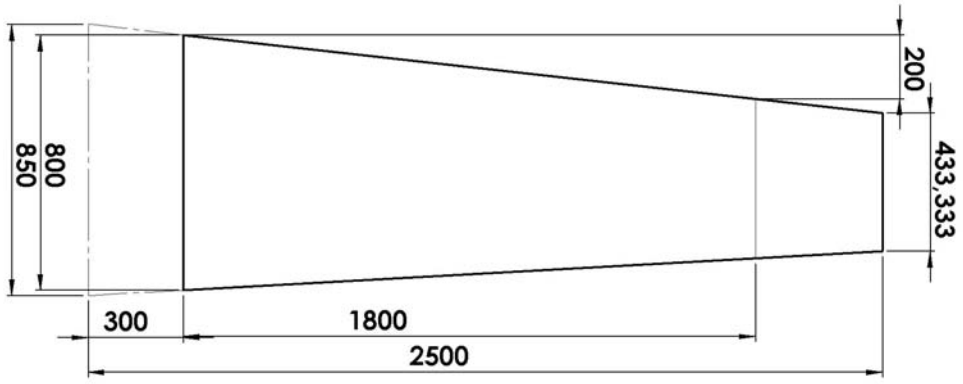

Figure 1.1: Wing geometry and dimensions.

1.1.2 Calculation of relevant parameters

As mentioned above, the common formulas for aerodynamic calculations consider the root chord at the center of the fuselage. This one can be related to the effective wing root and the wing tip by the following proportion:

$$\frac{C_{ER} - C_T}{L_{ER,T}} = \frac{C_R - C_T}{L_{R,T}} \tag{1.1.2}$$

where C_{ER}, C_R and C_T are respectively effective root, root (at center of the fuselage) and tip chord lengths. $L_{ER,T} = 2.2m$ and $L_{R,T} = 2.5m$ are the distances of the effective root and the root to the wing tip. The equation above, for C_R gives:

$$C_R = \frac{C_{ER} - C_T}{L_{ER,T}} L_{R,T} + C_T = 850mm \tag{1.1.3}$$

With this value, the wing reference area can be calculated:

$$S = \frac{C_R + C_T}{2} b = 3.208m^2 \tag{1.1.4}$$

where b is the total wing span. Once the reference area is found, the aspect ratio can be calculated:

$$AR = \frac{b^2}{S} = 7.79 \tag{1.1.5}$$

The taper ratio is the ratio between the tip and root chord lengths:

$$\lambda = \frac{C_T}{C_R} = \frac{433}{850} = 0.51 \tag{1.1.6}$$

The taper affects the lift distribution along the wingspan. For a taper ratio of about 0.5, the drag of the wing due to lift is very close to the value related to a perfect elliptical lift distribution, which the Prandtl finite wing theory indicates as the optimal distribution in order to minimize drag due to lift [4].

Now, the position of the aerodynamic center of the wing may be found. The aerodynamic center of an airfoil is the point where the aerodynamic forces (Lift and Drag) are applied creating a pitching moment that does not vary with the lift coefficient. For subsonic speeds, its position is very close to the quarter-chord point. For an entire wing, the aerodynamic center (also called neutral point) is assumed to be at a quarter of the mean aerodynamic chord. Calculations for aircraft stability require to know its exact location with respect to the root airfoil chord. At this purpose, Raymer [24] presents a formula and a graphical approach (figure 1.2) to find the mean aerodynamic airfoil of a trapezoidal wing.

The mean aerodynamic chord length is given by

$$\bar{C} = \frac{2}{3} C_R \frac{1 + \lambda + \lambda^2}{1 + \lambda} = 664.3mm \tag{1.1.7}$$

The mean aerodynamic chord is located at a distance $\bar{Y}$ from the plane of symmetry of the aircraft:

$$\bar{Y} = \frac{b}{6}(1+2\lambda)(1+\lambda)^{-1} = 1114.8mm \tag{1.1.8}$$

To position the wing correctly, it is necessary to obtain the position of the aerodynamic center with respect to the effective root chord. The distance from the e.r. leading edge is given by:

$$x_{ac} = \frac{\bar{C}}{4} + (\bar{Y} - 300)tan(\Lambda_{LE}) = 256.6mm \tag{1.1.9}$$

The result is confirmed by the graphical approach presented in figure 1.2.

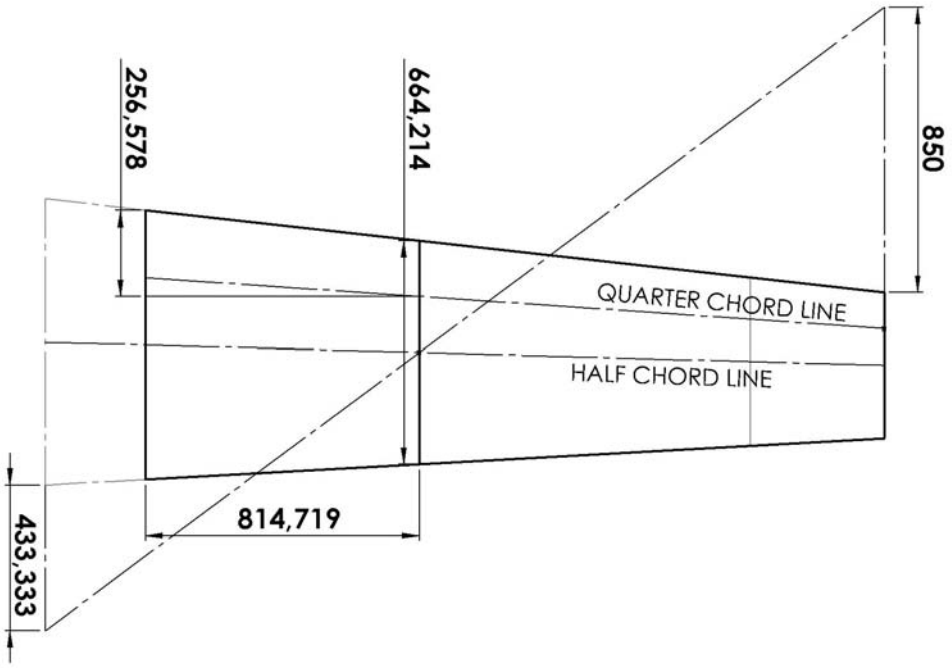

Figure 1.2: Graphical method for finding the aerodynamic center of the wing.

1.1.3 Tail sizing

The tail is designed to balance the moments produced by the wing, stabilizing the aircraft in the vertical and horizontal plane. Thus, the tail dimensions must be derived from the wing ones. Since there is not a unique method for tail sizing, the calculation must rely on historical data. Here, Raymer's tail volume coefficient method has been followed to obtain an initial estimation of tail surfaces ([24], chapter 6, paragraph 4).

Tail volume coefficients are two non-dimensional parameters, c_{VT} for the vertical tail and c_{HT} for the horizontal, defined by:

$$c_{VT} = \frac{L_{VT} S_{VT}}{bS} \tag{1.1.10}$$

$$c_{HT} = \frac{L_{HT} S_{HT}}{\bar{C} S} \tag{1.1.11}$$

where L_{VT} and L_{HT} are respectively the vertical and horizontal tail arms, that means approximately the distance between wing aerodynamic center and tail quarter-chord points. S_{VT} and S_{HT} are the tail reference surfaces, which are to be calculated. $\bar{C}$ is the wing mean chord, as calculated above.
Tail volume coefficient are chosen among the typical values provided by Raymer. For this case, "homebuilt" category coefficients $c_{VT} = 0.04$ and $c_{HT} = 0.5$ have been chosen. From the definition of tail volume coefficients, tail reference areas are calculated, assuming an initial estimate of $L_{VT} = 2.2m$ and $L_{HT} = 2.1m$.

$$S_{VT} = \frac{c_{VT} bS}{L_{VT}} = 0.314m^2 \tag{1.1.12}$$

$$S_{HT} = \frac{c_{HT} \bar{C} S}{L_{VT}} = 0.572m^2 \tag{1.1.13}$$

Merlo's tail configuration is absolutely "conventional". The airfoil selected from professor Sambin is a symmetric airfoil from the HQ family, the HQ$0/10$. It has a maximum thickness of 10% at 33.9% of the chord. The tail total span is $b_T = 1.6m$, with a root chord length of $c_{Tr} = 500mm$ and a tip chord length of $c_{Tt} = 400mm$. This leads to a taper ratio of $\lambda_T = 0.8$, and a total surface of $S_T = 0.72m^2$, which is approximately $0.15m^2$ more than the calculated value, taken as a safety margin.
Tail position with respect to the wing is defined as the vertical and horizontal distance from the wing aerodynamic center to the tail a.c., which can be approximated as the quarter-chord point of the tail root chord. The horizontal distance has been already defined above with the tail moment arms L_{VT} and L_{HT}. The vertical distance of the horizontal tail a.c. is $H_{VT} = 150mm$.

1.1.4 Stability margin

The wing must be carefully positioned with respect to the aircraft center of gravity. For stability, the aerodynamic center must lie behind the center of gravity. The horizontal distance between the c.g. and the a.c. with respect to the mean aerodynamic chord is called static margin:

$$s_m = \frac{x_{AC} - x_{CG}}{\bar{C}} \tag{1.1.14}$$

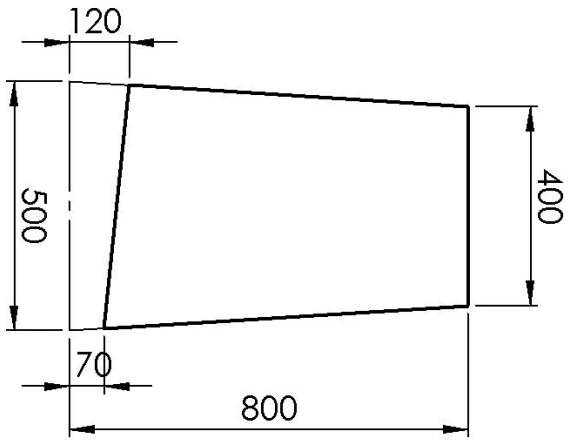

Figure 1.3: Horizontal tail geometry and dimensions.

where x_{AC} and x_{CG} are distances taken from an arbitrary point of the aircraft. In Merlo's case, they are taken from the tip of the propeller spinner.
Since the location of the center of gravity moves afterward during flight, mostly because of the consumption of fuel (which is stored in the front of the airplane), a minimum margin of stability must be set considering the most aft c.g. location. Anderson ([3], paragraph 8.6.7) suggest a safety value of 10% of the mean aerodynamic chord length. In this way, the minimum distance between the c.g. and the a.c. can be estimated:

$$x_{AC} - x_{CG} = 0.1\bar{C} = 66.4mm \approx 70mm \tag{1.1.15}$$

1.2 The flight envelope

1.2.1 Definition and regulations

The wing of an aircraft is the component which carries the greatest air loads, so it is necessary to verify the strength of the structure when the maximum expected loads are applied. The different load condition that an aircraft may meet during flight are represented in a chart called flight envelope, or $V - n$ diagram. This diagram reports the limit load factors as a function of the aircraft speed. Load factor n is defined as the ratio between the lift L generated by the wings during a particular maneuver and the aircraft maximum weight W. Thus, the limit load factor is a measure of the acceleration that the aircraft must be able to withstand during different flight conditions. The $V-n$ diagram can be interpreted as a boundary into which the aircraft must be able to operate in total safety. During the design of the aircraft structure, only a few points located at the boundary are investigated, since these points represent the worst load condition. If

the aircraft survives to them with a good safety margin, then it will be able to flight in every other condition inside the boundary.
The boundary points in the flight envelope are defined by the two coordinates, (V_i, n_i). These coordinates are given by the aviation regulations, with respect to the type of aircraft and its operative function. In Italy, the present normative is given by the DPR n.133[1] [8], which is inspired to the American Federal Aviation Regulations (FAR) [9]. In particular, the flight envelope is defined at paragraphs 321-341 of the DPR n.133 (which corresponds to the FAR part 23).
Since the load factor varies with the effect of compressibility, a flight envelope is given for a specific altitude: if the aircraft is designed to operate at different altitudes, more than one flight envelope must be examined. However, assuming that an ultralight aircraft will not operate at very high altitudes, the DPR n.133 allows to investigate only the flight envelope at altitude $0m$.

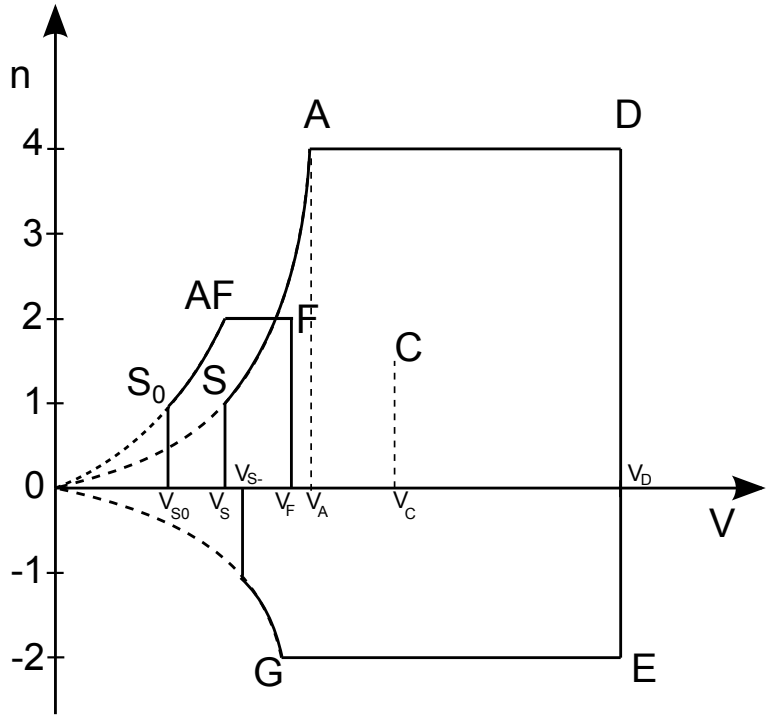

Figure 1.4: Flight envelope for advanced ultralights, presented in DPR n.133

With regard to the diagram in figure 1.4, the structure must be verified under load conditions at points A, D, E, G, F. Since the distribution of the air loads on wings will be

[1] Decreto del presidente della Repubblica, 9 luglio 2010, n. 133. Nuovo regolamento di attuazione della legge 25 marzo 1985, n. 106, concernente la disciplina del volo da diporto o sportivo.

calculated with a cfd software, it is important to understand which inputs is necessary to give to the simulation in order to obtain the particular conditions (V_i, n_i). Airspeed is already a typical condition that must be set when modeling a cfd simulation; on the other hand, the load factor n is not directly related to the fluid flow. Thus, it is necessary to relate the load factor to another variable that can be controlled in the preprocessing phase. This variable can only be the wing angle of attack, which, at a given Reynolds number, implies a wing coefficient of lift C_L. For a given coefficient of lift, the lift produced by the wing is calculated with the basic aerodynamic relation:

$$L = \frac{1}{2}\rho V^2 S C_L \tag{1.2.1}$$

thus, the load factor is simply obtained as $n = L/W$. This procedure will be used later to obtain the wing angle of attack when setting up the cfd simulation.

1.2.2 Lift and Drag polars

The procedure above requires that a relation between the lift coefficient and the wing angle of attack is known. The best way to calculate this relation is to test a wing model in a wind tunnel; however, it requires advanced instrumentations and takes a lot of time to set up the experiment and to calculate the results. In this work an approximate method is used, based on the lift and drag diagrams obtained from the airfoils with the help of the software Profili2© [22]. It is a software conceived for model builders, and among other functions has a procedure to calculate the lift and drag polars of any given airfoil[2]. The airfoils considered were the root airfoil HQ $3.5/10$ and the tip HQ $3.5/12$. The algorithm gives as a result the plots of different diagrams: C_l, C_d and C_m over the attack angle α, C_l/C_d over α and others. The plots vary for different Reynolds numbers. Figure 1.5 shows an example of the lift and drag polars for different Reynolds numbers. Given the root airfoil angle of attack, two different C_l are found for the root and for the tip, since the tip angle of attack is $\alpha_t = \alpha_r - 2°$. Thus, a mean coefficient of lift has been simply defined as the average value between the two values of C_l. The wing coefficient of lift is then calculated by a formula suggested by Raymer [24]:

$$C_L = 0.9\frac{C_{lr} + C_{lt}}{2} cos(\Lambda_{0.25c}) \tag{1.2.2}$$

where $\Lambda_{0.25c}$ is the quarter-chord line sweep angle, approximately $4°$. In example, the maximum coefficient of lift $C_{lr,max} = 1.32$ is reached by the root airfoil at an angle of

[2]Actually, *Profili* uses a graphical interface to the XFOIL algorithm. See `web.mit.edu/drela/Public/web/xfoil`.

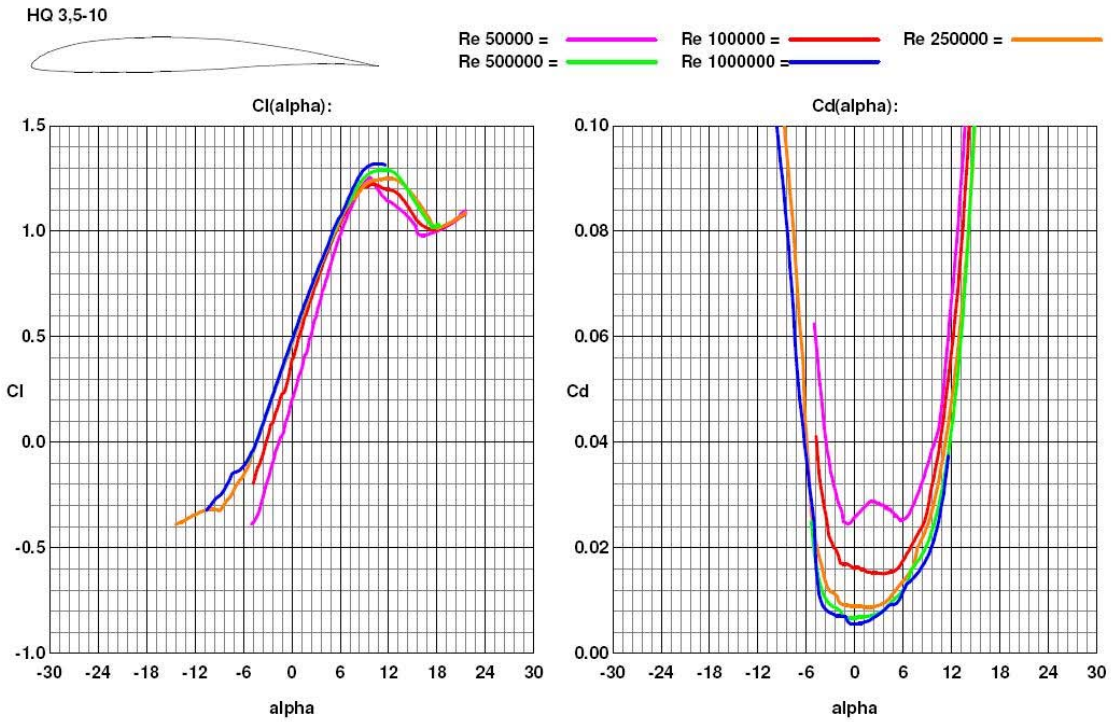

Figure 1.5: Example of lift and drag polars obtained for the root airfoil with Profili2©.

attack of $\alpha_t = 12°$; for this root angle, the tip has angle of attack of $\alpha_t = 10°$ and consequently a $C_{lt} = 1.3$. The wing maximum coefficient of lift is then

$$C_{Lmax} = 0.9\frac{1.32 + 1.3}{2} \cdot 0.997 = 1.18$$

Since the root airfoil has an inclination of $+2°$ with respect to the horizontal flight direction, the tip angle of attack is also the aircraft angle of attack. In the following calculations, "angle of attack" will refer simply to this angle.

1.2.3 V-n diagram description

It is now necessary to describe the points of the flight envelope that will be investigated. Kundu [16] gives a clear explanation about the V-n diagram and its relation to "real world" situations.
Starting from point $(0, 0)$ and going toward A, the maximum load factor is constrained by the aircraft C_{Lmax}. The minimum speed at point S is the stall speed V_S: this is the minimum speed at which the aircraft can carry its own weight. At stall speed, the maximum coefficient of lift is generated by an high angle of attack that is very close to

the stall angle. The stall speed can be calculated assuming $L = W$ and rearranging the lift equation 1.2.1:

$$V_S = \sqrt{\frac{2W}{\rho C_{Lmax} S}} = 27.6m/s = 99km/h \tag{1.2.3}$$

where the total aircraft mass has been assumed of $180kg$, so $W = 1765.8N$, and $C_{Lmax} = 1.18$ as calculated above.
At the end of the quadratic curve, the point A represents the condition in which C_{Lmax} is obtained just before the stall, producing the limit load $n = 4.5$. The normative prescribes a value of $n = 4$, but for safety a slightly higher limit load is assumed. The speed V_A is then calculated similarly to the stall speed, but assuming $L = nW = 7946.1N$.

$$V_A = \sqrt{\frac{2nW}{\rho C_{Lmax} S}} = 58.5m/s = 210km/h \tag{1.2.4}$$

It is worth to consider also the point C, corresponding to the design cruise speed of the aircraft. Even if is not necessary to investigate this condition, it is important to understand the configuration in which the aircraft will be most of the time. The cruise speed V_C is given by the normative as a function of the stall speed:

$$V_C = 2.2V_S = 60.6m/s = 218km/h \tag{1.2.5}$$

Since the angle of attack during level flight is zero, the corresponding lift coefficient is $C_L = 0.528$ and the lift generated at point C can be calculated:

$$L = \frac{1}{2}\rho V_C^2 C_L S = 3825N$$

that gives a load factor of $n = L/W = 2.16$. This high load factor means that the formula given by the norm is overestimating the cruise speed. If for example a load factor $n = 1$ is chosen, the minimum level flight speed can be obtained:

$$V_{C2} = \sqrt{\frac{2W}{\rho C_L S}} = 41.1m/s = 148.1km/s \tag{1.2.6}$$

At the right end of the diagram, the speed V_D is the maximum design speed, which usually occurs during a dive (V_D is called dive speed). At this speed, a very small elevator pull is enough to reach the limit load $n = 4.5$, so the angle of attack will not be very high. The speed V_D is calculated using the formula given by the regulations:

$$V_D = 1.5V_C = 87.7m/s = 316km/h \tag{1.2.7}$$

Thus, the wing coefficient of lift at point D is calculated by:

$$C_L = \frac{2nW}{\rho V_D^2 S} = 0.524$$

which, looking at the charts for the airfoils, is obtained for a zero angle of attack. This means that at the speed V_D the limit load is already reached without pulling the elevator. The negative side of the diagram regards the situations in which the aircraft experiments a negative load. At point E, the aircraft is moving with a speed V_D, and the pilot rapidly pushes the elevator down generating a negative lift on wings of $L = -2W$. The limit load is smaller than the limit load for the positive maneuver, since it is expected that it will not occur in normal flight conditions. As before, the lift coefficient at this point is calculated:

$$C_L = \frac{2nW}{\rho V_D^2 S} = -0.233$$

that corresponds to an angle of attack of approximately $\alpha = -8°$. The point G, similarly to the point A, satisfies both the conditions of negative stall and negative load factor of $n = -2$. The normative lets the designer assume a $C_{Lmin} = -0.68$ since is very difficult to obtain an accurate value for negative stall. Using these information the speed V_G is calculated:

$$V_G = \sqrt{-\frac{2nW}{\rho C_{Lmin} S}} = 51.3m/s = 185km/h \tag{1.2.8}$$

Points S0, F and AF lay on a different small flight envelope. This flight envelope refers to the wing with the flaps extended at an angle of $45°$. Extending the flaps adds a contribute to the C_{Lmax}; this contribute can be approximately assumed of 0.9 according to Raymer, so that the maximum coefficient of lift with flaps is $C_{Lmax,f} = 2.08$. The minimum speed at which the aircraft can fly is then the flapped-aircraft stall speed, and is calculated by

$$V_{S0} = \sqrt{\frac{2W}{\rho C_{Lmax,f} S}} = 20.7m/s = 74.5km/h \tag{1.2.9}$$

The normative indicates $V_{S0,n} = 65km/h = 18.06m/s$ as the maximum flapped stall speed for the advanced ultralight category. To obtain such a value, a larger wing surface is required. Keeping the same shape of the wing, a longer wingtip must be mounted. The required reference surface area should be:

$$S_2 = \frac{2W}{\rho C_{Lmax,f} V_{S0,n}^2} = 4.25m^2 \tag{1.2.10}$$

The base area of the wing without the tip is given by:

$$S_{base} = \frac{0.85 + 0.5}{2}(b - 2l_{tip}) = 2.835m^2 \tag{1.2.11}$$

where $l_{tip} = 0.4m$ is the length of the actual wingtip. Assuming a rectangular-shaped wingtip of width $w_{tip,2} = 500mm$, the length of the new wingtip should be:

$$l_{tip,2} = \frac{S_2 - S_{base}}{2w_{tip,2}} = 1.415m \tag{1.2.12}$$

However, the present calculations keeps the wingtip as previously sized. The opportunity of design a larger wingtip for respecting of the normative may be considered in a future work.
Another theoretical way to decrease the stall speed is to reduce the weight of the aircraft. Keeping the same wing reference area, the required weight to obtain the stall speed of $V_{S0,n} = 65km/h$ is given by

$$W_2 = \frac{1}{2}\rho C_{Lmax,f} V_{S0,n}^2 S = 1332N \tag{1.2.13}$$

which corresponds to a full-load mass of $m = 136kg$. Obtaining such a low mass for the Merlo would be a real engineering challenge.
The point F represents the maximum speed at which the aircraft can fly with the extended flaps, producing a load factor of $n = 2$. The norm gives a formula to evaluate V_F:

$$V_F = \sqrt{2} V_S = 39m/s = 140km/h \tag{1.2.14}$$

1.3 Longitudinal Stability

By now, the total lift, airspeed and angle of attack of each point of interest in the V-n diagram have been calculated. However, it would not be realistic to assume the total lift to be applied to the aerodynamic center of the aircraft. At least, it is necessary to consider the aerodynamic force generated by the horizontal tail, in order to give an initial estimate of the tail moment requested by the pitch stability of the aircraft. Megson ([20], chapter 14) gives an iterative method to estimate the lift forces acting on wings and tails.
The forces acting on the aircraft during flight can be assumed to be the following:

- L is the lift force applied to the aerodynamic center of the wing AC;
- D is the drag force applied to the aerodynamic center AC;
- M_0 is the aerodynamic pitching moment;
- P is the horizontal tail load, acting at the tail aerodynamic center (assumed to be at one quarter of chord length);
- W is the aircraft weight acting at the center of gravity CG;

- T is the thrust generated by the propeller. For simplicity, it is assumed to be applied to the aircraft center of gravity CG and to act in the direction parallel to the flight direction.

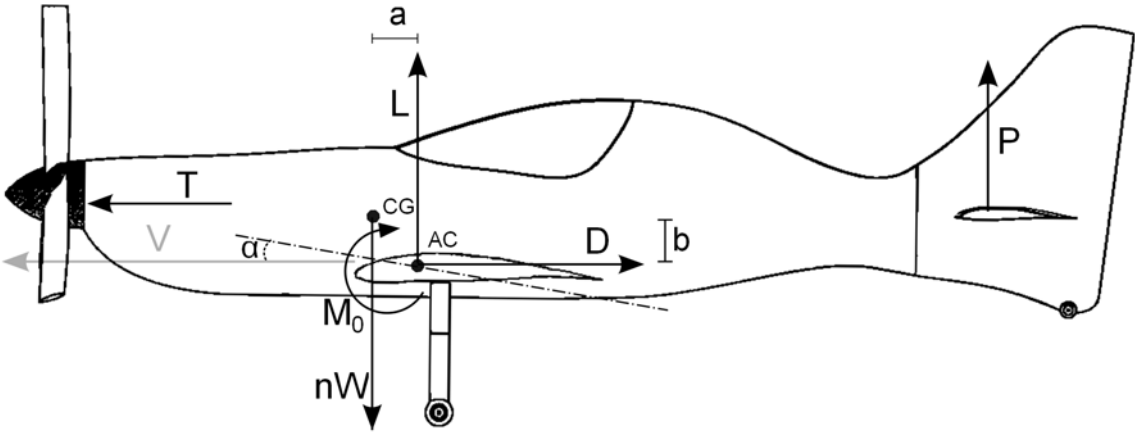

Figure 1.6: Forces acting on the aircraft during flight.

Referring to the figure, a is the horizontal distance between the aerodynamic center and the center of gravity of the aircraft, and it measures $70mm$ as previously calculated. The vertical distance b between these two points is difficult to estimate at this point; however, it can be assumed to be around $100mm$. For this length, the moments produced by drag and thrust are little, so they can be neglected for the preliminary calculations. Assuming the aircraft is in steady unaccelerated flight, the vertical equilibrium gives:

$$L + P - nW = 0 \tag{1.3.1}$$

while for horizontal equilibrium:

$$T - D = 0 \tag{1.3.2}$$

Taking the moments by the aircraft center of gravity

$$La - Db + M_0 - Pl_T = 0 \tag{1.3.3}$$

where l_T is the tail moment arm with respect to the center of gravity:

$$l_T = L_{HT} - a = 2.03m \tag{1.3.4}$$

At the first step of the iterative calculation, the load P can be neglected, so that $L = nW$. Using this value for the lift, the coefficient of lift of the wing is obtained:

$$C_L = \frac{2nW}{\rho V^2 S} \tag{1.3.5}$$

and the mean airfoil lift coefficient is obtained:

$$C_l = \frac{C_L}{0.9 cos\Lambda_{0.25c}} \tag{1.3.6}$$

Now, looking at the tables of the airfoil polars, the pitching moment coefficient at the quarter-chord point C_m can be obtained, and then the moment M_0 is calculated:

$$M_0 = \frac{1}{2}\rho V^2 S\bar{C}C_m \tag{1.3.7}$$

Thus, the load P can be calculated with the moment equation, neglecting the moment Db:

$$P = \frac{La - M_0}{l_T} \tag{1.3.8}$$

This value is inserted in the vertical equilibrium equation 1.3.1, at the beginning of step two:

$$L = nW - P$$

Then, the procedure is iterated until the values for L and P are calculated with a good approximation. This routine has been implemented in a MATLAB®script, and gives a good estimate of the forces just after four iterations.
Each point in the $V - n$ diagram has been investigated with this method. Table 1.1 presents a the values obtained for each point. Cases S_0 and F have not been investigated in this way, since there is no data for the lift polar curve of the flapped wing.

Case	n	V [m/s]	V [km/h]	α	$L[N]$	$P[N]$
S	1	27.5	99	$10°$	1736	30
S_0	1	20.7	74.5	$10°$	–	–
A	4.5	58.4	210	$10°$	7825	120
C	2.16	60.6	218	$0°$	3923	-120
C_2	1	41.1	148	$10°$	1816	-50
D	4.5	87.7	316	$0°$	8176	-230
E	-2	87.7	316	$-8°$	-3029	-502
G	-2	51.3	185	$-13°$	-3348	-183
F	2	39	140	–	–	–

Table 1.1: Summary of the aerodynamic data for the points in the $V - n$ diagram

1.4 Performance prediction

In this section, a brief performance analysis is presented. Ferus [10] already made the basic calculations that led to a first engine choice, mostly following Anderson [3]. Profes-

sor Sambin showed a particular interest for the possibilities of gliding flight with Merlo, so a performance prediction focused on gliding is now required.

1.4.1 Drag estimate

An estimate of the drag force is essential to predict the performance of the aircraft. If lift is considered "known" from design, since it must be at least equal to the weight W to make the aircraft fly, the drag force is a parameter that must be calculated to proceed to engine sizing and performance calculation. Drag force is given as a function of dynamic pressure, reference wing surface area and the drag coefficient:

$$D = \frac{1}{2}\rho V^2 S C_D \tag{1.4.1}$$

Drag is the sum of two drag components, one which is strongly related to lift and one which is not, called parasite or zero-lift drag. For this reason, for the drag coefficient is applied the following formula:

$$C_D = C_{D_0} + K C_L^2 \tag{1.4.2}$$

This relation implies that minimum drag occurs for zero lift: zero-lift coefficient is equal to the total drag coefficient when the coefficient for $C_L = 0$. This is true for uncambered wings, while for cambered wings the minimum drag occurs at some positive lift value. However, for small camber values the relation above can be used with an acceptable approximation.
Thus, to calculate drag it is necessary to know two coefficients, the zero-lift drag coefficient C_{D_0} and K, which is the factor that represents drag due to lift. Two methods from Raymer ([24], paragraphs 12.5 and 12.6) have been used to estimate these two coefficients.
The zero lift drag is obtained applying the component buildup method. This method calculates the parasite drag factors for each component of the aircraft, and the aircraft C_{D_0} is calculated as the sum of all components coefficients.

$$C_{D_0} = \frac{\sum (C_f F F Q S_{wet})_c}{S_{ref}} + \%C_{D,margin} \tag{1.4.3}$$

where C_f is the flat-plate skin-friction drag coefficient, FF is a form factor that estimates the pressure drag due to viscous effects,Q represents the interference effects on the component, S_{wet} is the component wetted area and S_{ref} is the wing reference area. Only two components have been deeply investigated, wings and fuselage. Drag due to other components is approximated by looking at historical data. Drag due to miscellaneous

V_{cruise}	$55m/s$
ρ	$1.225kg/m^3$
μ	$1.98 \cdot 10^5 kg/ms$
l_{wing}	$0.7m$
l_{fus}	$4m$
$C_{f,wing}$	0.0028
$C_{f,fus}$	0.0038

Table 1.2

factors is taken into account by a safety margin of 5%.
C_f for turbulent flow is calculated with the following formula:

$$C_f = \frac{0.445}{(log_{10}R)^{2.58}(1+0.144M^2)^{0.65}} \tag{1.4.4}$$

where R is the Reynolds number. The term containing the Mach number M can be neglected for low-subsonic speeds. The Reynolds number is calculated for each component as a function of its characteristic length l:

$$Re = \frac{\rho V l_c}{\mu} \tag{1.4.5}$$

The table 1.2 reports the values used for the calculation and the results for wings and fuselage.

For wings, the form factor is calculated using the following formula:

$$FF = \left[1 + \frac{0.6}{(x/c)_m}(t/c) + 100(t/c)^4\right]\left[1.38M^{0.18}(cos\lambda_m)^{0.28}\right] \tag{1.4.6}$$

which for $(x/c) = 0.35$ $(t/c) = 0.11$ and neglecting the term containing the Mach number gives $FF_{wing} = 1.138$.
For fuselage, the friction coefficient is calculated as the characteristic length and the average diameter (obtained from CAD drawings), $f = l_{fus}/d_{avg} = 5.89$, and then inserted into the following formula:

$$FF = \left(1 + \frac{60}{f^3} + \frac{f}{400}\right) = 1.308 \tag{1.4.7}$$

For both wings and fuselage, the interference factor Q can be neglected, since it is very close to 1. The wetted surface areas have been measured from CAD drawings:

$$S_{wet,wing} \approx 7m^2$$

$$S_{wet,fus} \approx 5m^2$$

Finally, the obtained values are inserted in the formula above and then C_{D_0} can be estimated:

$$C_{D_0,wing} = 0.094$$

$$C_{D_0,wing} = 0.0053$$

Looking at Raymer's design examples, drag due to the tail and to the landing gear can be approximated with the following values:

$$C_{D_0,tail} = 0.0025$$

$$C_{D_0,gear} = 0.002$$

Then, the total parasite drag coefficient is calculated:

$$C_{D_0} = (0.094 + 0.0053 + 0.002 + 0.0025) + 5\% \approx 0.02 \tag{1.4.8}$$

The K factor is calculated using the classical method based on the Oswald span efficiency factor e. According to the classical wing theory, the drag due to lift factor is obtained from the following formula:

$$K = \frac{1}{\pi ARe} \tag{1.4.9}$$

where AR is the aspect ratio, and e is the Oswald span efficiency factor, which for an unswept wing aircraft is obtained from the following empirical expression:

$$e = 1.78(1 - 0.045AR^{0.68}) - 0.64 \tag{1.4.10}$$

which, for an aspect ratio of $AR = 7.79$ gives a value of $e = 0.816$. K is then calculated:

$$K = \frac{1}{\pi 7.79 \cdot 0.816} = 0.05 \tag{1.4.11}$$

1.4.2 Gliding flight performance

The equations that govern the dynamics of an aircraft in steady, level flight are:

$$T = D = \frac{1}{2}\rho V^2 S(C_{D_0} + KC_L^2) \tag{1.4.12}$$

$$L = W = \frac{1}{2}\rho V^2 S C_L \tag{1.4.13}$$

When the aircraft is gliding, the engine is turned off so that $T = 0$. Then, according to the figure, the aircraft will slightly descend making an angle θ with the horizontal. The dynamics equations become:

$$D = Wsin\theta \tag{1.4.14}$$

$$L = W cos\theta \tag{1.4.15}$$

Assuming a small angle of descent, the lift to drag ratio is given by:

$$\frac{L}{D} = \frac{1}{tan\theta} \approx \frac{1}{\theta} \tag{1.4.16}$$

where θ is expressed in radians. For sailplanes, this ratio is called *glide ratio*, and represents the horizontal traveled distance for unit altitude lost. In example, a glide ratio of 30 means that for $1km$ of altitude lost the aircraft will travel $30km$ on the ground. Sailplane pilots try to obtain the highest value for this ratio by keeping the speed and attitude that maximize L/D. The speed for maximum L/D is given by (see Raymer[24] at chapter 17 for details):

$$V_{maxL/D} = \sqrt{\frac{2W}{\rho S}\sqrt{\frac{K}{C_{D_0}}}} = 37.7m/s \tag{1.4.17}$$

The value of the coefficient of lift at which maximum L/D is obtained is:

$$C_{L,maxL/D} = \sqrt{\frac{C_{D_0}}{K}} = 0.63 \tag{1.4.18}$$

The resulting maximum L/D, or glide ratio, is consequently found:

$$\left(\frac{L}{D}\right)_{max} = \frac{1}{2\sqrt{C_{D_0}K}} = 15.8 \tag{1.4.19}$$

The obtained value means that the Merlo is able to travel a ground distance of $15.8km$ on the ground with $1km$ of altitude. The time it takes to arrive at zero altitude is determined by the sink rate, the negative vertical velocity V_v:

$$V_v = Vsin(\theta) = Vsin\left(\frac{D}{L}\right) = 2.38m/s \tag{1.4.20}$$

In example, from an altitude of $1km$, the Merlo can fly for approximately 7 minutes before touching the ground.
Instead of maximizing the glide ratio, an attempt may be made to maximize the time that the aircraft will stay in the air, that is to say, the sink rate must be the smallest. As before, the following formulas are taken from Raymer. The lift coefficient for the minimum sink rate is:

$$C_{L,minV_v} = \sqrt{\frac{3C_{D_0}}{K}} = 1.09 \tag{1.4.21}$$

The speed for minimum sink rate is then found:

$$V_{minV_v} = \sqrt{\frac{2W}{\rho S}\sqrt{\frac{K}{3C_{D_0}}}} = 28.64m/s \tag{1.4.22}$$

which is close to the stall speed (without flaps). The glide ratio is given by

$$\left(\frac{L}{D}\right)_{max} = \sqrt{\frac{3}{16KC_{D_0}}} = 13.7 \tag{1.4.23}$$

The minimum sink rate is then found:

$$V_v = Vsin(\theta) = 2.09m/s$$

From an altitude of $1km$, the Merlo can fly at maximum for approximately 8 minutes.

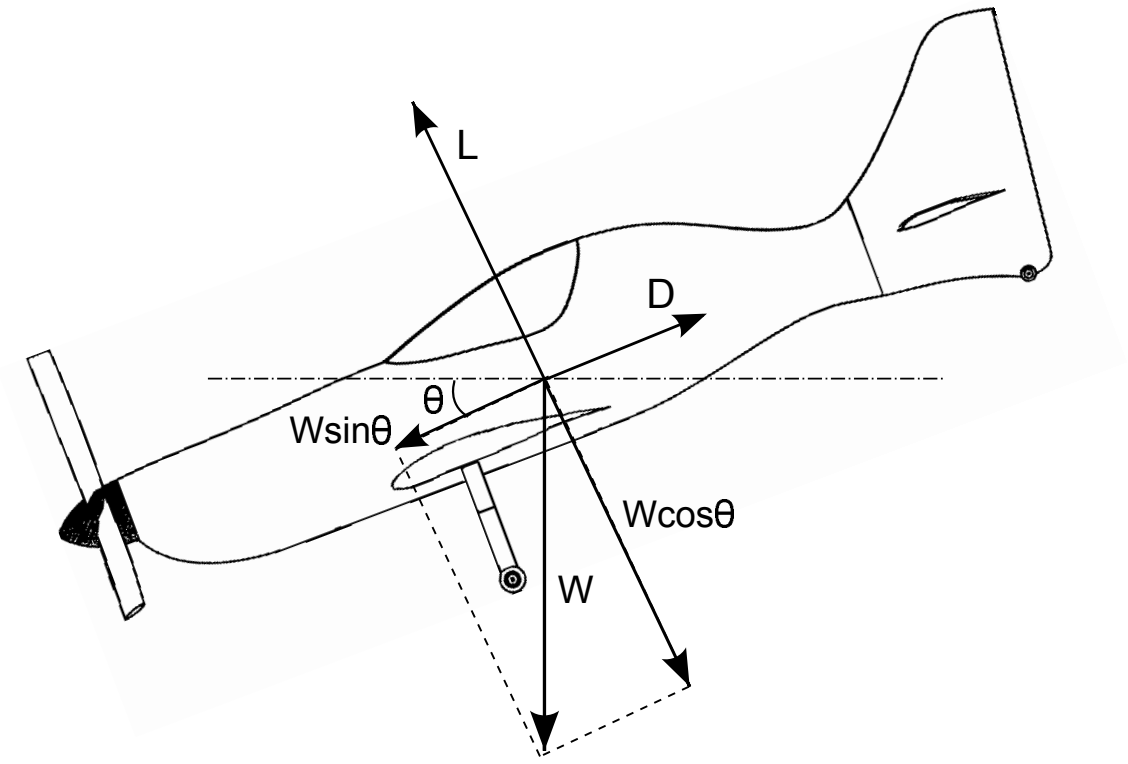

Figure 1.7: Equilibrium of the forces acting on the aircraft during gliding flight.

1.5 CFD Simulation

The aim of the cfd simulations that are presented here is to obtain the load distribution on the wing surface. This load distribution will be used as an input for the structural simulation that will follow, which purpose is to verify and correct the internal structure design. In addition, the cfd can be used as an instrument to verify the aerodynamic quality of the aircraft and to validate the assumptions made in analytical calculations above. The software used is Fluent®, which bases its calculations on the finite volumes method.

1.5.1 Set-up

A cfd software requires first the geometry of the model that will simulate the air flow around the aircraft. The geometry that has to be drawn is a fluid volume, whose inner boundaries are the aircraft surfaces (*walls* in cfd terminology, since the fluid cannot enter those surfaces). The external boundaries includes an *inlet*, which is the surface from where the fluid enters the control volume, an *outlet* and eventually some other boundary surfaces. The control volume must be chosen large enough so that the flow variations due to the presence of the aircraft are all contained; on the other hand, the smaller the control volume, and the smaller will be the number of fluid elements in which the volume will be divided. This condition is particularly relevant in this case since the educational license for Fluent limits the maximum number of elements to approximately 500'000.
The chosen shape for the control volume is a half-ellipsoid, where the curved surface is the inlet and the cut plane is the outlet. This shape has been chosen in order to ease the variations of the attack angle of the velocity at inlet, having only two borders instead of the six that will occur in case of a parallelepiped-shaped control volume. In addition, since the aircraft shape is almost perfectly symmetrical, only a half of the aircraft can be analyzed, reducing the number of cells and then the computational time requested. In this way, the control volume reduces itself to a quarter-ellipsoid, giving the condition of *symmetry* to the plane of symmetry of the aircraft.
Once the geometry is set, the mesh can be created. The mesh must be thickened in proximity of the aircraft, in order to obtain accurate results where is requested. In particular, the mesh has been given an element edge size of $5mm$ at the leading edge of wing and tail, a $20mm$ size on the wing and tail surfaces and a $100mm$ size on the fuselage on the aircraft.
Giving this sizes to the mesh results in a number of element that exceeds 1,000,000. Such an elevate number of element cannot be managed with the FLUENT educational license; fortunately, FLUENT has a function that transforms the tetrahedral elements in polyhedral elements, keeping the same precision and reducing dramatically the number of elements that must be computed. In fact, the resultant number of elements after

this process is approximately 200,000, which is far under the 500,000 threshold for the educational license.

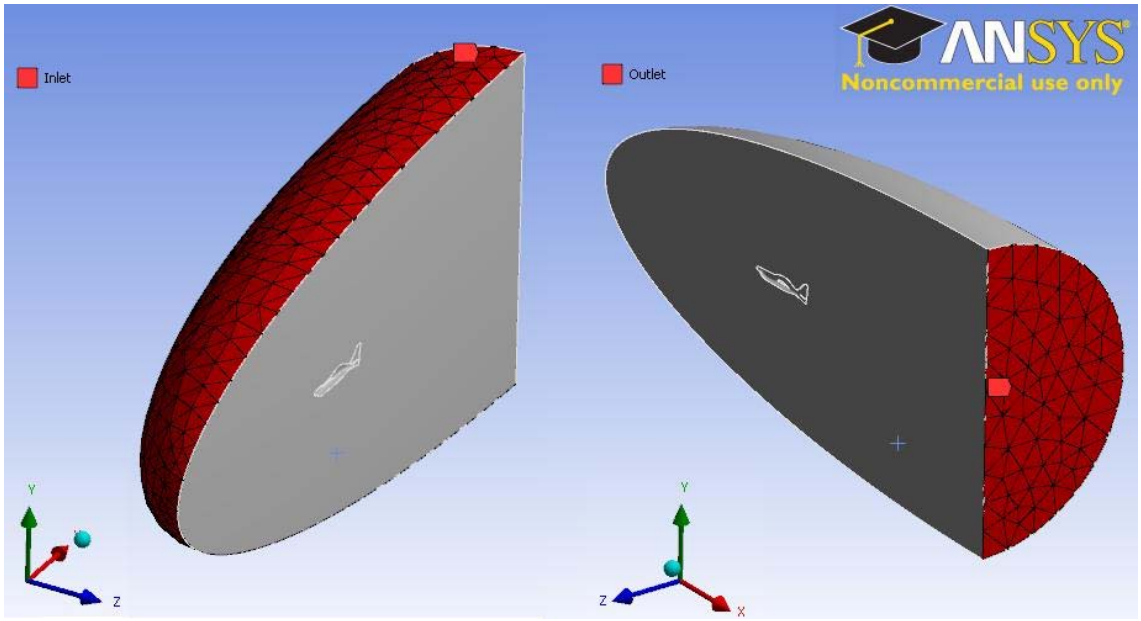

Figure 1.8: Views of the fluid control volume. The inlet and outlet regions are highlighted.

The velocity is given at the *inlet* section. Since the *inlet* surface is not planar, the velocity vector has been defined in terms of magnitude and direction with respect to the XYZ coordinate system. The X coordinate is in the level flight direction, thus the drag vector will be oriented with X; the Y direction is parallel to lift, and Z completes the system. In table 1.3 the input velocity vectors are given for each point of interest in the V-n diagram. The Z-direction cosine is always zero.

	Magnitude	X-direction cosine	Y-direction cosine
V_A	58.4	0.9848	0.1736
V_C	60.6	1	0
V_{C2}	41.1	1	0
V_D	87.7	1	0
V_E	87.7	0.9848	−0.1736
V_G	51.3	0.9744	−0.2249

Table 1.3

The boundary condition at *outlet* is given by simple setting the relative pressure to zero.
FLUENT® offers different turbulence models to close the system of equations governing

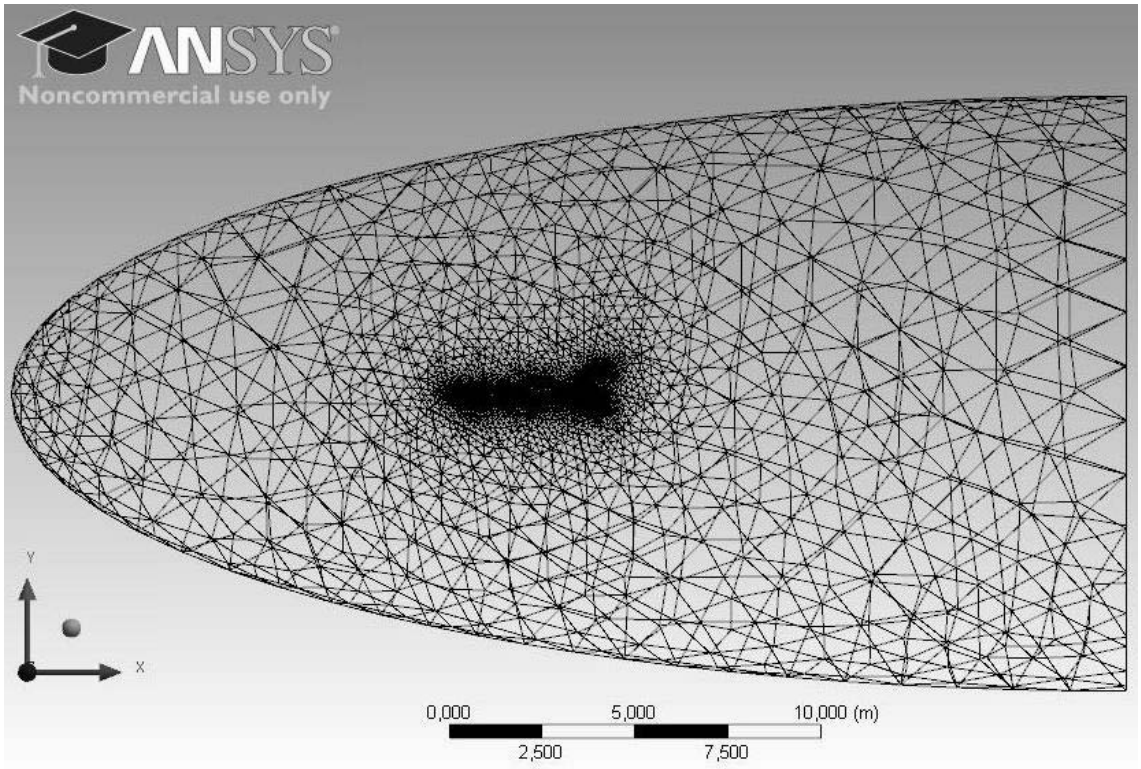

Figure 1.9: Mesh of the control volume.

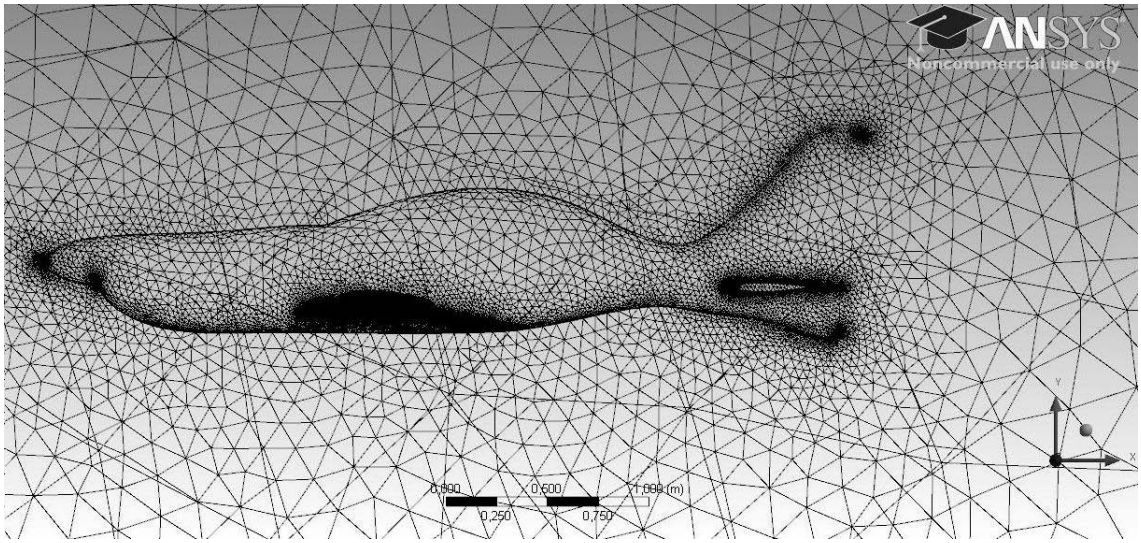

Figure 1.10: Details of the mesh. The mesh is refined in proximity of wings, tails and aircraft curved surfaces.

the flow. For this simulation, the Spalart-Allmaras[1] model has been chosen. It is a one equation model which solves a transport equation for the turbulent viscosity ν_T. It is indicated for flows with mild boundary layer separation, so stall simulation should be avoided.

1.5.2 Solution and results

The solution is initialized in order to provide the solver with an initial guess for the velocity and pressure distribution at the flow field. In this case, the standard hybrid initialization has been chosen [11].
Once the solution is initialized, the iterative solution can be started. The solution converges when the value of the calculation residuals reaches a tolerance that is given in input. During the solution, the program plots a diagram of C_L versus the number of iterations. The solution convergence can be seen also from the C_L curve, which converges to the correct value. The average iteration number to reach convergence is approximately 200.

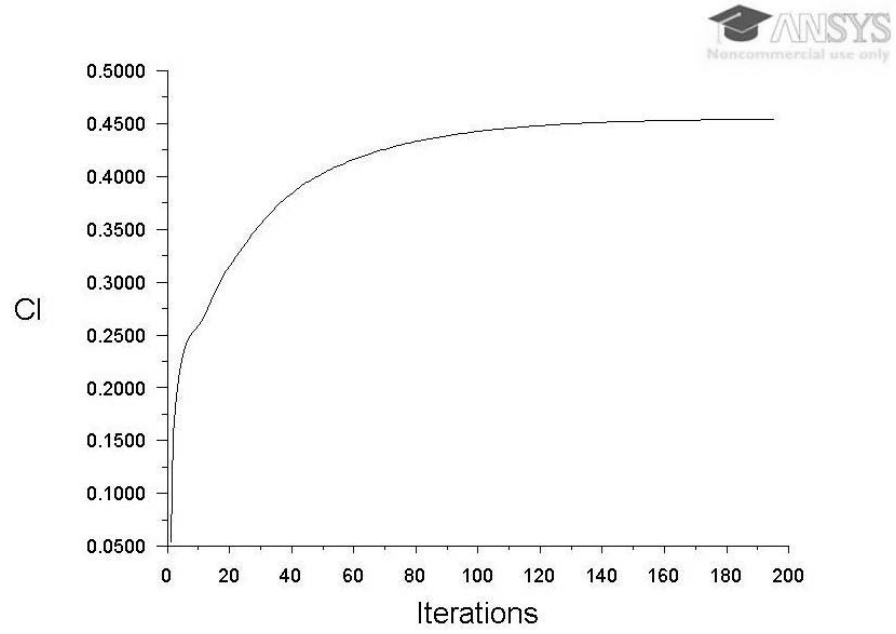

Figure 1.11: Convergence of C_L versus the number of iterations.

The calculated coefficient of lift differs from the coefficient calculated analytically; in the cases of level flight (C,D) it is smaller as it may be expected, since the analytical

[1]For an accurate description of this model, see: P.Spalart and S.Allmaras. *"A one-equation turbulence model for aerodynamic flows". Technical Report AIAA-92-0439.* American Institute of Aeronautics and Astronautics. 1992.

calculation partially considered the effects of the finite wing, like downwash. On the other hand, at high angles of attack (A,E) it results higher. This can be explained since at very high and very low angles of attack the wing is close to stall condition. Near stall condition the cfd model cannot be considered reliable any more, at least for two reasons:

1. Stall is a multi-scale phenomenon, meaning that recirculation interest either large and very small fluid regions, so small that the created mesh cannot capture it. In addition, it is difficult to simulate stall with a steady model, since stall is typically an unsteady phenomenon.

2. The Spalart-Allmaras turbulence model is not indicated for flows with large separation and recirculation, as it happens during stall.

For the same reasons, the results for G cannot be obtained, since the solution could not converge within an acceptable tolerance.

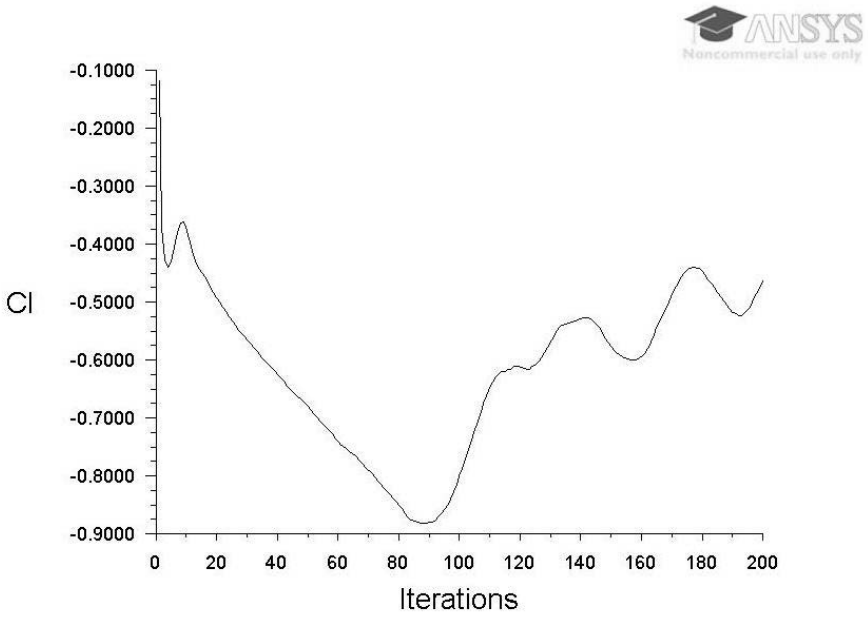

Figure 1.12: Case G: example of non-converging solution. The value of C_L changes with wide oscillations.

Table 1.4 reports the calculated value of C_L for the different angles of attack, the percent variation from the analytical value and the lift values obtained from the simulation. From the lift values, the load factor n is calculated.

Values obtained for the limit load are acceptable for cases A and E. This means that the pressure distribution obtained in these cases can be applied to the mechanical model

Case	C_L	% variation	Lift $[N]$	n
A	1.24	$+5\%$	8092	4.58
C	0.44	-16%	3086	1.75
C_2	0.44	-16%	1458	0.83
D	0.44	-16%	6744	3.83
E	-0.26	$+13\%$	-3978	-2.25
G	$-$	$-$	$-$	$-$

Table 1.4

of the wing in order to verify the spars strength. For cases C_2 and D, the calculated limit load does not reach the safety values given by the norm. In order to obtain the required loads, two new cases C_3 and D_2 have been considered. In C_3, the level flight is kept, thus attack angle remains zero; the speed has increased to the value at which $n = 1$ is expected, considering the new C_L:

$$V_{C3} = \sqrt{\frac{2W}{0.44\rho S}} = 45.2m/s \tag{1.5.1}$$

In the case D_2, speed is kept at the V_D value; the angle of attack is increased to obtain the value for C_L that was analytically calculated in order to obtain $n = 4.5$. Since an increase in C_L of 0.09 is required, looking at the lift polars an angle increase of approximately 1° is found. The new angle of attack is then $\alpha_{D2} = 1^\circ$. The velocity inputs are reported in table 1.5.

	Magnitude	X-direction cosine	Y-direction cosine
V_{C3}	45.2	1	0
V_{D2}	87.7	0.9998	0.0175

Table 1.5

Two new simulations have been set with the data above. The results are reported in table 1.6. The obtained values are suitable for the structural validation.

Case	C_L	Lift	n
C_3	0.44	1906	1.08
D_2	0.53	7780	4.41

Table 1.6

Chapter 2

Wing structural analysis

The purpose of this chapter is to verify the wing structural components designed under professor Sambin guidelines. The wing structure layout is presented, and the choice of materials is specified. Then, a first sizing of the main spar is obtained with analytical calculations. Finally, a detailed finite element model of the wing has been built and analyzed to verify the design of the structure.

2.1 Structure layout

2.1.1 Wing inner structure

Merlo's internal structure is conceived to obtain maximum strength with the least weight; where possible, the components have been be designed in order to let the professor himself build them "at home", with common materials and instruments.
The spars are the most important structural component of the wings, since they carry the airloads during flight and the wing weight while on the ground. Merlo's wing has a total of four spars: a main central spar, a front spar, a back spar and a the spar at which the control surface, the flaperon, is attached.
The first two spar, the main and the front, are expected to carry most of the load. They are built in the same way, being the front one a smaller version of the main spar. The spar consist of two beams made of fir wood that run all the way from the aircraft plane of symmetry to the rib located at $1.8m$ from the effective wing root. The total length of the main spar is $2.1m$, including $300mm$ from the plane of symmetry of the aircraft to the beginning of the wing. The beams of the main spar are tapered from a width of $100mm$ at the intersection with the fuselage to a width of $50mm$ at the last rib. The front spar has two constant-width beams of $30mm$. The ribs are placed perpendicularly to the wooden beams at a constant interval of $150mm$. Thus, in the main part of the wing are allocated $1800/150 = 12$ ribs, plus one at the beginning, making a total of 13

ribs. Between the ribs, two vertical side beams made of birch plywood are glued to the main beams. In order to obtain a larger area to spread the glue, and thus for making the structure more resistant, four thin strips of wood are added to the internal corners. The figure fig:sparcross shows the cross sections of the main and the front spar. The horizontal beams plus the side plates make a sort of hollow-rectangular cross-section, with reinforcements at the corners. The thicknesses have been given by professor Sambin as an initial guess. The height of the cross-section is not indicated since it must match the thickness of the airfoil at each section. For this reason the spars result to be slightly tapered also in the vertical direction. Referring to the effective root airfoil, the center of the main spar is located at $320mm$ from the leading edge, while the front is located at $100mm$ from the leading edge.

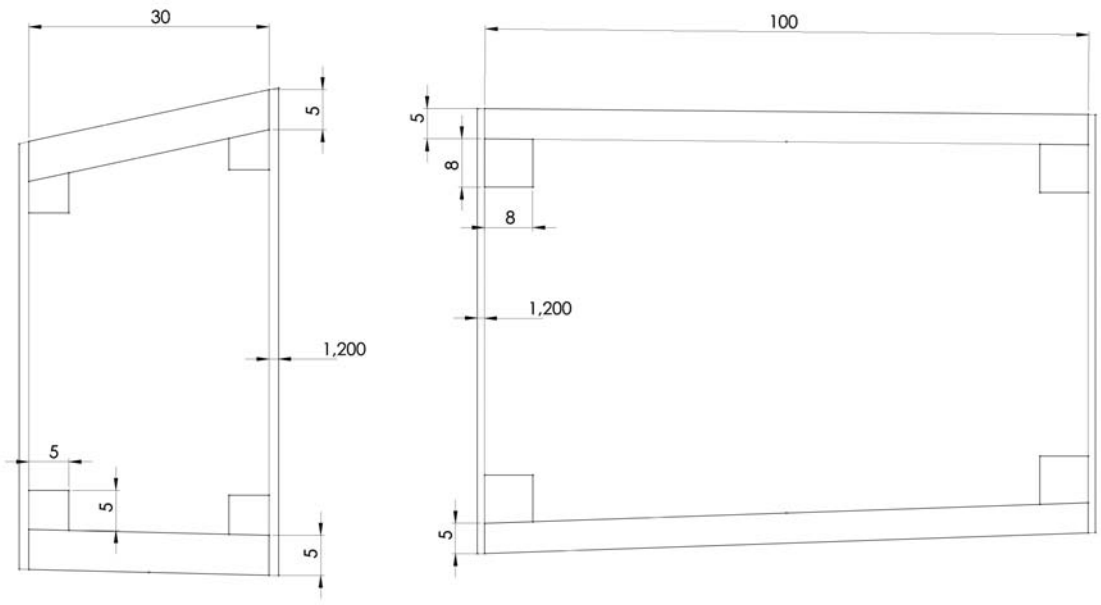

Figure 2.1: Cross-sections of main and front spars at the beginning of the wing, with initial dimensions. The figure does not show the reinforcement fir plies that will be glued under the main ply of $5mm$ thickness.

The last two spars are made of carbon rovings, with a constant hollow-circular cross-section of diameter $20mm$. The thickness is assumed to be of $0.8mm$. The back spar cross-section center is located at approximately 540mm from the leading edge at the first rib. The back spar is placed perpendicularly with respect to the rib plane. The flap spar is located approximately at 12% of the airfoil chord from the trailing edge, resulting inclined relatively to the ribs. The ribs are cut between the back and the flap spar, leaving enough room for a $\pm 45^{\circ}$ rotation of the flaperon.

All the connections between spars, ribs and wing skin will be made with high-strength glue.
The main connection between the airplane body and the wings consists in a pivot that links the main spar to the spar box. The spar box will be a very rigid hollow-rectangular box connected to the fuselage walls, into which the main spar will be inserted and fixed through a bolted connection. The accurate design of the spar box and its modeling will not be treated in this work, since it requires a complex analysis.

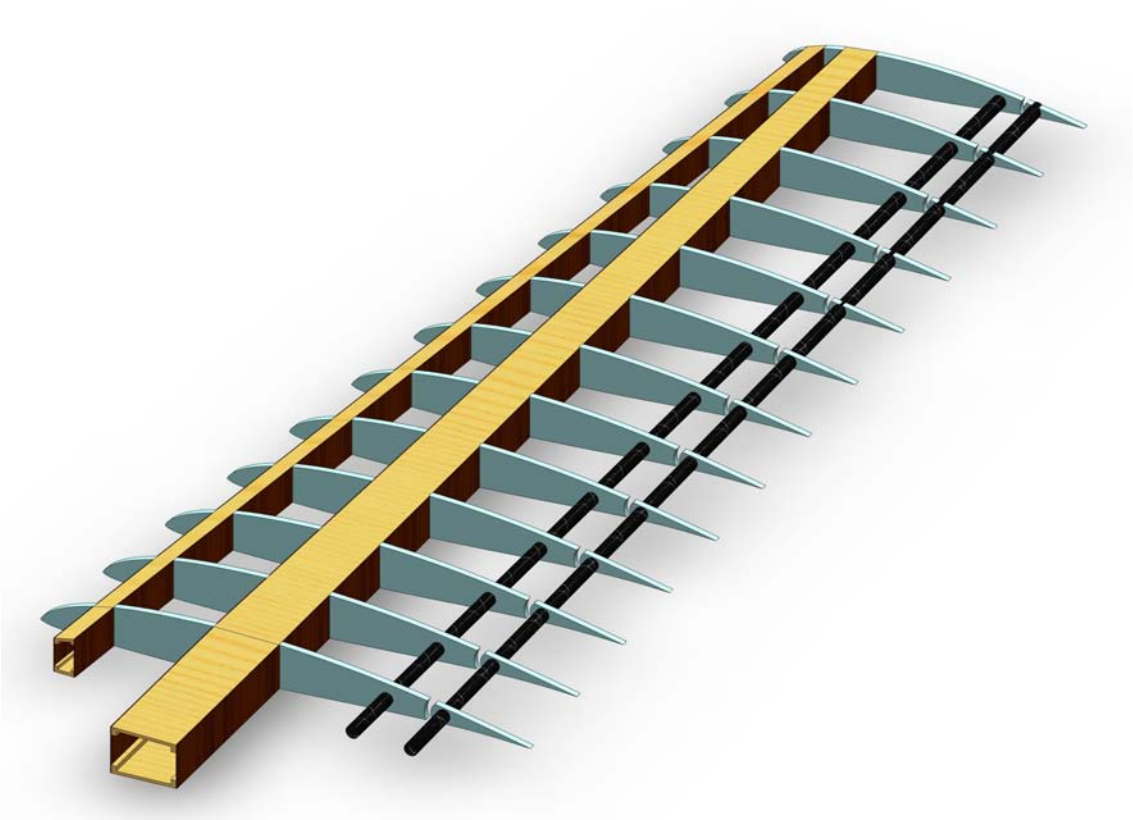

Figure 2.2: 3D CAD model of the wing inner structure.

2.1.2 Wing tip

The wing as it has been described above has a total length of $2.1m$ from the plane of simmetry to the last (the 13th) rib. Since the total semi-wing span is $2.5m$, the remaining $0.4m$ are covered by the wing tip, that will be realized separately and mounted on the wing later. The shape of the tip has quite important effects on the wing drag due to the tip vortices. If the tip is smoothly-rounded, the air can easily flow around the tip. If it has a sharp edge, the air flow is interrupted, causing a decrease in the induced

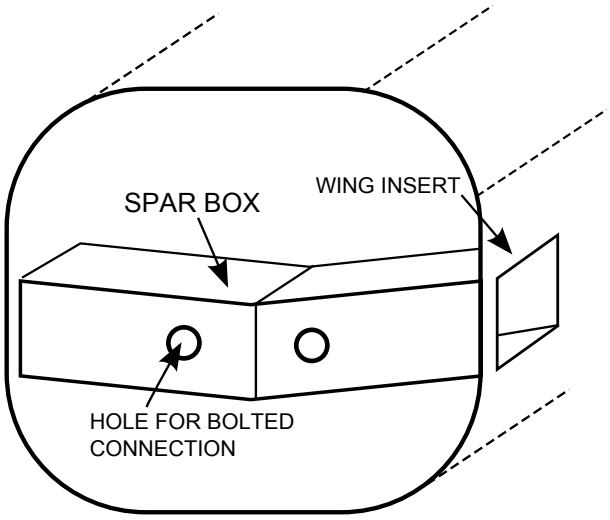

Figure 2.3: Sketch of the spar box. The spar box must be inclined with respect to the fuselage wall to give the wing the required dihedral.

drag, as demonstrated by Hoerner [14]. For this reason, the most used low-drag tip is the Hoerner wing tip, basically a sharp-edged wing tip with the upper surface continuing the upper surface of the wing.
Another interesting tip that prof. Sambin has been considering is the upswept wing tip. Its effect is to increase effective wing span without increasing the total span, separating the flow of air from the bottom of the wing (high pressure) to the top (low pressure), and thus reducing the induced drag.

The cfd and structural analysis have been done considering a simple cut-off wing tip. The lack of the real wing tip that will be mounted on the Merlo goes toward safety, since a smaller drag is expected using the tip.
The wing tip skin is sustained by a total of three ribs. The first is located at $100mm$ from the wing end, the middle at $150mm$ from the first one and the last at the tip end. The wing tip will be connected to the main wing with a carbon-carbon tube as the ones used for the back and flap spars. The tube is placed into the main spar, starting from the 9th rib and going into the tip, ending at the middle tip rib. The first tip rib is also connected with a $12mm$ aluminum axle to the back spar. The wing tip connections have been conceived for the possibility of mount different kinds of tips on the wing.

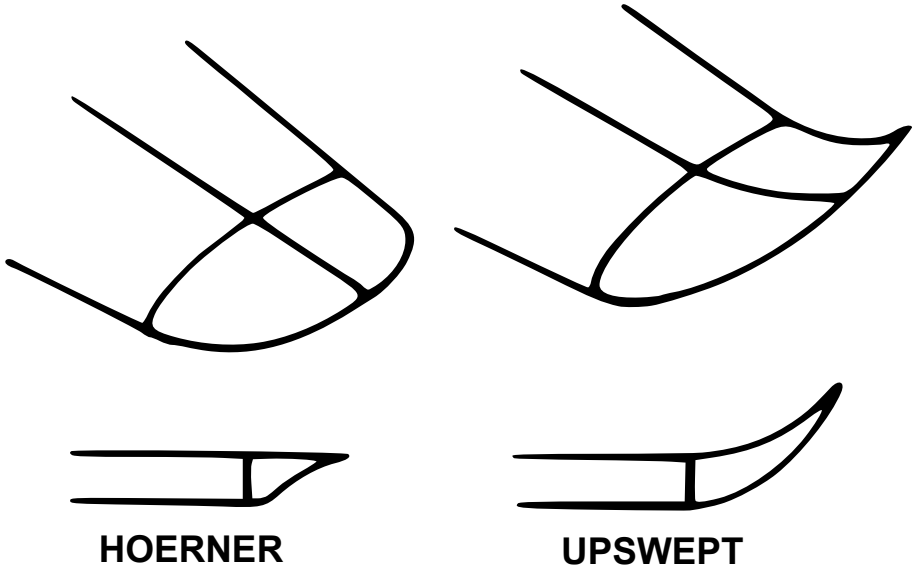

Figure 2.4: Two wing tips considered for the merlo [24]

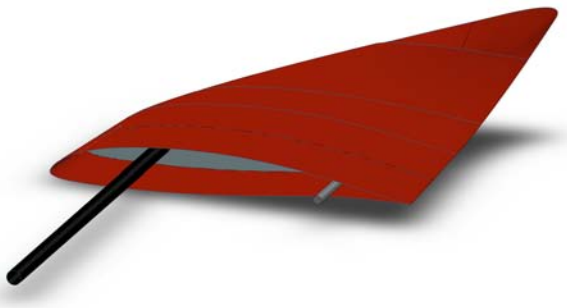

Figure 2.5: 3D CAD model of a possible upswept tip for Merlo's wing.

2.2 Material choice

2.2.1 Wooden materials

Today, the advancements in the production techniques give the builders the possibility to choose between a wide variety of high-strength composite materials, which weight is much less than their respective metallic counterparts. However, wood is still an excellent material for the construction of light aircrafts due to its characteristics:

- Good strength-to-weight ratio;
- Easy to fabricate and repair, especially for homebuilders;
- Long fatigue life, longer than aluminum or steel;
- Low cost, compared with composite materials;
- It is the construction material that has been most used, so a lot of information it is available regarding its mechanical properties and behavior.

However, the wood pieces from which the components are made must be chosen carefully. Each piece of wood is unique, and making the right choice requires a lot of experience. For this reason, the mechanical properties of wood vary in a larger interval with respect to metallic materials, the production of which is controlled. In addition, it must be kept the most isolated as possible from moist, which is the main cause of wood failure in the long time.
Wood mechanical behavior is typically orthotropic: it has different properties (Modulus of elasticity, strength etc.) in the direction of three perpendicular axes. Conventionally, L is the axis parallel to the fiber (also called grain), R is the axis perpendicular to the grain that is radial with respect to the growth rings and T is the axis tangential to the growth rings and perpendicular to the other two. Recalling the constitutive relations of an orthotropic material, the strain tensor can be written as following:

$$\mathbb{D} = \begin{bmatrix} \frac{1}{E_x} & -\frac{\nu_{xy}}{E_y} & -\frac{\nu_{xz}}{E_z} & 0 & 0 & 0 \\ -\frac{\nu_{yx}}{E_x} & \frac{1}{E_y} & -\frac{\nu_{yz}}{E_z} & 0 & 0 & 0 \\ -\frac{\nu_{zx}}{E_x} & -\frac{\nu_{zy}}{E_y} & \frac{1}{E_z} & 0 & 0 & 0 \\ 0 & 0 & 0 & \frac{1}{2G_{xy}} & 0 & 0 \\ 0 & 0 & 0 & 0 & \frac{1}{2G_{xz}} & 0 \\ 0 & 0 & 0 & 0 & 0 & \frac{1}{2G_{yz}} \end{bmatrix}$$

As it can be seen, twelve constants are needed to define the behavior of wood: 3 Young's moduli, 3 Shear moduli and 6 Poisson's ratios. Considering a conservative material, only

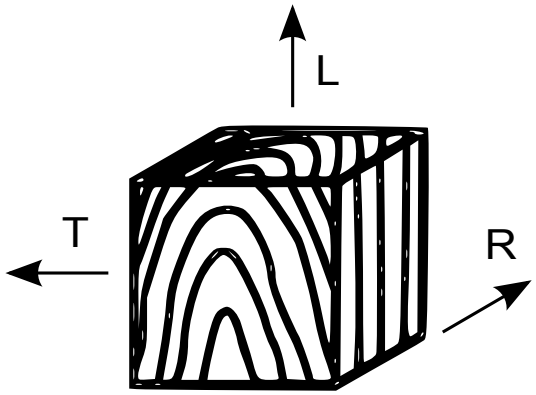

Figure 2.6: Wood principal direction for modeling as an orthotropic material.

9 constants are required, since for the Poisson's ratios the following relation is valid:

$$\frac{\nu_{ij}}{E_i} = \frac{\nu_{ji}}{E_j} \tag{2.2.1}$$

The classic wood for aircraft construction is the American Sitka Spruce (*Picea sitchensis*) [1]. It has become the standard for judging all other types of wood. Its characteristics are light weight, high strength, it is resistant to rotting and presents a uniform texture with very few defects. Unfortunately, this tree is found along the North-western coast of the American continent, so an Italian alternative must be found. The literature offers various types of fir as a valid alternative to spruce. Professor Sambin's choice has been the Silver Fir (*Abies alba*), commonly found in Italy and Europe. The mechanical properties found in literature are often contrasting: this because of the large variation of mechanical properties of two different pieces of the same wood (up to $\pm 25\%$). The table presents a comparison between the properties of Silver fir obtained from different sources and Sitka spruce properties, which are found in [12].

	Spruce, Sitka [12]	Fir, Silver [12]	Fir, Silver [17]	Fir, Silver [25]
Density $[kg/m^3]$	400	350	460	380
Modulus of Elasticity, long. E_L $[Pa]$	$10.8 \cdot 10^9$	$10 \cdot 10^9$	$10 \cdot 10^9$	$8.8 \cdot 10^9$
Poisson's ratio ν_{LT}	0.47	0.33	–	–
Strength, long. tension $[Pa]$	$70 \cdot 10^6$	$63 \cdot 10^6$	$83 \cdot 10^6$	$77 \cdot 10^6$
Strength, long. compression $[Pa]$	$38.7 \cdot 10^6$	$36.4 \cdot 10^6$	$37 \cdot 10^6$	–

Table 2.1: Spruce and Fir wood properties comparison.

The birch plywood, also called aircraft plywood, is widely used in the construction of aircraft models and sailplanes. It has very good mechanical properties due to its manufacturing process: in fact, it is obtained by gluing with resin very thin birch veneers

at high temperature and pressure. In this way, all the defects are discarded, and the hardened resin adds resistance to the material, making the compression strength almost equal to the tension, and reducing the anisotropic effect. The initial choice for Merlo is a birch plywood of $1.2mm$ thickness, made of three $0.4mm$ layers. The properties of fir wood are reported in the table, according to different sources.

	Birch [12]	Birch [24]
Density $[kg/m^3]$	620	720
Modulus of Elasticity, long. E_L $[Pa]$	$13.9 \cdot 10^9$	$12 \cdot 10^9$
Poisson's ratio ν_{LT}	0.45	–
Strength, long. tension $[Pa]$	$114 \cdot 10^6$	$107 \cdot 10^6$
Strength, long. compression $[Pa]$	$59 \cdot 10^6$	$50 \cdot 10^6$
Strength, perp. tension $[Pa]$	$6.7 \cdot 10^6$	$11 \cdot 10^6$
Strength, perp. compression $[Pa]$	$6.3 \cdot 10^6$	–

Table 2.2: Birch wood properties.

2.2.2 Composites

Although wood has good mechanical properties, some components require higher-performance materials. In this cases, in order to keep low weights, composite materials are the obliged choice.

For the back and flap spars of the wing, professor Sambin chose carbon-carbon pipes to get highly resistant, light and space-saving beams. The properties of the carbon fiber in carbon (epoxy) matrix may vary from producer to producer; for initial calculations average properties are taken according looking at the web databases [19]. Carbon-carbon may be considered an isotropic material.

The ribs are made of $10mm$ thick flexyfoam sheets. Flexyfoam is an expanded closed-cell PVC, mostly used as a core material for the sandwich panels. It is widely used by model builders because of its good rigidity and strength-to-weight ratio. Different types are available, classified by density. Baldon [7] presents the full set of flexyfoam types. Following his work, the choice has been the flexyfoam M-130, whose properties

	Carbon fiber
Density $[kg/m^3]$	1600
Modulus of Elasticity E $[Pa]$	$80 \cdot 10^9$
Poisson's ratio ν	0.33
Strength, compression $[Pa]$	$230 \cdot 10^6$

Table 2.3: Carbon-carbon properties [19].

	Flexyfoam
Density $[kg/m^3]$	130
Modulus of Elasticity E $[Pa]$	$0.108 \cdot 10^9$
Poisson's ratio ν	0.49
Strength, tension $[Pa]$	$3.7 \cdot 10^6$
Strength, compression $[Pa]$	$3.6 \cdot 10^6$
Strength, shear $[Pa]$	$2.4 \cdot 10^6$

Table 2.4: Flexyfoam M-130 properties [7].

are reported in the table.

The wing skin material selection is fundamental due to the skin function. It must transfer the pressure loads to the spars, carrying high stresses especially in the areas of skin between the supports of spars and ribs. For this reason, a sandwich panel may be the best choice: the skins provide the required stiffness, and the core rigidly joins the two faces granting high torsional and bending rigidity. In his work, Baldon [7] designed the aircraft fuselage, verifying the performance of three different sandwich panels. The core consists in a flexyfoam panel, while the skins have been modeled using various layers of glass fiber in epoxy matrix. This composite has been chosen for its good mechanical properties and for its low cost if compared to the Rohacell® counterpart[1]. This material presents an orthotropic behavior: its main properties are shown in table 2.5. The sandwich that has been chosen for the fuselage by Baldon is made of 4 layers of glass/epox per side, with a $5mm$ core. The layers are placed at different inclinations in order to get an isotropic behavior: from the external layer to the inner one, the layers have been placed respectively at $0/-45/+45/90°$.

[1] www.rohacell.com

	Glass fiber + epox composite
Density $[kg/m^3]$	1630
Modulus of Elasticity E_L $[Pa]$	$15.8 \cdot 10^9$
Modulus of Elasticity E_T $[Pa]$	$4 \cdot 10^9$
Poisson's ratio ν_{LT}	0.24
Strength, long. tension $[Pa]$	$200 \cdot 10^6$
Strength, long. compression $[Pa]$	$150 \cdot 10^6$
Strength, trans. tension $[Pa]$	$36 \cdot 10^6$
Strength, trans. compression $[Pa]$	$30 \cdot 10^6$
Strength, shear $[Pa]$	$40 \cdot 10^6$

Table 2.5: Glass fiber/epox composite properties [7].

2.3 Analytical calculations

Before proceeding to the finite element analysis of the wing structure, it is good to obtain a first sizing of the thickness of the spar components through analytical calculus. At a first approximation, it is assumed that only the main spar carries the total load acting on the wing. This assumption goes toward safety and leads to oversize the thickness, since in the real structure there are two more spars that carry part of the load. The spar can be modeled as a cantilever beam, where one end is constrained into the fuselage and at the free end a vertical load L is applied (figure 2.7). Stress distribution due to the drag and the pitching moment can be neglected in this phase. The worst load cases are points A and D in the flight envelope, where the load factor is assumed $n = 4.5$. Thus, the load L at free end is calculated as follows:

$$L = \frac{1}{2} nW = 0.5 \cdot 4.5 \cdot 180 \cdot 9.81 \approx 4000N \tag{2.3.1}$$

The length at which the load L is applied is assumed to be the distance from the effective root airfoil to the mean aerodynamic chord, and its value is $l = 815mm$. The moment distribution along the spar is linear and it is given by

$$M(z) = -L(l - z) \tag{2.3.2}$$

The spar cross-section is approximated as in figure 2.8. The main load is carried by two horizontal fir wood beams. The vertical plywood reinforcements main function is to connect the two fir spars, allowing them to work together as a single beam. The four strips of wood at the corners are not included, since their structural function is negligible. To obtain the stress distribution on the section, the composite beam method is used ([18], paragraph 11.3.3.2). Since each material has a different modulus of elasticity, it is necessary to define an equivalent beam rigidity as follows:

$$EI_{eq} = E_{fir} I_{x,fir} + E_{birch} I_{x,birch} \tag{2.3.3}$$

where $E_{fir} = 10GPa$ and $E_{birch} = 13GPa$ are the moduli of elasticity of fir wood and birch plywood, whose values have been taken as an average value between the

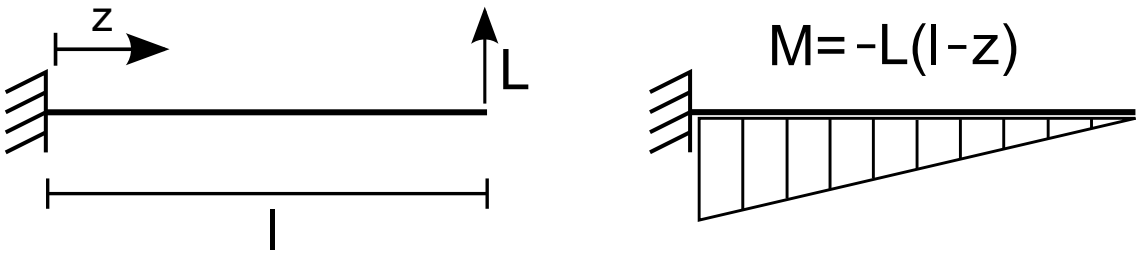

Figure 2.7: Cantilever beam model of the main spar, with the lift load L concentrated at free end.

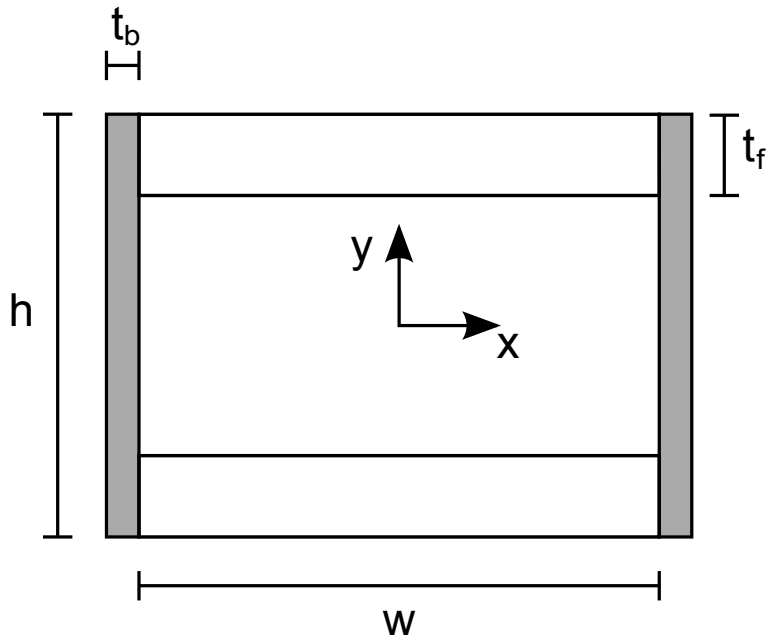

Figure 2.8: Main spar cross-section.

different values found in the literature. The second moment of area are calculated for each material. Thus, referring to figure 2.8, the moment of inertia along the x axis for the two fir wood spars is:

$$I_{x,fir} = 2\left(\frac{wt_f^3}{12} + \left(\frac{h-t_f}{2}\right)^2 wt_f\right) \tag{2.3.4}$$

while for the plywood reinforcements it is given by:

$$I_{x,birch} = 2\frac{t_b h^3}{12} \tag{2.3.5}$$

Since the two materials have different moduli of elasticity, a stress discontinuity will occur at the interface between them. In fact, using the calculated value of EI_{eq}, the stress distribution as a function of the y coordinate is different for the two materials, and it is given by:

$$\sigma_z(y)_{fir} = E_{fir}\frac{M}{EI_{eq}}y \tag{2.3.6}$$

$$\sigma_z(y)_{birch} = E_{birch}\frac{M}{EI_{eq}}y \tag{2.3.7}$$

The maximum stress occurs where y is maximum. The height of the section may be assumed to be constant through the length of the spar, thus $y_{max} = h/2 = 35mm$.

$t_f[mm]$	$\sigma_{max,fir}[MPa]$	$\sigma_{max,birch}[MPa]$	n_{fir}	n_{birch}
5	97	127	0.72	0.87
10	59	77	1.19	1.43
15	47	61	1.49	1.8
20	42	54	1.67	2.04
25	39	51	1.79	2.16

Table 2.6

The fir beams are tapered both in width and thickness, so it may be necessary to verify the maximum stress at different positions along the spar length (for a more detailed formulation about tapered beams, see the next chapter). The width varies from a value of $w_1 = 100mm$ at the constrained section to a value at the mean aerodynamic chord which is given by

$$w_{mac} = 0.815\frac{(w_2 - w_1)}{1.8} + w_1 = 77mm \tag{2.3.8}$$

where $w_2 = 50mm$ is the width at the end of the spar, located at $1.8m$ from the fuselage. The variation in thickness is not continuous, since the section is reinforced adding layers of fir wood to a base of $5mm$ thickness. The formulas above have been implemented in a MATLAB® script. In table 2.6 the results for different values of t_f at the constrained section are shown. The values used for calculations are $w = 100mm$, $h = 70mm$, $t_b = 1.5mm$.

From the results, it is evident that, since the height h is fixed, the thicker is the section and the smaller are the decreases in the maximum stress. Taking a maximum thickness of $20mm$ and considering a bending strength of $70MPa$ a good safety margin of $n = 70/42 = 1.67$ is obtained for fir wood. For birch plywood, the bending strength is $110MPa$ so a factor $n = 110/54 = 2.04$ is obtained.
Considering a reduction in thickness of $5mm$ at each rib (which is located every $150mm$, starting from the first one at the fuselage), the maximum stress is calculated at different cross-sections in order to verify that the value does not exceed the constrained section value. The results are shown in tables 2.8 and 2.7. It is evident that if the reduction in thickness occurs too early, the maximum stress value at a certain section may exceed the value calculated at the constrained section, thus tapering the beam loses its structural effect. For this reason, the reductions in thickness will occur farther from the constrained end, especially the last reduction from $10mm$ to $5mm$. The taper of the beam will be defined with more accuracy through the finite element analysis.

$t_{f(z=0)}[mm]$	$\sigma_{max(z=0)}$	$\sigma_{max(z=0.15)}$	$\sigma_{max(z=0.3)}$	$\sigma_{max(z=0.45)}$	$\sigma_{max(z=0.6)}$
25	39	35	32	30	30
20	42	40	41	49	–
15	47	50	67	–	–
10	59	83	–	–	–

Table 2.7: Maximum stress values at different cross-sections for the fir beams. Stress values are in $[MPa]$.

$t_{f(z=0)}[mm]$	$\sigma_{max(z=0)}$	$\sigma_{max(z=0.15)}$	$\sigma_{max(z=0.3)}$	$\sigma_{max(z=0.45)}$	$\sigma_{max(z=0.6)}$
25	51	49	42	39	39
20	54	52	53	64	–
15	61	65	87	–	–
10	77	107	–	–	–

Table 2.8: Maximum stress values at different cross-sections for the birch plywood reinforcements. Stress values are in $[MPa]$.

2.4 Finite elements analysis

The sizing of a complex structure such as the wing of an aircraft requires a finite element model on which the constraints and pressure loads will be applied in order to obtain a solution. Four load conditions will be investigated, corresponding to the four points on the $V - n$ diagram A,D,E,G. The software that has been used is the ANSYS® APDL interface, which allows to create an input code in a form of a programming language, granting a more immediate user-control than, in example, the ANSYS Workbench interface.

2.4.1 Modeling and elements setup

The ADPL interface allows the user to create a 3D model of the structure, giving *keypoints* in input. These keypoints are then used to make lines and areas that will form the model on which the mesh will be built. However, the ADPL modeler is not so handy when it comes to complex models. For this cases, a CAD model is created with an external software (such as SolidWorks®) and then exported in the *Parasolid* format, that the APDL interface can easily read converting the entities to keypoints, lines and areas.
Fortunately, the structure of a wing consist in different components that can all be modeled using planar elements. This is an advantage, because gives the possibility to obtain a simple model which is easy to calculate keeping a close relationship with the real behavior of the structure. For this reason, the wing has been model in SolidWorks® only

with surfaces.
Two element types have been used for this model: the SHELL 181 to model the surfaces of main and front spars, ribs and skin, while the BEAM 188 to model the back spar, the tip spar and the tip axle.
SHELL 181 is a four-node shell element with six degrees of freedom per node: three translations (*UX,UY,UZ*) and three rotation about the principal axes (*ROTX,ROTY,ROTZ*). It is suitable for analyzing thin to moderately-thick shell structures [5]. The degenerate triangular option is not recommended, since for a triangular element the stress is constant through the entire element, giving non-realistic stress values. However, it can be used for filling small regions of mesh where required. The shell element can be associated with different sections to model different thicknesses and layered composites.
BEAM 188 is a 3D beam with two nodes, with six degrees of freedom at each node, as described above for shell nodes. It is suitable for modeling slender to moderately thick shell structures. The element is based on Timoshenko beam theory, including shear-deformation effects. A quadratic or cubic behavior can be given to the element for a better representation of stresses. The beam element can be associated to different cross-sections. The command that is given in the APDL input file to specify the element type and its options (like quadratic behavior) is the following, taking as example the beam element[1]:

```
ET,1,BEAM188
KEYOPT,1,1,0
KEYOPT,1,2,0
KEYOPT,1,3,2
...
```

2.4.2 Material models

The material mechanical properties must be set into the APDL interface before setting up the sections, since layered section require material data inputs. The table reports the data given for different materials. The material number correspond to the materials described above in the following way:

1. Silver Fir wood;
2. Birch wood;
3. Flexyfoam;
4. Carbon-carbon;

[1] For a complete explanation of the commands, see [5]

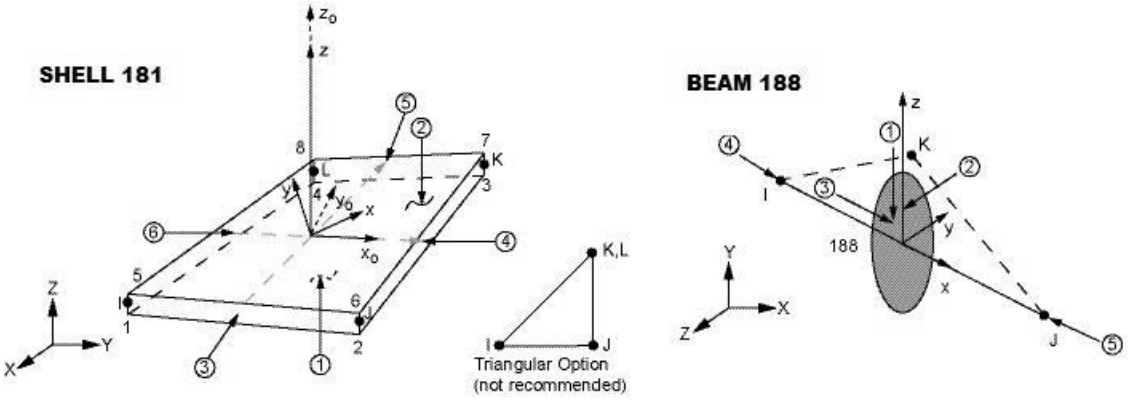

Figure 2.9: Elements SHELL 181 and BEAM 188 geometries [5]

5. Aluminum;

6. Glass fiber.

The material properties must be specified in the input file as follows:

```
MPTEMP,1,0
MPDATA,EX,1,,10.5e9
MPDATA,EY,1,,0.35e9
MPDATA,PRXY,1,,0.33
MPDATA,GXY,1,,0.82e9
MPDATA,GYZ,1,,0.07e9
MPDATA,GXZ,1,,0.67e9
MPDATA,DENS,1,,400
```

The orthotropic properties have been given with respect to the xyz element coordinate system. In fact, each element has a local coordinate system that must be specified accurately to avoid to give non-realistic properties to the model. The local x axis corresponds to the grain direction in the case of woods, or fiber direction in the case of composites. The y axis is the direction tangential to the growth rings in the case of wood, or the in-plane direction perpendicular to the fibers in the case of composites. Since all the elements have at maximum two dimensions, the value of the modulus of elasticity in the z direction can be neglected, as well as the Poisson's ratios in the yz and xz planes, that for simplicity have been set equal to the ratio in the xy plane. The properties for wooden material have been chosen as an average between the values reported by different sources. The shear moduli have been taken from the FPL Wood Handbook [12].

Material number	1	2	3	4	5	6
Density $[kg/m^3]$	400	720	130	1600	2780	1630
E_x $[Pa]$	$10.5 \cdot 10^9$	$13 \cdot 10^9$	$0.108 \cdot 10^9$	$80 \cdot 10^9$	$70 \cdot 10^9$	$13 \cdot 10^9$
E_y $[Pa]$	$0.35 \cdot 10^9$	$0.75 \cdot 10^9$	–	–	–	$10.5 \cdot 10^9$
ν_{xy}	0.33	0.45	0.49	0.33	0.33	0.24
G_{xy} $[Pa]$	$0.82 \cdot 10^9$	$1.02 \cdot 10^9$	–	–	–	$4.14 \cdot 10^9$
G_{yz} $[Pa]$	$0.07 \cdot 10^9$	$0.255 \cdot 10^9$	–	–	–	$3.9 \cdot 10^9$
G_{xz} $[Pa]$	$0.67 \cdot 10^9$	$1.11 \cdot 10^9$	–	–	–	$3.9 \cdot 10^9$

Table 2.9: Material properties that have been inputed in the APDL.

The strength values that have been considered for evaluating the failure of the material are shown in table 2.10.

Material number	1	2	3	4	5	6
Strength, x tension $[MPa]$	70	110	3.8	1200	570	200
Strength, x compression $[MPa]$	-36	-55	-2.6	–	–	-150
Strength, y tension $[MPa]$	1.2	86	–	–	–	36
Strength, y compression $[MPa]$	1.3	6.3	–	–	–	30
Strength, xy shear $[MPa]$	4.6	15	2.3	–	–	2.3

Table 2.10: Strength values of the considered materials.

2.4.3 Sections

Each element, beam or shell, needs section data specifications to simulate a three-dimensional behavior. In the section data, a laminate composite can be also created, inputing for each layer the material, its thickness and its orientation with respect to the local coordinate system x axis.
The sections that have been associated to beam elements are two, one for the carbon tube and one for the aluminum axle. For the shell elements, a total of eight sections have been set. Five of these are used to model the different thicknesses of the fir beams, and have been approximated as single-layer homogeneous sections. In fact, five different thicknesses have been used, respectively of 5, 10, 15, 20 and $25mm$. Another single-layer section is used for the ribs, with a constant thickness of $10mm$. The input data for the two layered sections, one for the skin and one for the plywood reinforcements, are shown in figures 2.10 and 2.11.

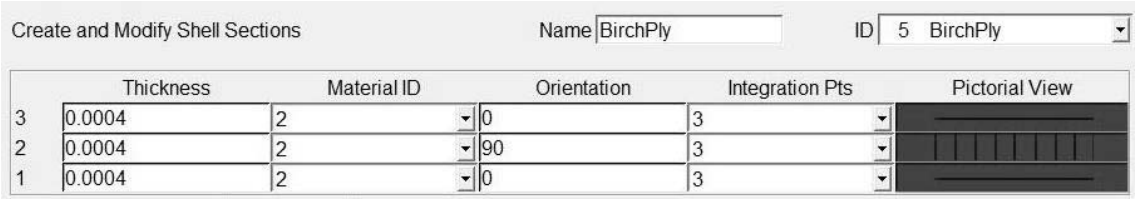

Figure 2.10: APDL window for shell section data input, birch plywood.

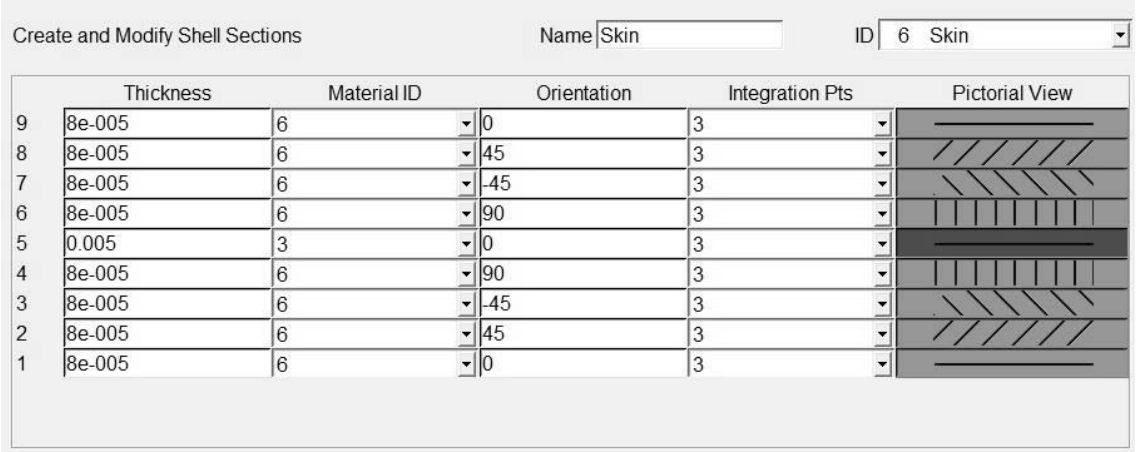

Figure 2.11: APDL window for shell section data input, laminate for the wing skin.

2.4.4 Mesh

At this point, all the information required for meshing the geometric model have been given to the program, except the mesh size. A good method for controlling the mesh size and making the mesh the most regular as possible is to give a number of divisions to the lines in the model. In example, if the lines at the boundaries of a rectangular area have been divided respectively in a m and n number of one-dimensional elements, the relative area will be divided in $m \times n$ two-dimensional elements.
Instead of inputing the number of divisions, the element edge length can be set. The program will automatically calculate the finite number of divisions for each line by dividing the total line length for the element edge length, rounding up to the nearest integer. This is the best method when the exact length of the lines is not known. The average size given for all lines is $50mm$, leading to a light mesh, but with enough elements to make it suitable for a good first sizing.
The lines defining the carbon beams and the axle have been meshed with the same settings, having at least three beam elements between each couple of ribs.
The different sections defined for the fir beams have been associated to different areas. The thickest section of $25mm$ has been associated to areas located from the beginning

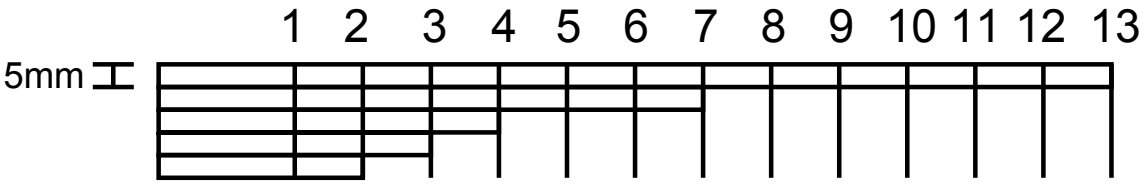

Figure 2.12: Reduction of thickness on the main spar beams. The numbers above are the numbers of the ribs, located every $150mm$. The total beam length is $2.1m$.

of the spar to the second rib, for a total length of $300 + 150 = 450mm$. The section of $20mm$ thickness has been associated with areas from the second to the third spar, the one of $15mm$ thickness with areas from the third to the fourth and the one of $10mm$ thickness with areas from the fourth to the seventh. The remaining part of the fir beam has been associated with the section of $5mm$ thickness. Figure 2.12 shows the variation of thickness at the different ribs.

2.4.5 Loads and boundary conditions

The most complicated part when dealing with a coupled cfd-structural analysis (also called FSI, *fluid-solid interface*) is related to transferring the load data from the results of the cfd analysis to the mechanical model. Different solutions are offered from the software in this cases. ANSYS Workbench® allows to create two different analysis on the same project. First, the cfd analysis must be solved, then the pressure distribution can be transferred to the solid model creating a link between a surface specified in the cfd model to the corresponding surface in the structural model. If working with Workbench, this is for sure the easiest way; however, as written above, the Workbench interface does not offer the same flexibility and user-control over the project as the APDL interface. For this reason, this method has not been followed.
Fortunately, FLUENT offers the possibility to create an input file for fluid pressure loads for all the main FEA softwares, including APDL mechanical and PATRAN/NASTRAN®. In order to create this file, FLUENT needs in input the mesh of the surface created in the structural pre-processing phase. Then, the program applies the pressure on the surface directly on the nodes of the structural mesh. However, it is fundamental that the surfaces location with respect to the global Cartesian coordinate system coincide in both models. For this reason it is recommended to create the cfd geometry file with respect to the same coordinate system that will be used when creating the geometry for structural analysis.

The boundary conditions that are applied to the structural model must be chosen accurately in order to obtain the best simulation of the real behavior of the structure. The first important assumption is that the spar box is perfectly rigid. It is a good assumption for a safe-sizing; however, a successive and more accurate structural analysis must

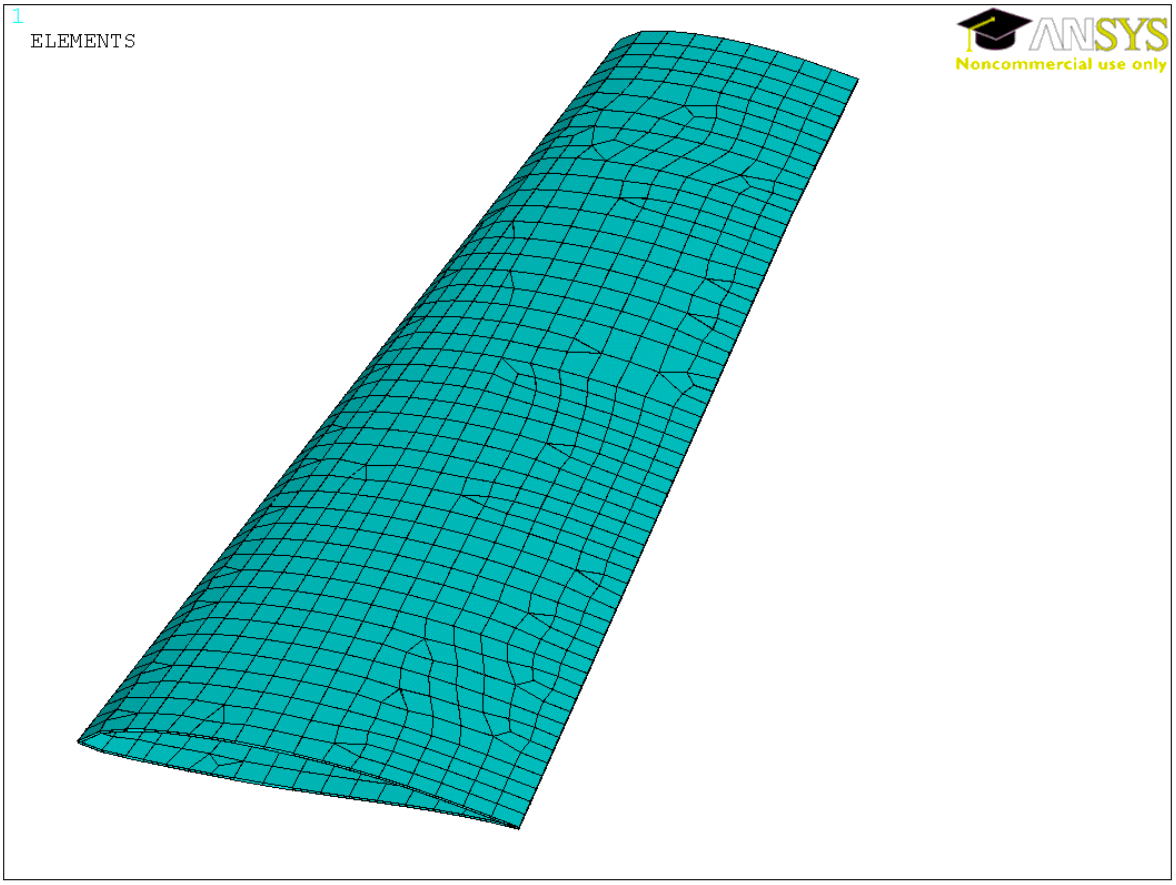

Figure 2.13: Line divisions and relative mesh of the wing skin.

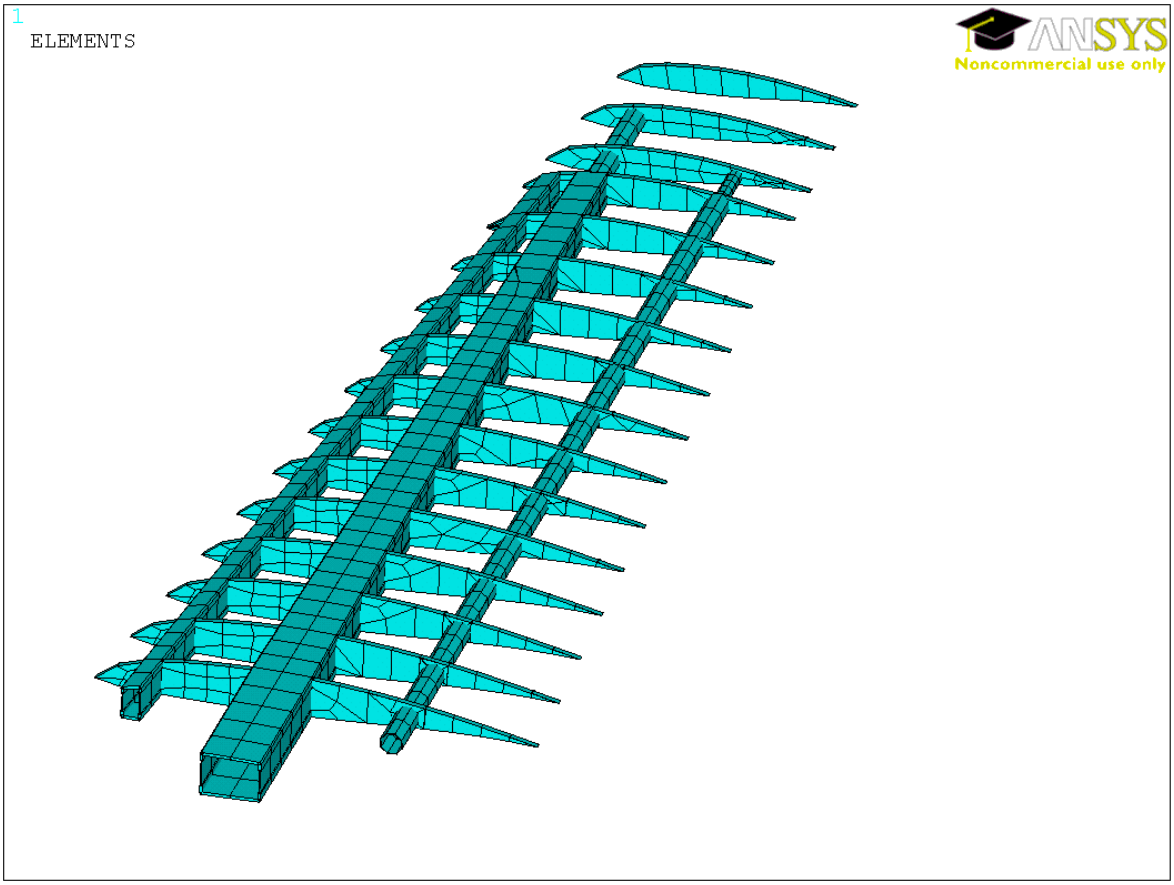

Figure 2.14: Mesh of the inner structure of the wing.

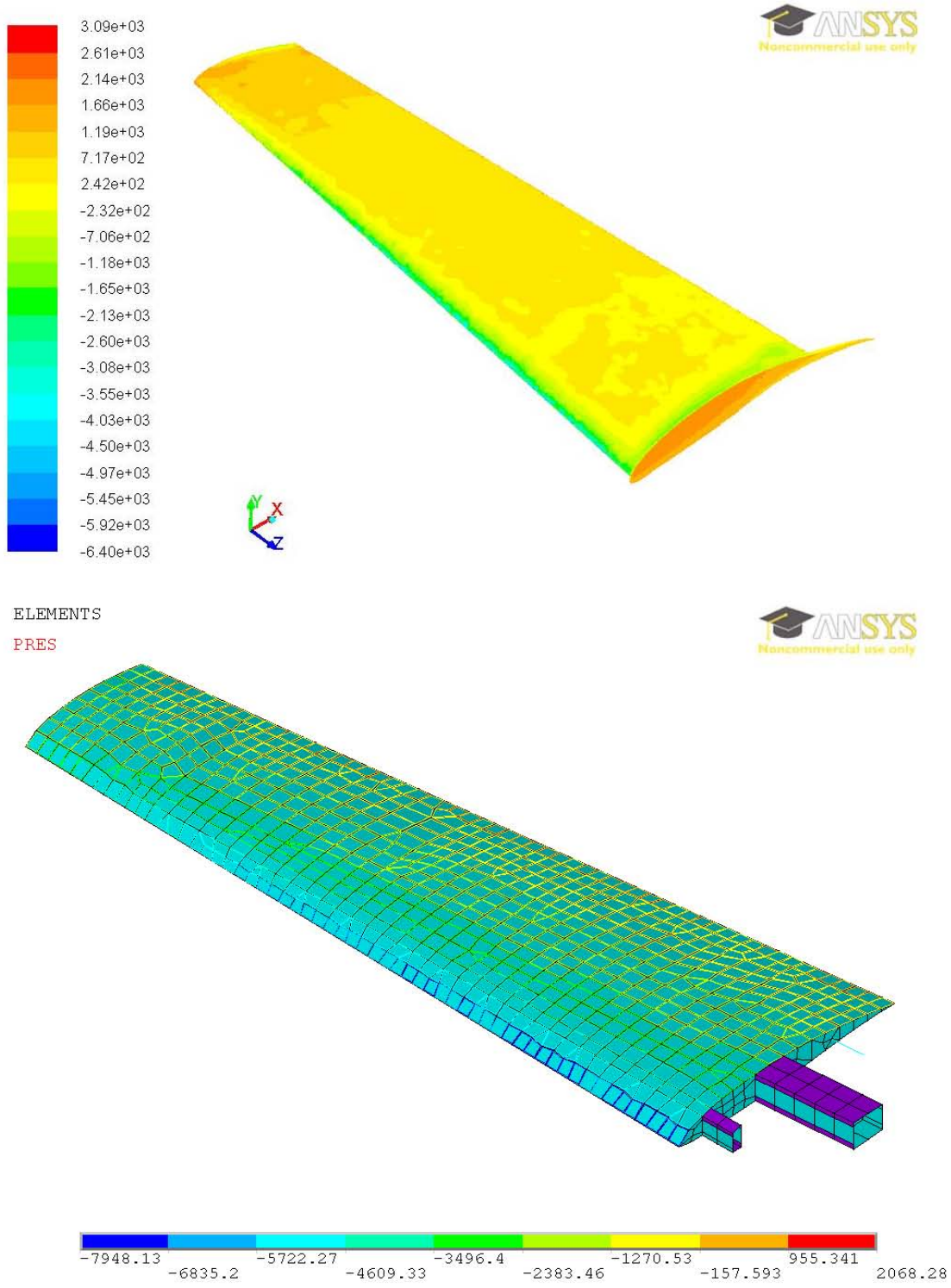

Figure 2.15: Relative pressure contour in the fluent model of the wing and correspondent pressure load in the APDL interface.

consider the spar box FE model to size the thickness of the walls and the connections to the fuselage.
Considering the spar box perfectly rigid corresponds to blocking the vertical and lateral displacement of the part of the spar which is introduced into the box. In the model, this translates in blocking the UX and UY displacement of the interested areas. The constraint of the longitudinal displacement (in other words, blocking the wing so that it does not pull off) is granted by the bolted connection. In this model, since the connection has not been modeled for simplicity, a fixed constraint (blocking all six degrees of freedom) has been given to the lines at the very beginning of the main spar. In addition, since the front spar and the back will be simply glued to the fuselage wall, other two fixed constraints have been given to their inner end. The figure 2.16 shows the detail of the constraints.

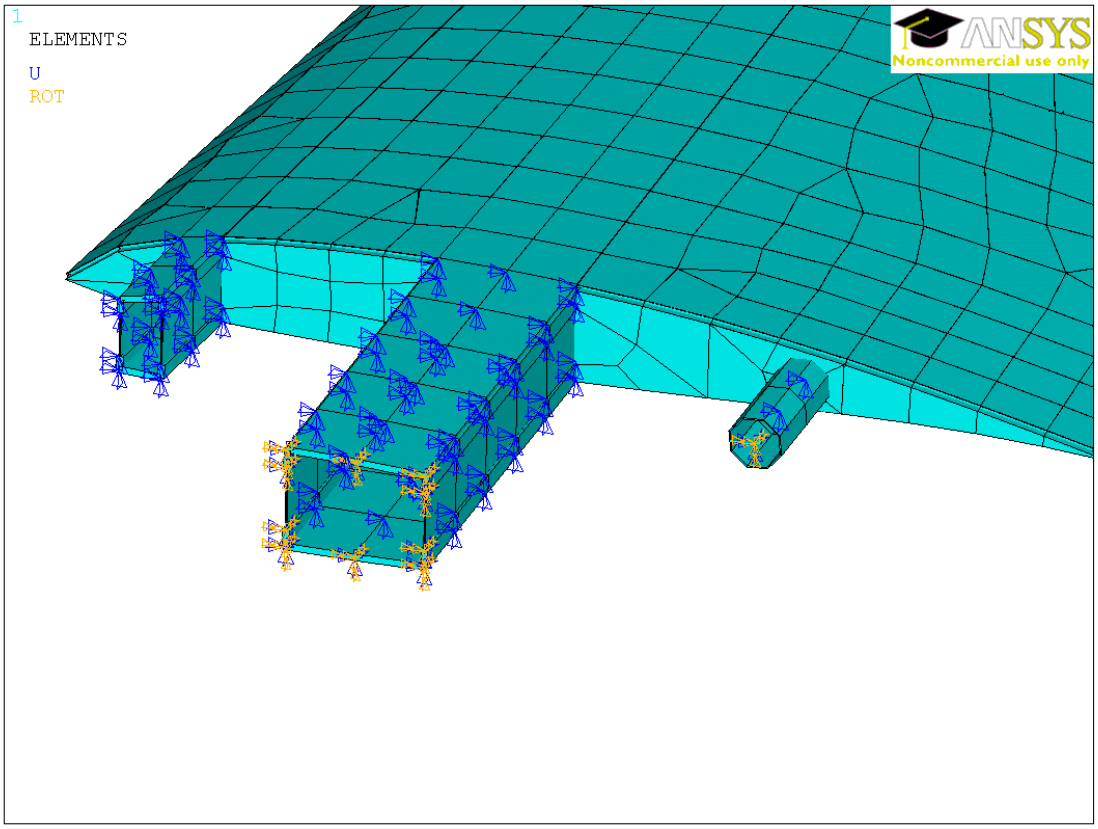

Figure 2.16: Boundary conditions that simulate the connection between wing and fuselage.

2.5 FEA Results

The solution has been obtained with a simple static analysis. The number of solutions is four, one for each point A, D, E and G. The overall mass of the wing computed by the software is approximately $8.4kg$. However, the real mass of the wing will be higher, since additional mass of the flap spar and the glue must be added.
Since the worst load conditions occur at points A and D, the sizing is mainly made upon the solutions obtained at these two points. The maximum displacement occurs at the end of the wingtip, and the values obtained for cases A and D are very similar, with a $\delta_{max,A} \approx \delta_{max,D} = 122mm$. Such value is not negligible if a detailed aerodynamic solution is desired. In fact, this value of the displacement adds an effective dihedral angle of

$$\theta_{dihedral} = arctan\frac{122}{2500} = 2.8^{\circ} \tag{2.5.1}$$

Thus, the aerodynamic forces should be recalculated taking into account the deflection of the wing. This leads to an aeroelastic analysis, which can be made coupling a fluid solver with a structural solver. This type of analysis requires an accurate set-up, and it is beyond the aim of this work. However, since the main purpose of this thesis is to size the main structural elements, neglecting the aeroelastic effect leads to acceptable results anyway.
The stress values are shown for the different parts of the structure. The maximum stress on the spars is shown in figure 2.18. The selected reduction in thickness has the effect of concentrating the stress only at the interface with the fuselage. The maximum value for the case A is $27MPa$, and for case D is $26MPa$. The safety factor obtained in this way is calculated considering the highest value of stress:

$$n_{spar} = \frac{70}{27} = 2.59 \tag{2.5.2}$$

which is an acceptable value. It is worth considering that wood does not exhibit a yield behavior like metallic materials: instead, wood has a "proportional limit" stress value, above which the relation between the stress and the displacement is not linear any more. For fir wood, this value is estimated to be approximately $5000psi(\approx 35MPa)$ [2]. Thus, it is good to have the maximum value of stress below the proportional limit, so the linear relation that is assumed by the APDL interface is still valid.

The maximum stress value for plywood reinforcements occurs at the intersection with the fuselage. Stress is higher for the front spar, due to the high value of pitching moment. The results of this analysis show a maximum value of approximately $27MPa$, thus a coefficient of safety of

$$n_{birch} = \frac{110}{24} = 4.58 \tag{2.5.3}$$

However, due to the shape of the plywood reinforcements, the possibility of buckling failure should be considered. To investigate this, a buckling analysis could be useful.

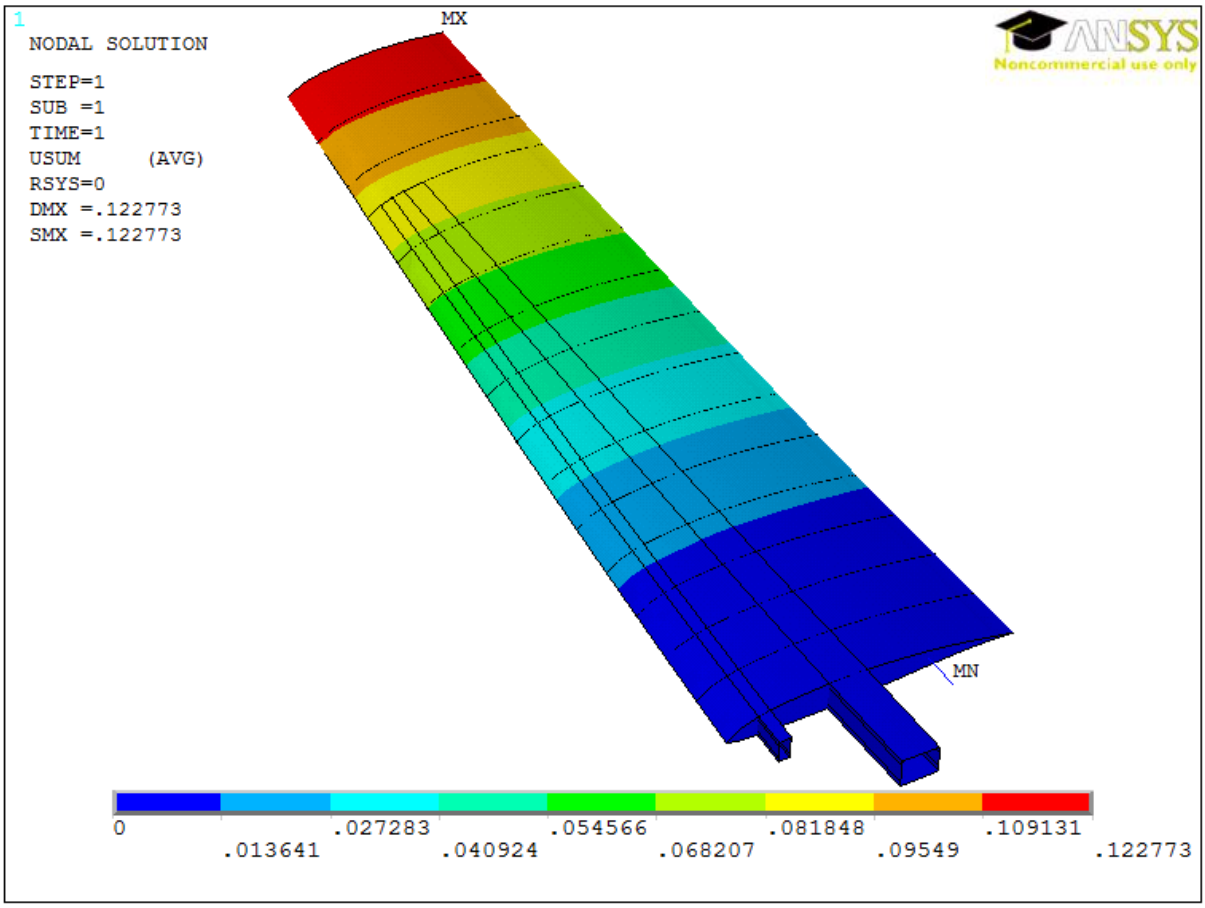

Figure 2.17: Displacement vector sum, case A.

However, to avoid this it may be enough to choose a different thickness for the reinforcements at the beginning of the spar. A new analysis has been done considering a thickness of $1.5mm$ instead of a thickness of $1.2mm$, thus increasing the thickness of only $0.3mm$. The stress obtained is $21MPa$, which is the 20% less than the previous value.

On the ribs, there are no particular stress concentrations. However, a buckling analysis could be useful here too. The coarse mesh does not allow to see the stress details at the interface between the ribs and the spars, so a more detailed model may be required. The back spar show a high concentration of stress of $133MPa$ at the constrained section. This value is overestimated, since part of the load in the back part of the structure will be carried by the flap spar. However, it is well below the carbon-carbon strength in tension of $1200MPa$ ([24]). The skin shows a concentration of stress in the area between the two main spars. The stress distribution is not continuous, since in the model the skin has been considered to be "glued" to the upper and lower surfaces of the spars.

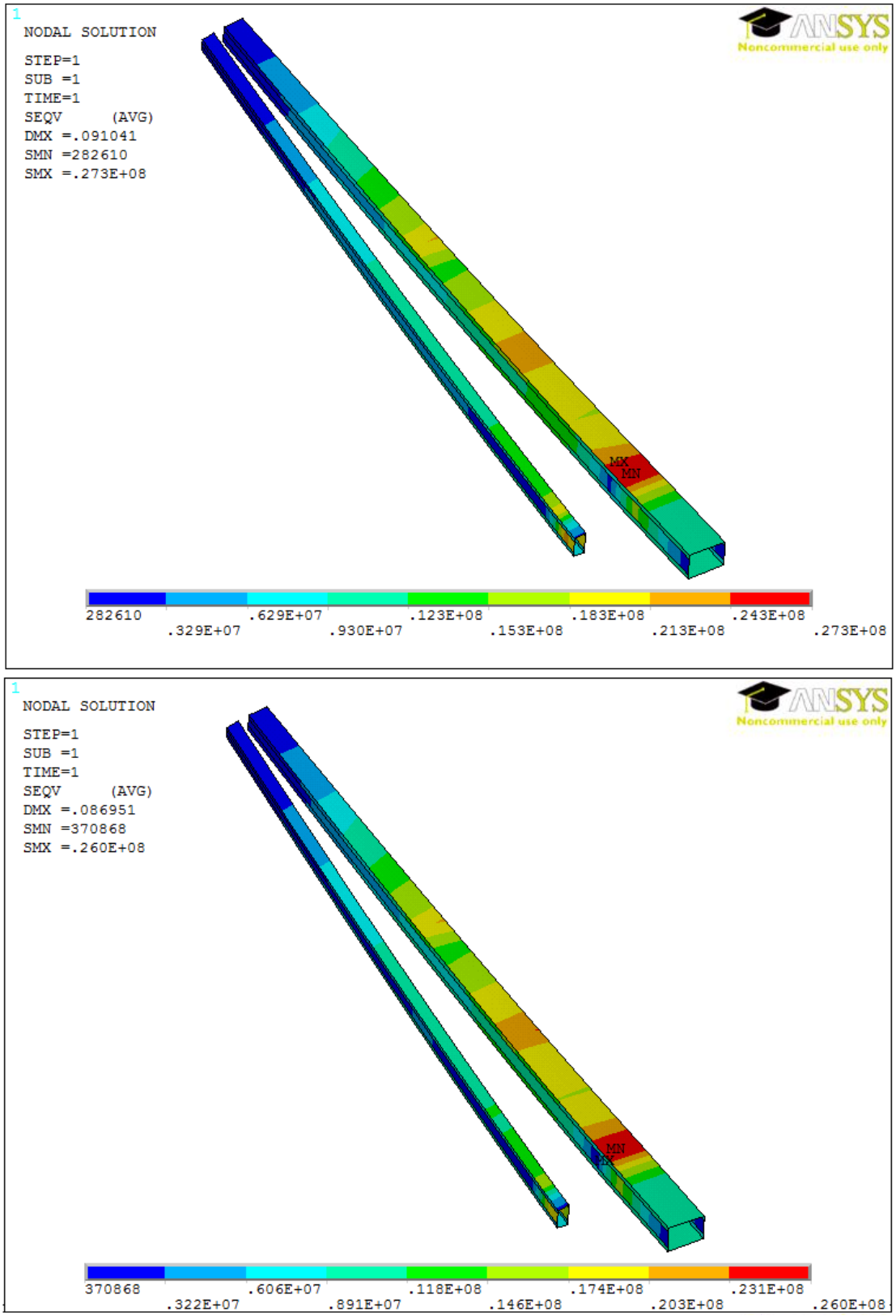

Figure 2.18: Maximum stress in the spars, cases A (above) and D.

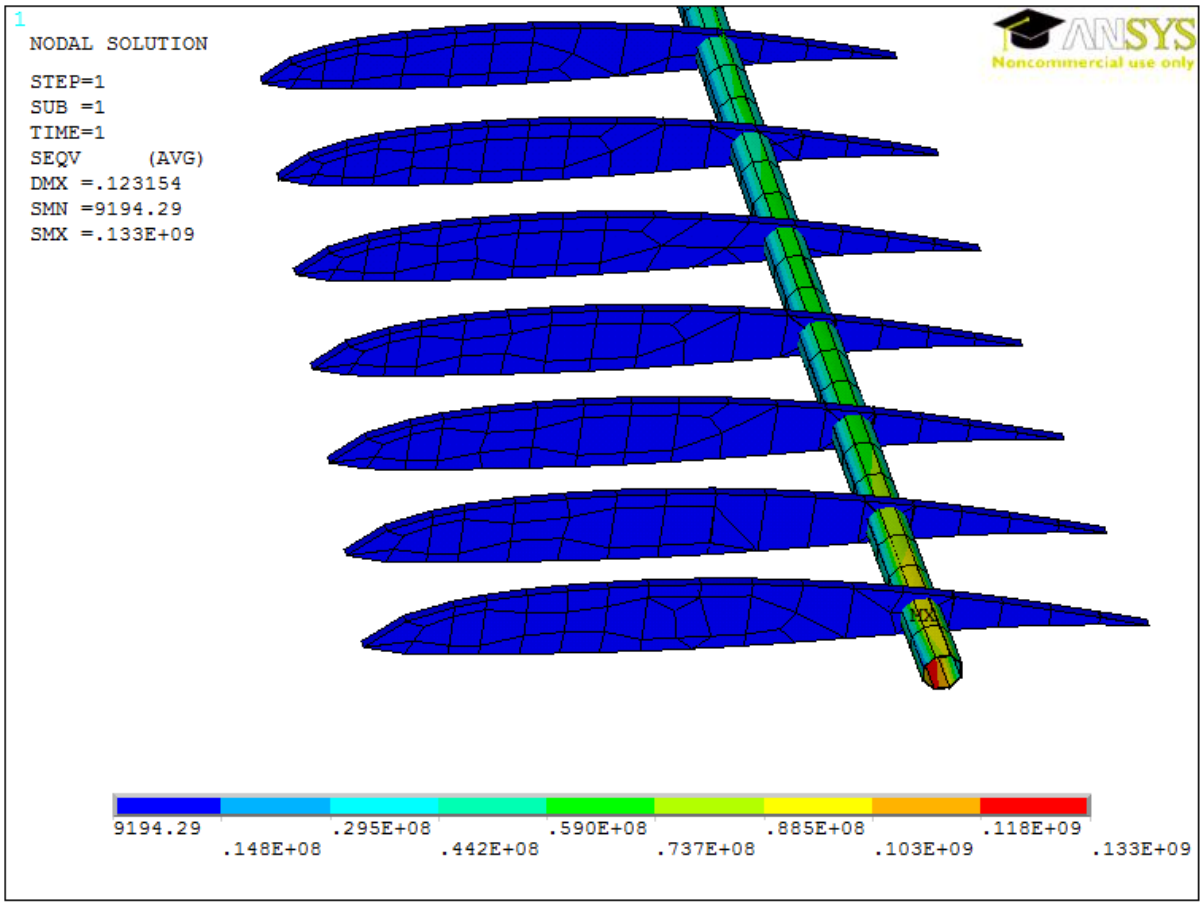

Figure 2.19: Detail of stress distribution on ribs and back spar, case A.

The maximum tension is about $33MPa$ (figure 2.20). The stress values are much lower than the ones found by Baldon ([7]), however a detailed failure analysis could confirm the strength of the structure.
The other two cases, E and G, do not show particular concentrations of stress that may exceed those obtained for points A and D. Thus, the results for these two points are reported here just for comparison. The static structural analysis showed that the structure is able to withstand the given load conditions. A more accurate analysis may be done, where dynamic effects are considered, in order to verify the resistance of the structure to buckling, flutter and other dynamic phenomena.

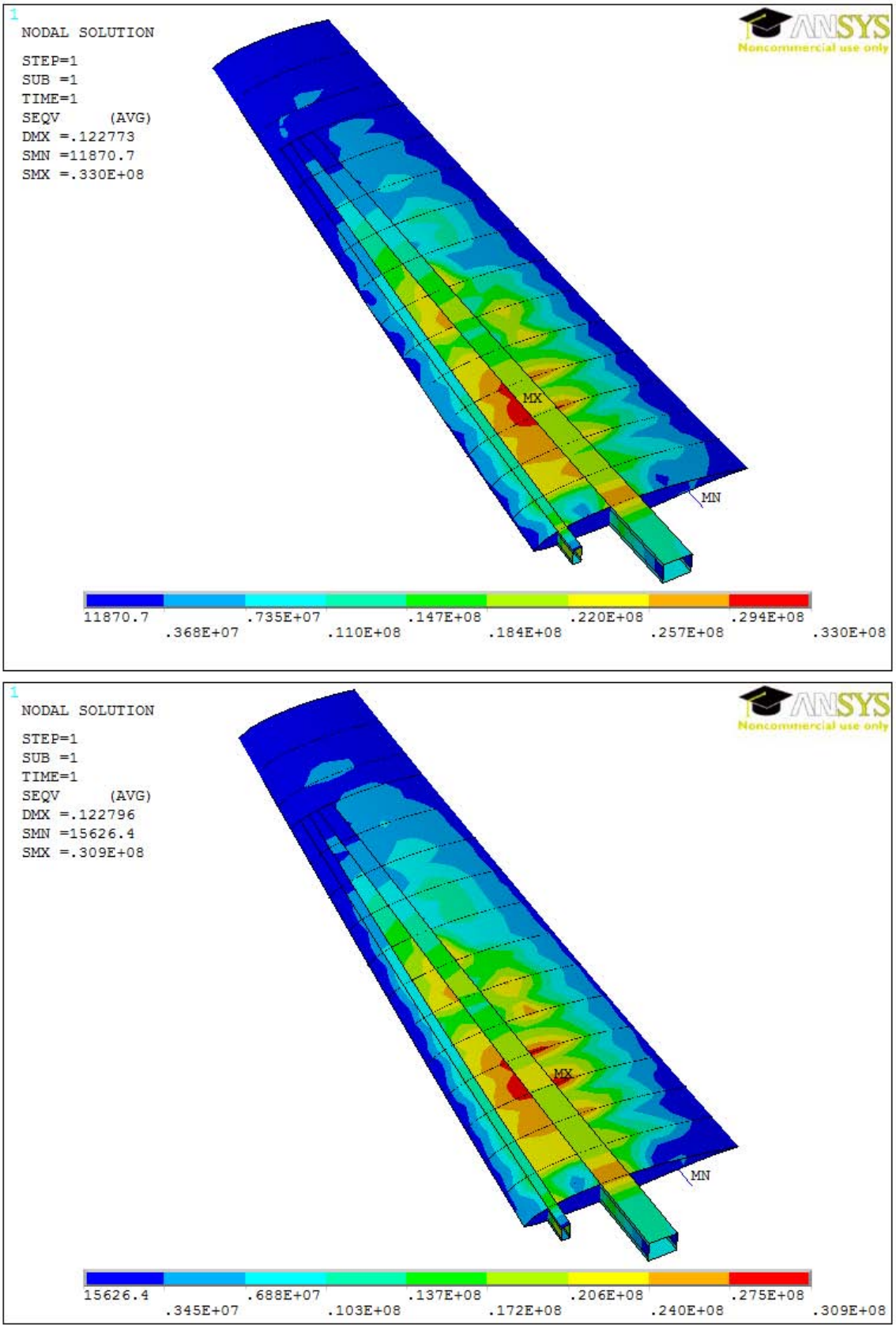

Figure 2.20: Maximum stress in the skin, cases A (above) and D.

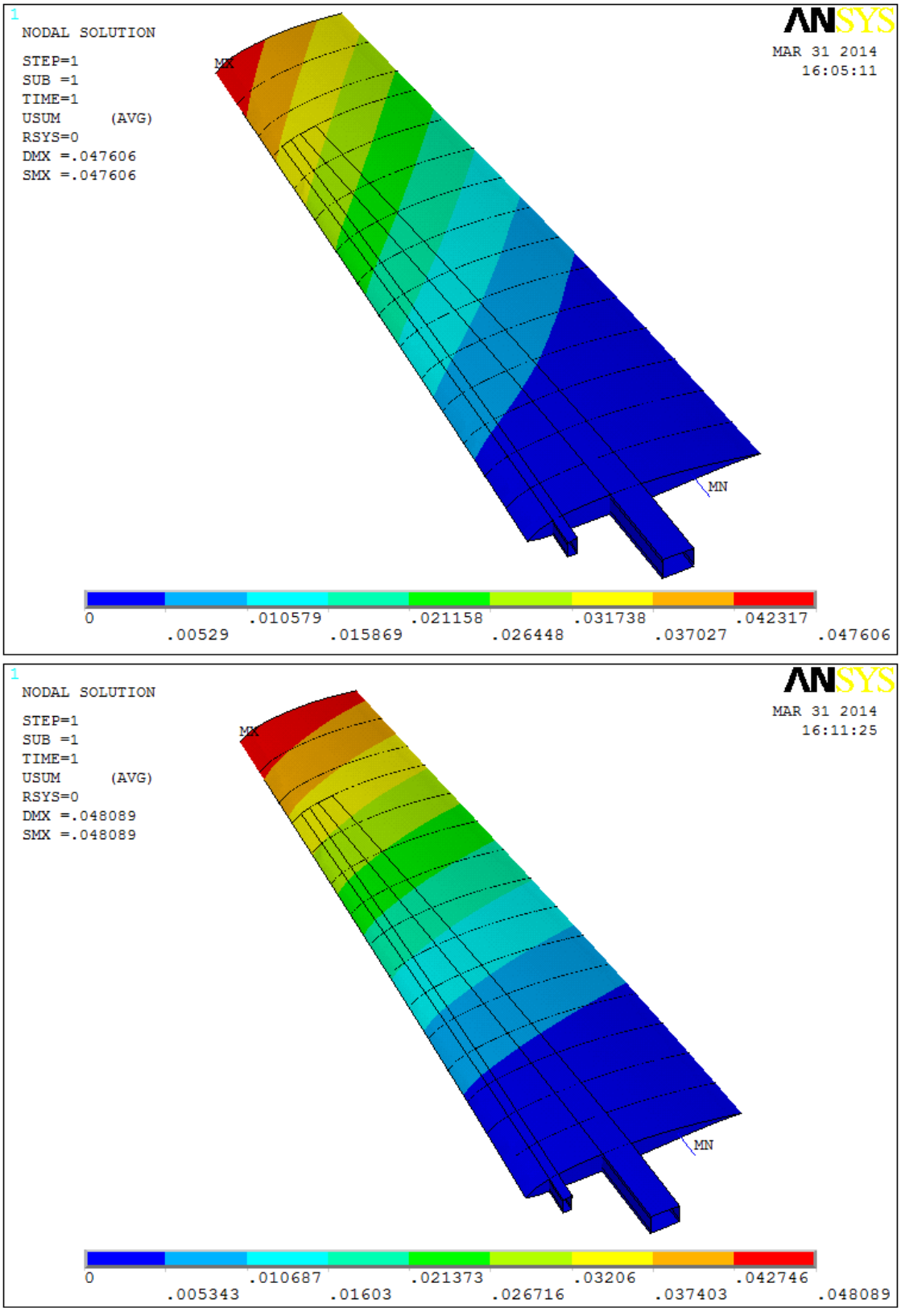

Figure 2.21: Displacement vector sum, cases E (above) and G.

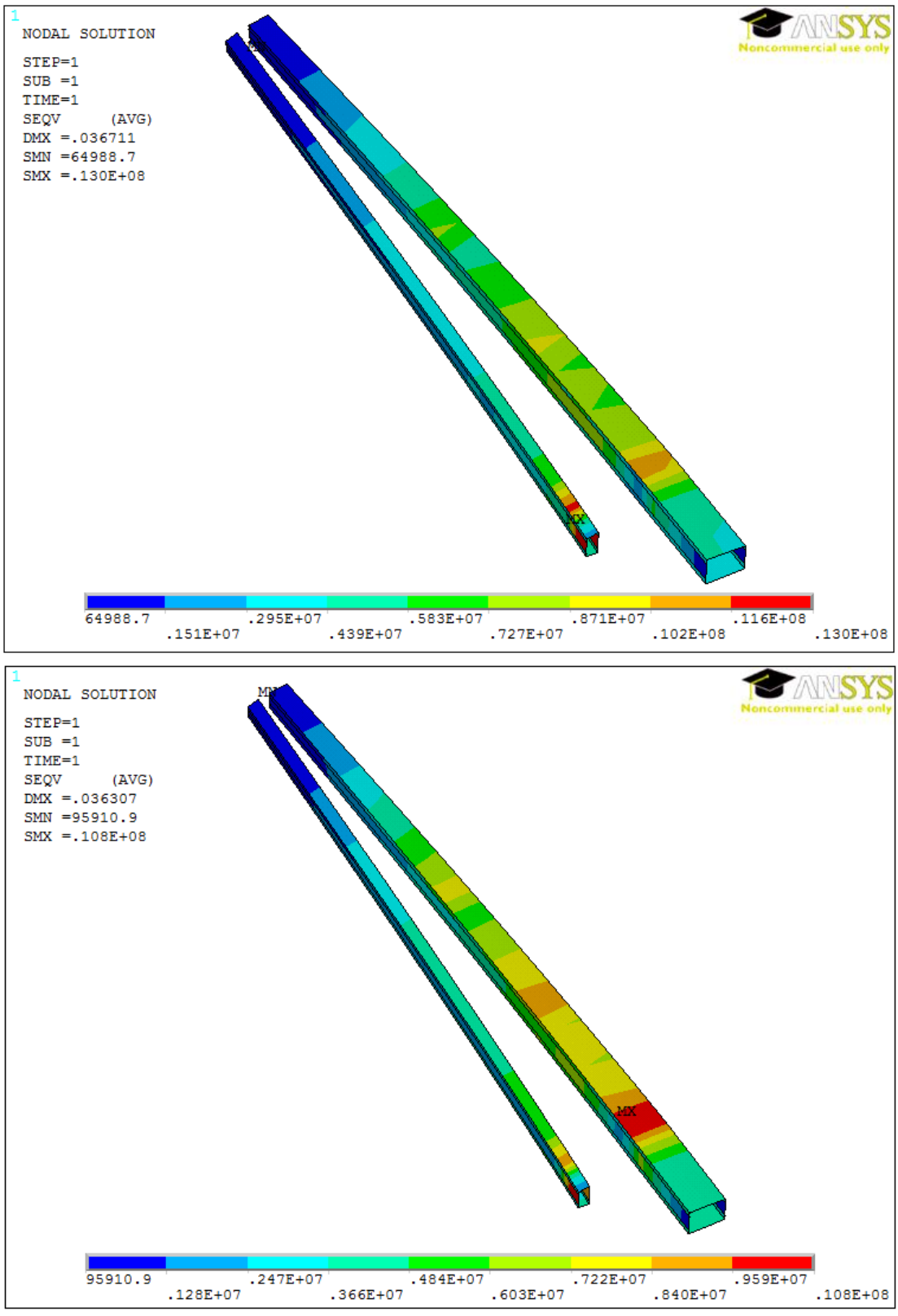

Figure 2.22: Maximum stress in the spars, cases E (above) and G.

Chapter 3

The Landing Gear

In this chapter, the design of the main landing gear leg of the Merlo is presented. An aluminum pipe gear leg has previously been designed and analyzed by Gori [13]. Professor Sambin required further investigation about the possibility to obtain a more flexible shock absorbing system, selecting a solid-spring gear leg. The purpose of this chapter is to design a landing gear of this type, verifying the structure with analytical calculations and then with a finite element analysis. In addition, an estimate of the fatigue life of the component has been carried out, following an approximated method.

3.1 Landing gear sizing

The landing gear type selected for the Merlo is a common taildragger. It consists of a two-wheels main landing gear located in advanced position with respect of the center of gravity, and a small tailwheel mounted on the rudder. This choice leads to larger propeller clearance, less drag and weight, and shortens the takeoff distance since the wing has a higher angle of attack on the ground. However, it is a less stable configuration with respect to a tricycle gear, and requires more ability from the pilot, in order to avoid the "ground loop" while moving on the runway.
The sizing procedure that has been adopted here is taken from Raymer, chapter 11 [24]. First, the requirements of the shock-absorbing system are specified, and then the landing gear leg geometry is defined.

3.1.1 Shock-absorbing system sizing

The landing gear main purpose is to absorb the shock at landing, in order to avoid an excessive vertical deceleration that may lead to unbearable loads on the structure. The norm[1] prescribes to verify the efficiency of the landing gear at a vertical impact speed of

[1] DPR 133, paragraph 473

$V_{vert} = 1.6m/s$. The test is done dropping the aircraft from a height of $0.13m$, and the deceleration that it is measured at the aircraft c.g. must not exceed $4g$. The landing gear must then provide a certain stroke to allow a smooth deceleration. The stroke is the vertical deflection of the shock-absorbing system. It can be calculated using the following formula obtained from Raymer's:

$$S = \frac{V_{vert}^2}{2g\eta N_{gear}} - \frac{\eta_T}{\eta} S_T \tag{3.1.1}$$

where η is the landing gear efficiency factor, N_{gear} is the load factor, η_T is the tire efficiency and S_T is the tire stroke.
The efficiency factors are taken from the literature [24]. A solid leaf spring has an efficiency of $\eta = 0.5$, while for the tires a value of $\eta_T = 0.47$ can be used. The landing gear load factor represents the vertical deceleration rate. It affects the load that must be applied to the structure in order to simulate the impact at landing. The norm prescribes a value of $N_{gear} = 3$. The stroke provided by the tire is related to its dimensions and its inner pressure. At the moment, a value of $50mm$ can be used. This value will be justified later in during the tire sizing.
The values that have been specified above have been substituted into the stroke formula, giving a landing gear stroke of $S = 40mm$. Raymer suggests to increase this value of approximately $1in$ $(25mm)$ for safety, giving $S = 65mm$. This value will be used later in the structural analysis as a requirement.

3.1.2 Tire sizing

In the taildragger configuration, approximately the 90% of the aircraft weight is carried by the main landing gear tires. Considering this weight fraction for the Merlo, each tire of the main landing gear must carry a weight of:

$$W_w = 0.45W = 0.45 \cdot 180 \cdot 9.81 = 794.6N = 369.8lbf$$

A statistical method based upon solutions adopted for similar-size aircrafts can be used. The tire external diameter and width in inches are calculated with the following statistical expression, considering general aviation aircrafts. The weight must be expressed in lbf.

$$\emptyset_t = 1.51W_w^{0.349} = 11.89in = 302mm$$

$$w_t = 0.715W_w^{0.312} = 4.52in = 115mm$$

With a first size of the tire diameter, a suitable wheel for Merlo can be chosen. The wheel, in technical terminology, is the circular object on which the tire is mounted. Most of the aircrafts use metallic wheels; however, in order to save weight, the choice of another material has been considered. A very good weight-saving option has been

individuated in the *Azusalites* wheel series made by Azusa Engineering[2]. These wheels are made in engineering grade Nylon, and offer a good strength with very low weight if compared with aluminum. The AZUSALITE 4" model has been chosen. It has a width of $3.5in(89mm)$ and a diameter of $4in(102mm)$, and mounts a $410/350 \times 4'$ tire of $\emptyset_t = 10.5in(267mm)$ diameter, weighing only $1lb$ $(0.45kg)$. The dimensions are smaller than the calculated values, since Merlo is much lighter than the common general aviation aircrafts.
The weight acting on tires is entirely carried by the tire internal pressure. Considering the contact area between the tire and the pavement A_p, the carried load can be expressed with the simple relation

$$W_w = pA_p \tag{3.1.2}$$

where p is the tire internal pressure. The contact area of the tire can be expressed as a function of the tire dimensions:

$$A_p = 2.3\sqrt{wd}\left(\frac{d}{2} - R_r\right) \tag{3.1.3}$$

where w is the tire width, d is the external diameter and R_r is the rolling radius, that is the radius of the tire when under load. From the formula it is evident that, if w, d and W_w are given, the rolling radius depends only on the internal pressure. A pressure value of $p = 25psi = 1.7atm$ is considered the maximum allowable value from the manufacturer. However, the tire may work at lower inner pressures in order to have a larger rolling radius. This increases the life of the tire, but it must be verified that the wheel radius does not exceed the new rolling radius obtained for a lower pressure. Having a smaller rolling radius is useful to better absorb the shock at landing. In fact, the tire stroke is given by:

$$S_T = \frac{d}{2} - R_r \tag{3.1.4}$$

During the calculations of the stroke, a value of $S_T = 50mm$ has been considered. This means that the wheel rolling radius at the landing impact is:

$$R_r = \frac{d}{2} - S_T = 83.5mm$$

This value implies a specific inflation pressure, which can be found rearranging the equation above. The load acting on the tire at the landing impact is given by:

$$F = \frac{1}{2}WN_{gear} \approx 2700N \tag{3.1.5}$$

[2]www.azusaeng.com

To obtain the tire inner pressure, the calculated load must be substituted in the equation $(3.1.2)$:

$$p = \frac{F}{A_p} = \frac{F}{2.3\sqrt{wd}\left(\frac{d}{2} - R_r\right)} = 1.523 \cdot 10^5 Pa = 1.5atm = 22psi$$

The pressure value can be adjusted to obtain a larger stroke if needed during the drop test phase. The minimum allowable rolling radius corresponds to the tire inner radius (the wheel radius):

$$R_{r_{min}} = \frac{4 \cdot 25.4}{2} = 51mm$$

This means that, if required, the rolling radius can be further decreased until it reaches the minimum value, which corresponds to the maximum stroke from the tire. The maximum stroke can be obtained as a difference between the tire external radius and the minimum rolling radius:

$$S_{T_{max}} = \frac{d}{2} - R_{r_{min}} = 82.5mm$$

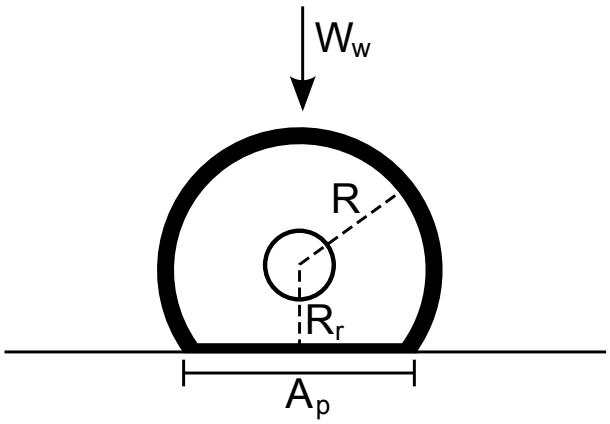

Figure 3.1: Wheel dimensions.

3.1.3 Geometry

The landing gear geometry is shown in figure 3.2. The position of the landing gear leg with respect to the aircraft center of gravity must follow some basic rules for granting the stability of the aircraft during the maneuvers on the ground [24]. The tail-down angle (β in figure 4.1) should be about $10 - 15°$. The angle that the vertical direction makes with the line connecting the wheel axle to the aircraft center of gravity (angle α in the figure) should be between $16°$ and $25°$. The angle should be large enough in order

to prevent the aircraft to nose-over; however, it should not be too much large otherwise the aircraft will tend to groundloop.
For lateral maneuvering stability, main wheels must be laterally separated by a length of $1200mm$, as calculated by Gori [13]. This leads to an inclination of an angle α_f with the vertical direction when the aircraft is seen from the front.

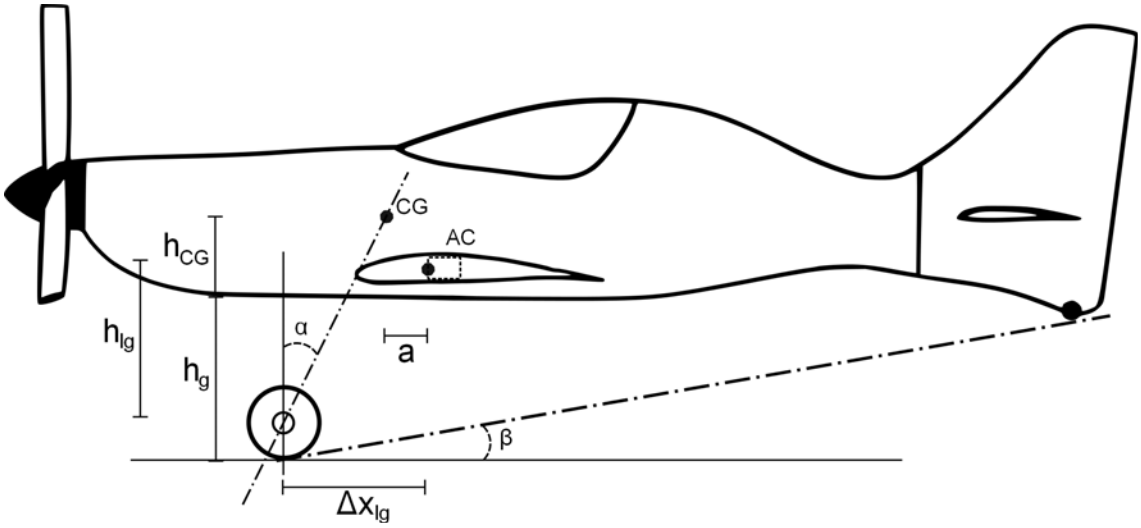

Figure 3.2: Position of the landing gear with respect to the aircraft center of gravity.

The height of the aircraft floor from the ground h_g must grant the minimum propeller clearance of $\Delta_{clear} = 250mm$ in every situation, including when the deflection of the landing gear plus the tire is maximum. Following the calculations done by Gori ([13], par. 3.2), the height from the ground is found:

$$h_g = \frac{\emptyset_{prop}}{2} + \Delta_{clear} - h_{CG} + S_{max} \tag{3.1.6}$$

where $\emptyset_{prop} = 1220mm$ is the propeller diameter, $h_{CG} = 260mm$ is the height of the c.g. from the aircraft floor and S_{max} is the maximum shock-absorber system stroke, rounded for safety to $100mm$. Substituting these values, a height from the ground of $h_g = 700mm$ is obtained.
Choosing an angle of $\alpha = 20°$ (which is an intermediate value in the interval given by Raymer) leads to an horizontal distance between the aircraft c.g. and the wheel axle of:

$$(h_g + h_{CG} - \frac{\emptyset_t}{2})tan(\alpha) = 301mm$$

Professor Sambin's intention is to connect the landing gear to the most stiff part of the aircraft, the spar box. The height of the landing gear leg is calculated knowing the

wheel diameter and the height of the spar box from the aircraft floor, which measures approximately $100mm$ (obtained from the CAD drawings):

$$h_{lg} = h_g + 100 - \frac{\emptyset_t}{2} = 666.5mm$$

The angle α_f can be chosen within a specific range. Since the semi-distance from the wheels must be of $d_w/2 = 600mm$ and the width of the fuselage at the landing gear section is approximately $w_f = 300mm$, the minimum angle is obtained from:

$$\alpha_{f_{min}} = arctan\left(\frac{\frac{d_w}{2} - w_f}{h_{lg}}\right) = 24.3^\circ \tag{3.1.7}$$

The maximum angle is given by:

$$\alpha_{f_{max}} = arctan\left(\frac{\frac{d_w}{2}}{h_{lg}}\right) = 42^\circ \tag{3.1.8}$$

A larger angle means a longer leg. For the following calculations, an intermediate angle of $\alpha_f = 35^\circ$ is chosen.
From the drawings, the front vertical wall of the spar box is located approximately at $250mm$ from the root leading edge. Its position can be approximated with the position of the aircraft aerodynamic center (as shown in figure 3.2). Stability requires that the a.c. is located approximately $70mm$ behind the c.g. (see chap. 1). Thus, the horizontal distance between the wheel axle and the spar box wall is

$$\Delta x_{lg} = 301 + 70 = 371mm$$

This means that, if a perpendicular leg is desired, it must be attached to the fuselage at a distance Δx_{lg} from the spar box, complicating the connecting structure. If connected directly to the spar box, the landing gear leg cannot be designed to be "planar" (with "planar" it is intended a gear leg that has both ends laying on the same vertical plane). Instead, it must be inclined toward the front of the aircraft of an angle of:

$$\alpha_s = arctan\left(\frac{\Delta x_{lg}}{h_{lg}}\right) = 29^\circ \tag{3.1.9}$$

The solution of a inclined gear leg has some disadvantages. First, the landing gear leg will result longer than the planar-type leg, thus heavier. In addition, the gear at landing will be subjected to additional loads. In fact, if the leg does not lay in a vertical plane, torques in the horizontal and vertical plane are produced in addition to the bending moment. For this reason, the leg should be sized in order to withstand larger loads, adding more weight to the structure.
In this chapter, both the possibilities have been investigated, being the analysis on the in-plane case a simplified version of the inclined-leg case.

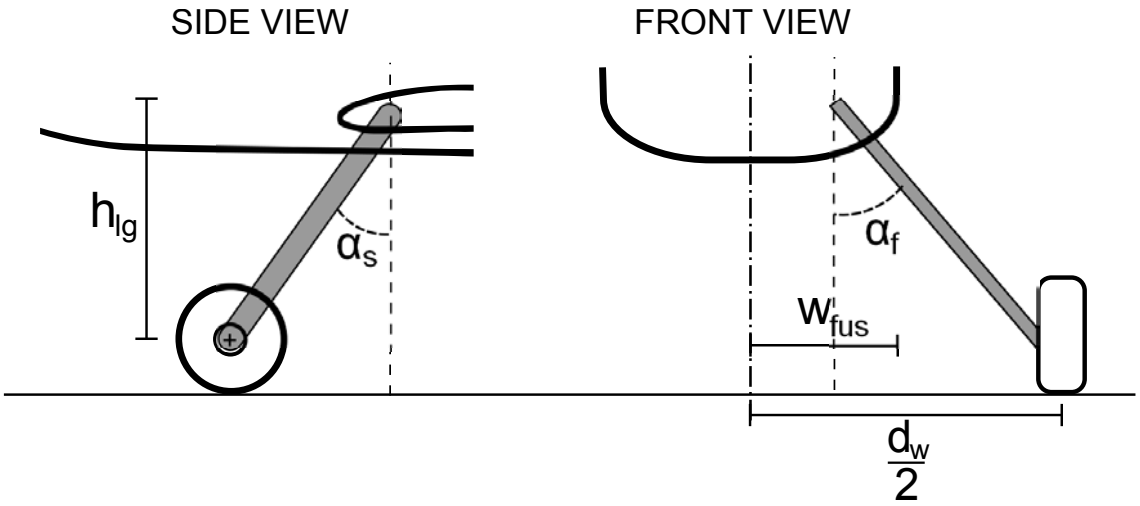

Figure 3.3: Side and front landing gear angles.

3.2 Analytical structural analysis

The landing gear leg has been modeled looking at the gears of similar aircrafts. This comparison led to choose a common bar of rectangular cross section, eventually tapered to reduce weight, with one end fixed into the fuselage and the other one connected to the wheel axle. The selected material is Aluminum 7075-T6, since it presents the highest strength values among other aluminum types. An aluminum gear leg weighs considerably less than a steel leg designed to withstand the same loads. However, Aluminum 7075-T6 is considered non-weldable by the arc-welding process, since it is very susceptible to stress corrosion cracking. For this reason a welded connection between the leg and the axle is not possible, and a different solution must be designed. In the table the Aluminum 7075-T6 properties are shown.

E [Pa]	$71.7 \cdot 10^9$
ν	0.33
Tensile Strength, Ultimate [Pa]	$572 \cdot 10^6$
Tensile Strength, Yield [Pa]	$503 \cdot 10^6$

Table 3.1: Aluminum 7075-T6 properties, obtained from Matweb [19].

3.2.1 Cantilever beam model

The simplest way to model the landing gear leg is to consider a straight cantilever beam with a load applied at the free end. The force at the free end is the perpendicular

component of the total vertical force acting on the landing gear at landing:

$$F_{\perp} = \frac{1}{2} W N_{gear} sin(\alpha_f) \approx 1549N \tag{3.2.1}$$

The length l of the beam depends on the height of the landing gear leg h_{lg} and on the angles of inclination α_f and α_s. For this model, the side angle α_s is equal to zero, considering a planar-type landing gear. The length of the equivalent cantilever beam is:

$$l = \frac{h_{lg} - 100}{cos(\alpha_f)} = 691mm \tag{3.2.2}$$

where a quantity of $100mm$ has been subtracted by h_{lg}, since that is the height of the landing gear portion into the fuselage. The required stroke S can be approximated with the vertical component of the displacement at the free end due to bending, neglecting the axial displacement. Thus,

$$\delta = \frac{S}{sin(\alpha_f)} = 113mm \tag{3.2.3}$$

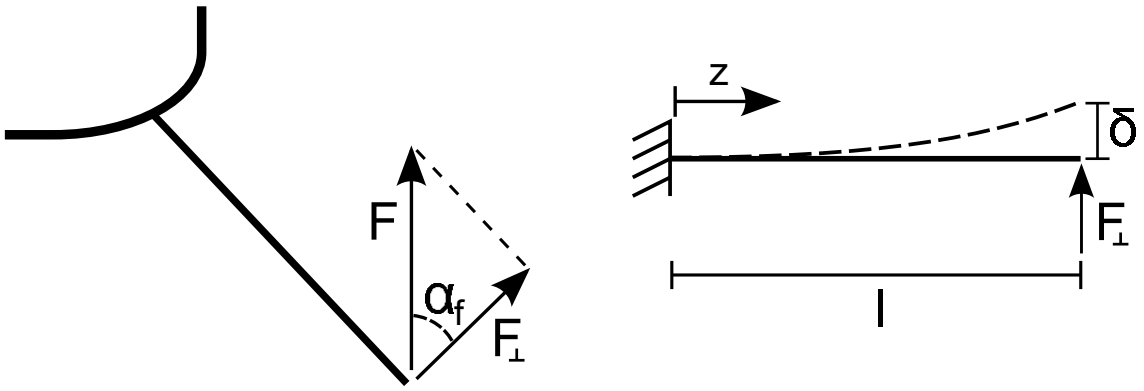

Figure 3.4: Cantilever beam model of the landing gear leg.

The two main parameters that must be controlled in the design of a solid spring landing gear are the vertical displacement at the axle end δ and the maximum stress σ_{max} that is generated at the constraint section. The vertical displacement must equal the landing gear stroke S calculated in the previous section. The maximum stress value σ_{max} must not exceed the value that grants a safety coefficient of 1.5 as prescribed by the norm. The safety coefficient is found dividing the material's yield strength by the maximum value of stress obtained from calculations:

$$n = \frac{\sigma_{yield}}{\sigma_{max}} \geq 1.5 \tag{3.2.4}$$

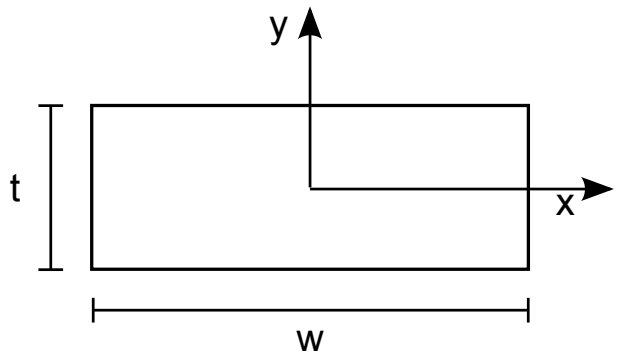

Figure 3.5: Solid rectangular cross-section.

Since the yield strength of Aluminum 7075-T6 is $\sigma_{yield} = 503MPa$, the maximum stress allowable on the leg is

$$\sigma_{max_{limit}} = \frac{\sigma_{yield}}{1.5} = 335MPa \tag{3.2.5}$$

In addition, the stress value must be small enough to allow an adequately long fatigue life of the component. In this chapter, a method for estimating the fatigue life of the landing gear leg will be presented in detail.
The obvious constraint for sizing the landing gear leg is mass. The leg must designed to be as light as possible, thus producing the same stroke and the same maximum stress value at landing.
Considering a constant cross-section beam, the displacement value at the free end is found with the following expression ([21], paragraph 13.1):

$$\delta = \frac{F_{\perp} l^3}{3EI_x} \tag{3.2.6}$$

where $F_{\perp}$ is the concentrated load at the free end, l is the beam length and I_x is the second moment of area of the section calculated by the axis laying in the cross-section plane and perpendicular to the applied force. The bending moment only has been considered, since the shear moment can be neglected for slender beams ([21], paragraph 13.6). For a rectangular cross section of width w and thickness t, the second moment of area is calculated as

$$I_x = \frac{wt^3}{12} \tag{3.2.7}$$

The stress distribution at a certain cross-section along the beam is given by ([21], paragraph 9.1):

$$\sigma(y) = \frac{M(z)}{I_x} y \tag{3.2.8}$$

where y is the vertical distance from the x axis, and $M(z)$ is the bending moment at the cross section which is located at a distance z from the fixed constraint, given by

$M(z) = -F_\perp(l - z)$. The maximum stress occurs at the constrained section (z=0), where $M(z) = -F_\perp l$ is maximum, and when y equals half of the thickness t of the section. For calculating the stress, the modulus of M is considered.
Substituting the value of I_x in the expressions $(3.2.6)$ and $(3.2.8)$ gives:

$$\delta = \frac{4F_\perp l^3}{Ewt^3} \tag{3.2.9}$$

$$\sigma_{max} = \frac{12F_\perp l}{wt^3}\frac{t}{2} = \frac{6F_\perp l}{wt^2} \tag{3.2.10}$$

Dividing the two expressions above gives:

$$\frac{\delta}{\sigma_{max}} = \frac{4F_\perp l^3}{Ewt^3}\frac{wt^2}{6F_\perp l} = \frac{2l^2}{3Et} \tag{3.2.11}$$

It is evident that, in order to obtain a larger displacement keeping the stress to a fixed value, it is more efficient to add length to the gear leg than to decrease its thickness. However, this option adds mass to the beam. In fact, the mass of the beam is given by:

$$m = \rho twl \tag{3.2.12}$$

where ρ is the density of the material. An interesting relation can be found rearranging the $(3.2.12)$, substituting the value of t extracted from $(3.2.11)$ and the value of w extracted from the $(3.2.10)$:

$$m = \rho\frac{2l^2\sigma_{max}}{3E\delta}\frac{6F_\perp l}{\sigma_{max}t^2}l = 9\rho F_\perp E\left(\frac{\delta}{\sigma_{max}^2}\right) \tag{3.2.13}$$

From this equation it is clear that, for a specific material and for a specific load condition, mass depends only on the ratio δ/σ_{max}^2. Of these two parameters, δ is a requirement and σ_{max} must not exceed the value calculated with the relation $(3.2.5)$. Thus, there is a minimum mass value for a landing gear leg of this kind, whatever is the value of w, t or l. Substituting the values obtained for δ, $\sigma_{max_{limit}}$, $F_\perp$ and the Aluminum 7075-T6 properties ρ and E gives a minimum mas value of:

$$m_{min} = 2.8kg$$

This value is rather high, considering that the maximum stress value has been used in the equation. Since a safe fatigue life requires lower values of maximum stress, the leg mass must be further increased. A way to reduce its mass must be found, and the most immediate solution is to taper the width.

3.2.2 Simple tapered beam

A tapered beam has the advantage of obtaining a larger displacement keeping a large cross-section at the constraint, thus keeping a low maximum stress value. However, if the shape is not accurately chosen, the maximum stress may not occur at the constrained end, but it may move in a certain section of the beam where the cross-section is "weaker" due to the taper.
In the following calculations, only the width variation along the beam is considered. The width $w(z)$ linearly decreases from the fixed constraint toward the free end. The width maximum value is called w_1, and its minimum value is w_2. The minimum value must be large enough to allow the mounting of a bolted flange joint to the wheel axle, thus a value of $w_2 = 50mm$ is chosen.
The analytical formulation of a tapered beam is more complex than the constant cross-section beam. Actually, is not possible to obtain an explicit expression for the displacement, because this would require integrating a complex expression. However, calculations can be made numerically. For this calculation, a MATLAB® script has been wrote, and the whole code is found in the appendix.
The strain energy method has been chosen in order to calculate the maximum displacement, which is expected to be at the free end of the beam. Only the strain energy due to bending is considered, neglecting the contribute of the shear effect. The strain energy per unit length due to bending is given by the following expression ([21], paragraph 9.4):

$$u_{bending} = \frac{M(z)^2}{2EI_x(z)} \tag{3.2.14}$$

where $M(z)$ and I_x are respectively the bending moment and the second moment of area as a function of beam length. The bending moment, as before, varies with the distance from the fixed constraint (where $z = 0$ is assumed), and is given by

$$M = -F_{\perp}(l - z)$$

For a straight beam with constant cross-section, the moment I_x is constant through the beam's length; however, since the beam is tapered it varies proportionally with the beam width at the z section:

$$I_x(z) = \frac{w(z)t^3}{12}$$

where $w(z)$ is the section width at the z section

$$w(z) = w_1 + \frac{w_2 - w_1}{l}z \tag{3.2.15}$$

Substituting the expression for I_x in the $(3.2.14)$ gives:

$$u_{bending} = \frac{M(z)^2}{2EI_x(z)} = \frac{6F_{\perp}^2(l - z)^2}{Et^3(w_1 - \frac{w_1 - w_2}{l}z)}$$

The function above is integrated over the beam length to obtain the total shear energy due to bending:

$$U_{bending} = \int_0^l u_{bending}\,\mathrm{d}z$$

The integral is not explicited because of the complicated expression that would result. For Castigliano's theorem ([21], paragraph 15.3), the displacement at the point where the force $F_\perp$ is acting is given by simply differentiating the total complementary energy by the force $F_\perp$. For a linear load-deflection relation, the complementary energy equals the strain energy. Thus,

$$\delta_{(x=l)} = \frac{\delta U_{bending}}{\delta F_\perp}$$

The maximum section stress as a function of the length z is now given by:

$$\sigma_{max}(z) = \frac{M(z)}{I_x(z)}\frac{t}{2} = \frac{6F(l-z)}{w(z)t^2} \tag{3.2.16}$$

Assuming that maximum stress occurs at the constrained section, it can be found with the following expression:

$$\sigma_{max(z=0)} = \frac{6Fl}{w_1 t^2} \tag{3.2.17}$$

The total mass of the beam is:

$$m = \rho\frac{w_1 + w_2}{2}tl \tag{3.2.18}$$

Thus, the best way to reduce the maximum stress with the minimum mass increase is to increase w_1, keeping the free end width w_2 at the minimum value. From the numerical calculation it appears that, while w_1 is increased, the thickness t must be gradually decreased to obtain the desired displacement δ. Starting from a ratio of $w_1/w_2 = 1$, a thickness $t = 20mm$ and keeping the length $l = 691mm$, several iteration have been carried out to size a gear leg that matches the requirement of stroke $S = \delta sin(\alpha_f)$ keeping an acceptable value of maximum stress. In the table 3.2 are shown the results of different iterations. The value of the mass includes the mass of a solid cylindrical aluminum axle which has a diameter of $\emptyset_{ax} = 1in$ $(25mm)$ and a length of $l_{ax} = 90mm$. The axle mass is then:

$$m_{ax} = \pi\left(\frac{\emptyset_{ax}}{2}\right)^2 l_{ax} = 0.127kg \tag{3.2.19}$$

The results in the table show that the required stroke of $S = 65mm$ is reached with an acceptable value of $\sigma_{max} = 297MPa$ for a width $w_1 = 130mm$ and a constant thickness of $13mm$. A smaller stress value of $\sigma_{max} = 262MPa$ can be obtained with a width $w_1 = 170mm$ and a constant thickness of $12mm$, thus increasing the mass from $2.37kg$ to $2.62kg$. These values will be the starting point for an optimization done with a finite element analysis.

$w_1[mm]$	$w_2[mm]$	$t[mm]$	$l[mm]$	$\delta[mm]$	$S[mm]$	$\sigma_{max}[MPa]$	$m[kg]$
50	50	20	691	70	40	321	2.05
70	50	20	691	54	31	229	2.43
70	50	18	691	74	42	283	2.20
100	50	18	691	55	32	198	2.72
100	50	15	691	96	55	285	2.29
130	50	13	691	118	68	292	2.37
170	50	12	691	120	69	262	2.62

Table 3.2

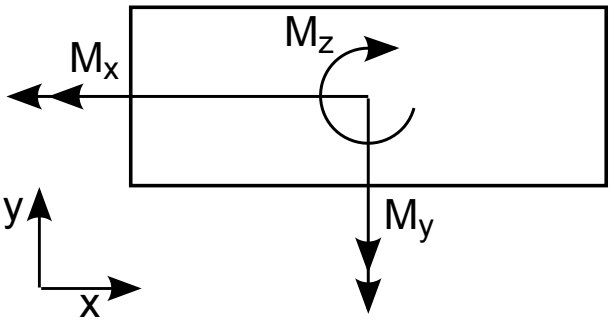

Figure 3.6: Rectangular cross-section with moments due to mis-aligning of the force $F_\perp$.

3.2.3 Inclined gear leg

The case of a gear leg that is directly connected to the spar box is now considered. The side angle will now have a value of $\alpha_s = 29°$ as found in the $(3.1.9)$. Since the vertical force F does not lay in the same vertical plane of the constrained section, the force $F_\perp$ is not aligned with the y axis of the rectangular cross-section. Two additional moments will then occur along the leg: a bending moment M_y and a torque M_z (figure 3.6).
The length of the gear leg is now given by:

$$l = \frac{h_{lg} - 100}{cos(\alpha_f)cos(\alpha_s)} = 790mm \tag{3.2.20}$$

The leg results approximately $100mm$ longer. Thus, a larger stroke δ is expected, but also a larger mass. The bending moment distribution M_x is given by the product of the perpendicular component of the force F and its arm relative to the considered cross-section:

$$M_x = -Fsin(\alpha_f)(l - z)cos(\alpha_s) \tag{3.2.21}$$

Similarly, the bending moment M_y is given by the product of the in-plane component of the force F and its arm, which in the previous case was equal to zero. The expression

is:

$$M_y = -Fcos(\alpha_f)(l-z)sin(\alpha_s) \tag{3.2.22}$$

The torque M_z is given by the product of the perpendicular component and the same arm that produced M_y:

$$M_z = -Fsin(\alpha_f)(l-z)sin(\alpha_s) \tag{3.2.23}$$

Obviously, the maximum value for these functions occurs at the constrained section, where $z = 0$.
The displacement at the free end δ is not calculated in this case, due to the complicated analytical formulation. Only a brief stress estimate will be presented.
To calculate the stress distribution due to the two bending moments, the following expression is used ([21], paragraph 9.7):

$$\sigma_z(x,y) = \frac{M_x}{I_x}y + \frac{M_y}{I_y}x \tag{3.2.24}$$

Substituting the values of M_x, M_y and the moments of inertia the above expression becomes:

$$\begin{aligned}\sigma_z(x,y) &= \frac{Flsin(\alpha_f)cos(\alpha_s)}{\frac{wt^3}{12}}y + \frac{Flcos(\alpha_f)sin(\alpha_s)}{\frac{w^3t}{12}}x \\ &= \frac{12Fl}{wt}\left(\frac{sin(\alpha_f)cos(\alpha_s)}{t^2}y + \frac{cos(\alpha_f)sin(\alpha_s)}{w^2}x\right)\end{aligned} \tag{3.2.25}$$

The maximum values for $\sigma_z(x,y)$ occurs where both x and y are maximum, at the corners of the cross-section.
The torque M_z produces a shear stress on the cross-section. The analytical formulation for stresses due to shear is complex, and semi-empirical relations may be found for simple cross-section types. For a rectangular cross-section, the shear stress distribution is given by ([18], paragraph 11.5.1.7):

$$\tau_{xy,max} = \frac{M_z}{I_t}t \tag{3.2.26}$$

where I_t is the torque modulus of the section. For a rectangular cross section where $w/t > 3$, the modulus I_t is given by the following analytical relation:

$$I_t = \frac{wt^3}{3}\left(1 - 0.63\frac{t}{w}\right) \tag{3.2.27}$$

The maximum shear stress will then occur where the border of the cross-section is closest to the section centroid.
Since both direct and shear stress are present at the cross-section in this case, the Von Mises criterion may be used to combine them, obtaining an equivalent stress σ_{eq}. The

equivalent stress value is then compared with the yield stress to obtain the safety factor n, and used for fatigue life calculation. The Von Mises equivalent stress expression for a two-dimensional problem is given by ([21], paragraph 14.10):

$$\sigma_{eq} = \sqrt{\sigma_z^2 + 3\tau_{xy}} \tag{3.2.28}$$

With the dimensions obtained from the leg sized in the previous case (table 3.2, sixth row), the geometry has been modified in order to decrease the equivalent stress. In fact, since the leg is longer, moments are larger, thus a larger displacement is obtained with a larger stress at the constrained section. Two geometries have been calculated, one with a larger width and another one with a larger thickness. In both cases, the mass of the leg is larger. The displacement will be calculated with the finite elements method, then the leg will be sized to met the required stroke.

$w_1[mm]$	$w_2[mm]$	$t[mm]$	$\sigma_{z,max}[MPa]$	$\tau_{xy,max}[MPa]$	$\sigma_{eq}[MPa]$	$m[kg]$
130	50	13	315	86	349	2.70
130	50	14	273	75	303	2.89
150	50	13	271	74	300	2.98

Table 3.3

3.3 Finite Element Analysis

In this section, the results obtained from analytical calculations have been confirmed and optimized with a finite element analysis done with the ANSYS® APDL interface.

3.3.1 Tapered cantilever beam

The landing gear has been modeled using BEAM 188 elements, which specifications have been presented in section 2.4.1. The material properties have been taken from table 3.1. The selected cross-section is a solid rectangular cross-section. To taper the cross-section, the two end sections must be specified, and then a new section with the option "taper" must be created. The taper section requires in input the numbers that represent the end sections and the (x,y,z) location of the ends at which the cross-sections correspond:

```
ET,1,BEAM188
KEYOPT,1,3,2
SECTYPE,1,BEAM,RECT,,0 !--Large section
SECOFFSET,CENT
```

```
SECDATA,t1,w1,0,0,0,0,0,0,0,0,0,0 !--Base,Height
SECTYPE,2,BEAM,RECT,,0 !--Small section
SECOFFSET,CENT
SECDATA,t2,w2,0,0,0,0,0,0,0,0,0,0 !--Base,Height
SECTYPE,3,TAPER,,taper !--Taper section
SECDATA,1,0,0,0
SECDATA,2,l*cos(alpha)*sin(beta),-l*cos(alpha)*cos(beta),l*sin(alpha)
```

A very simple model has been set to confirm the results obtained for the cantilever beam at paragraph 3.2.2. The geometry considered is the one shown at the sixth row of table 3.2: the large width is $w_1 = 130mm$ and thickness is $t = 13mm$. Two *keypoints* have been inputed, and the line connecting them has been divided in 20 elements, which is a sufficient number to obtain an accurate result for a cantilever beam. The vertical load $F = 2700N$ has been set at free end, and at the constrained end all the displacements have been blocked (fixed constraint). A simple static analysis gives results which are very close to the ones found in the table 3.2.

The finite element software allows to easily calculate variations in the cross-sections that would require a very complicated analytical calculus. For this reason, a stress and mass optimization has been carried out considering a tapered thickness in addition to the tapered width. Tapering the thickness allows to obtain a more flexible landing gear leg, thus keeping a thick cross-section where the maximum stress is expected. However, with a tapered thickness the maximum stress does not occur at the constrained end section. The maximum stress value will occur somewhere along the leg where the cross-section is weaker. It may be very complicated to estimate the exact location where the maximum stress occurs, thus the beam sizing has been carried out with several iterations. The simple way in which the model has been created allows the software to make the calculation in a few seconds, thus allowing an iterative approach. Starting from the defined dimensions of the simple width-tapered beam, a the design has been optimized setting a thickness $t_1 = 15mm$ at the constrained end and a thickness $t_2 = 10mm$ at the free end. The results are shown in figure 3.9. A maximum stress of $235MPa$ has been obtained, thus obtaining the 20% less stress, with a similar mass of $2.35kg$.

3.3.2 Inclined gear leg

A finite element model has been created for the inclined gear leg case. Actually, the input file is the same of the previous case, but now setting an angle $\alpha_s = 29°$ instead of a null angle. The boundary conditions are the same of the previous model. The dimensions at the first row of table 3.3 have been inputed for an initial displacement estimate. The resulting stress is shown in figure 3.10, and confirms the analytical calculations.

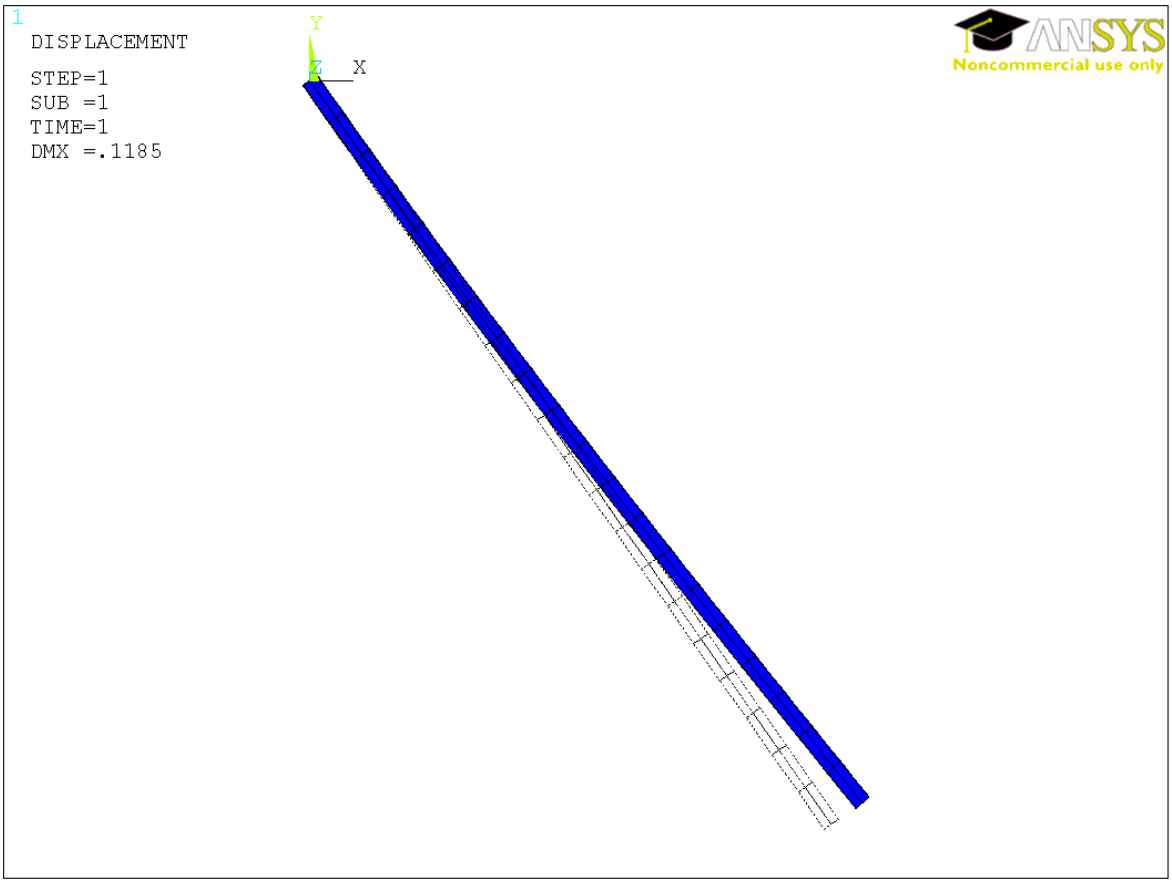

Figure 3.7: Deformed shape and undeformed edges of the tapered beam. The maximum value of the displacement is shown with the abbreviation DMX.

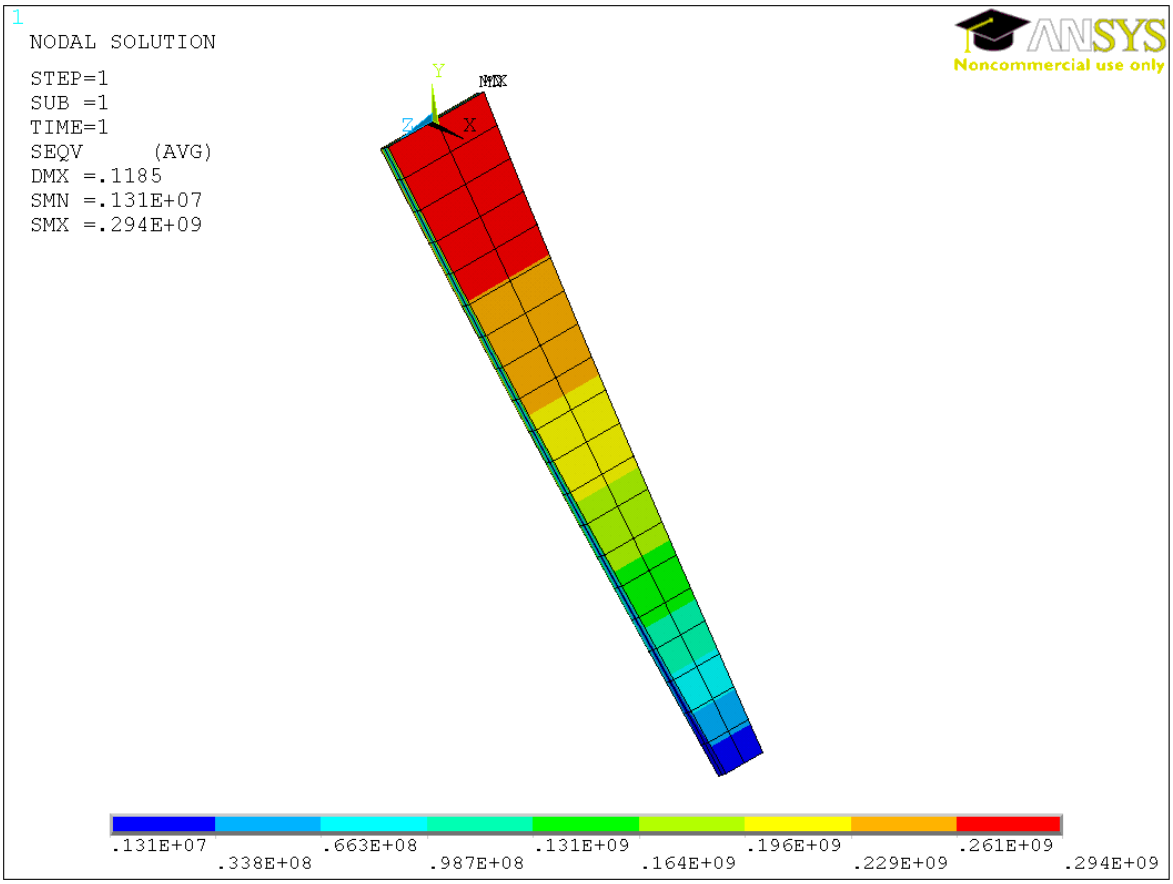

Figure 3.8: Stress distribution on the beam. Maximum width is $w_1 = 130mm$, and thickness has a constant value of $t_1 = 13mm$. Maximum stress occurs at the constrained section.

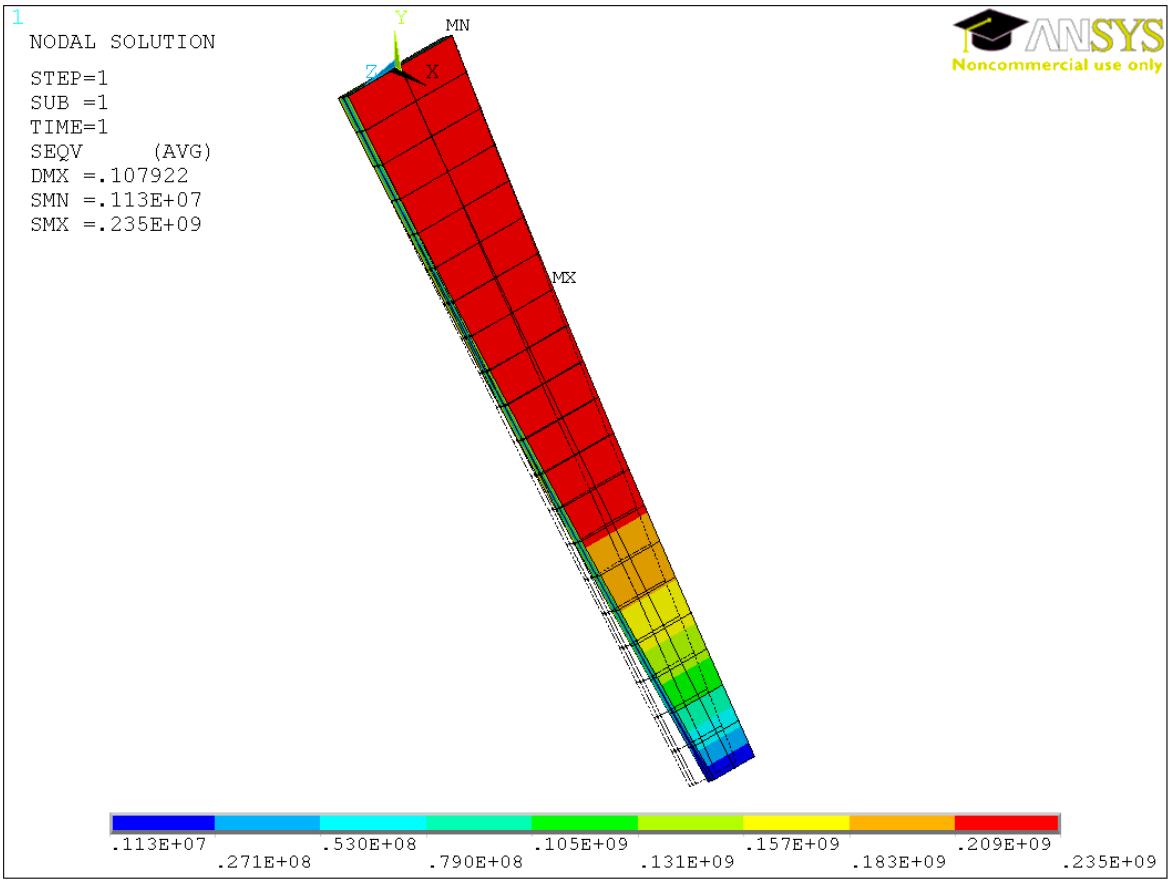

Figure 3.9: Stress distribution on the beam. Maximum width is $w_1 = 130mm$, and thickness is tapered from $t_1 = 15mm$ to $t_2 = 10mm$. Maximum stress occurs approximately at $7/20$ of the leg length, starting from the constrained section.

The nodal solution gives the vertical displacement at the free end, which in this case is $S = 102mm$. Both displacement and stress are very high, thus the leg is sized with the inverse procedure with respect to the previous case. The ratio w_1/t is reduced in order to obtain a stiffer leg, saving as much mass as possible. A good result has been obtained with a leg of width $w_1 = 100mm$, and tapered thickness from $t_1 = 18mm$ to $t_2 = 13mm$. The result is shown in figure 3.11. The required stroke is obtained with a maximum stress of $256MPa$ and a total mass of $2.73kg$.

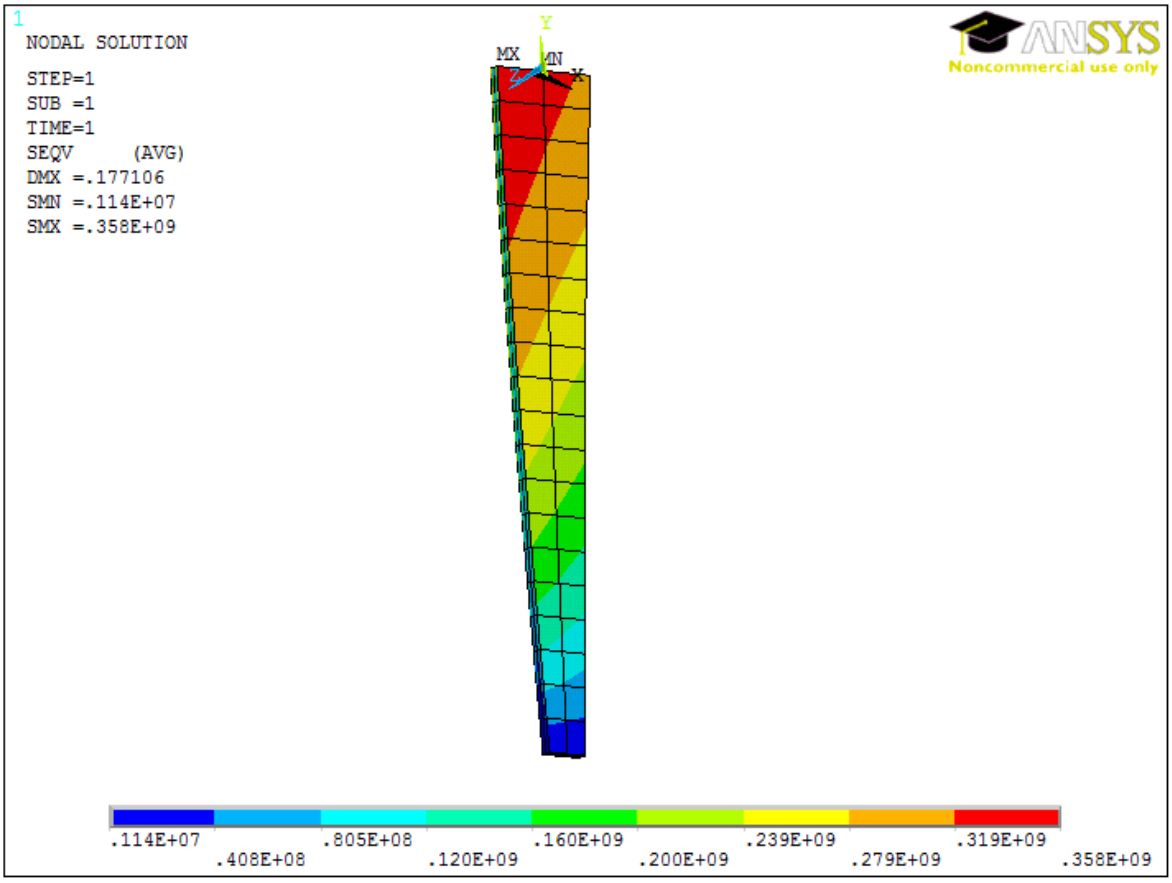

Figure 3.10: Stress distribution on the beam, inclined leg case. Maximum width is $w_1 = 130mm$, and thickness has a constant value of $t_1 = 13mm$. The stress distribution is not perpendicular to the beam's length any more.

3.3.3 Optimized model

A better model for the landing gear leg can be obtained using shell elements. Their use is particularly suitable since the leg section has a large width if compared to the thickness.

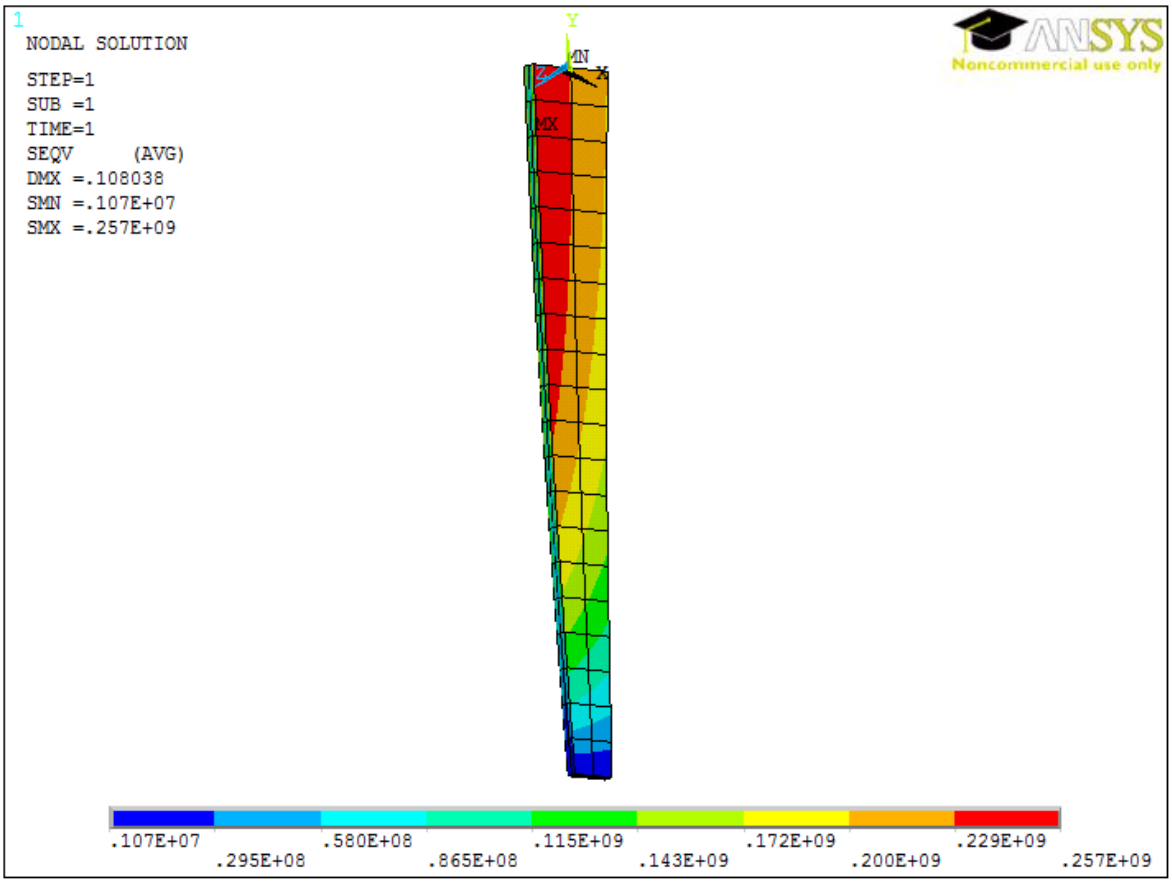

Figure 3.11: Stress distribution on the beam, optimized inclined leg case. Maximum width is $w_1 = 100mm$, and thickness is tapered from $t_1 = 18mm$ to $t_2 = 13mm$.

Again, elements SHELL 181 have been used. The APDL interface allows to define a tapered thickness for shell elements. The thickness as a function of the coordinate x has been inputed in a *table*, which must be associated with the shell section with the following commands:

```
*DIM,TAPERED,TABLE,2,,,x
TAPERED(1,0)=0,l*cos(alpha)*sin(beta)
TAPERED(1,1)=t1,t2
SECFUNCTION,%tapered%
```

Modeling the leg with shell elements allows to model the final part of the leg, where the axle is connected with a bolted flange. The bolted connections, that will be four at the angles of the rectangular flange, have not been modeled. The axle is modeled with beam elements, directly connected to the leg surface mesh. The load has been applied at halfway along the axle, to obtain a more realistic behavior. The constraint has been applied to all the nodes associated to the line defining the wide section.
The shell model allows to "see" concentrations of stress that the beam model cannot show, due to its coarse mesh. The two previously optimized gear legs have been modeled with shell elements. In both in-plane and inclined gear leg the maximum stress values shown in the results increases. For the in-plane leg, the maximum stress value calculated is now $286MPa$, and occurs approximately the half length of the leg (figure 3.12). For the inclined leg, a very high value of $455MPa$ is obtained at the front corners of the constrained section (figure 3.13). For this reason, the inclined gear leg option is definitely discarded, since it would require to much mass to withstand these stress values with a good margin of safety. To get a more realistic model, it is necessary to compare the required deflection of the beam to its dimensions. If the required maximum displacement for the in-plane gear leg case is about $120mm$, the ratio between this displacement and the total length of the leg is:

$$\frac{120}{691} = 17\%$$

It is evident that the hypothesis of small displacement is not valid for this problem. For this reason, the real behavior of the structure may change dramatically, widely increasing both stress and displacement if compared to the theory models. A way to predict the behavior of the structure in the condition of large displacements is to carry out a non-linear analysis. In this type of analysis, the software applies the load incrementally, and at each load step the stiffness matrix is recalculated considering the deflected geometry. For this reason, the solver takes more time to obtain the solution. A number of 10 steps has been set, so that at each step the force is incremented by $F/10$. The results are shown in figure 3.14. With the shell model, stroke is calculated at the node which lays at the intersection between the leg and the axle. As expected, the maximum displacement is very high, almost the double of the requested stroke (S=128mm), and thus the maximum

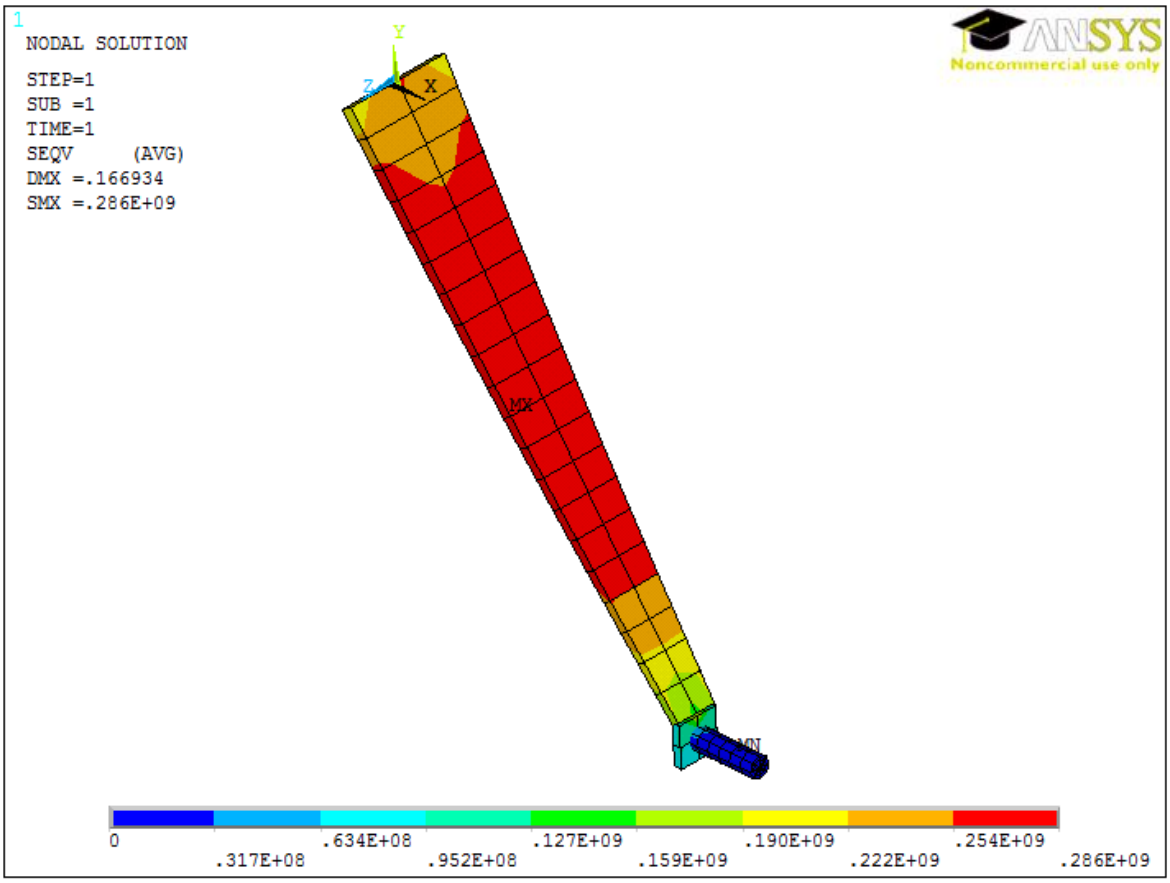

Figure 3.12: Stress distribution on the beam, in-plane leg modeled with shell elements. Maximum width is $w_1 = 130mm$, and thickness is tapered from $t_1 = 15mm$ to $t_2 = 10mm$.

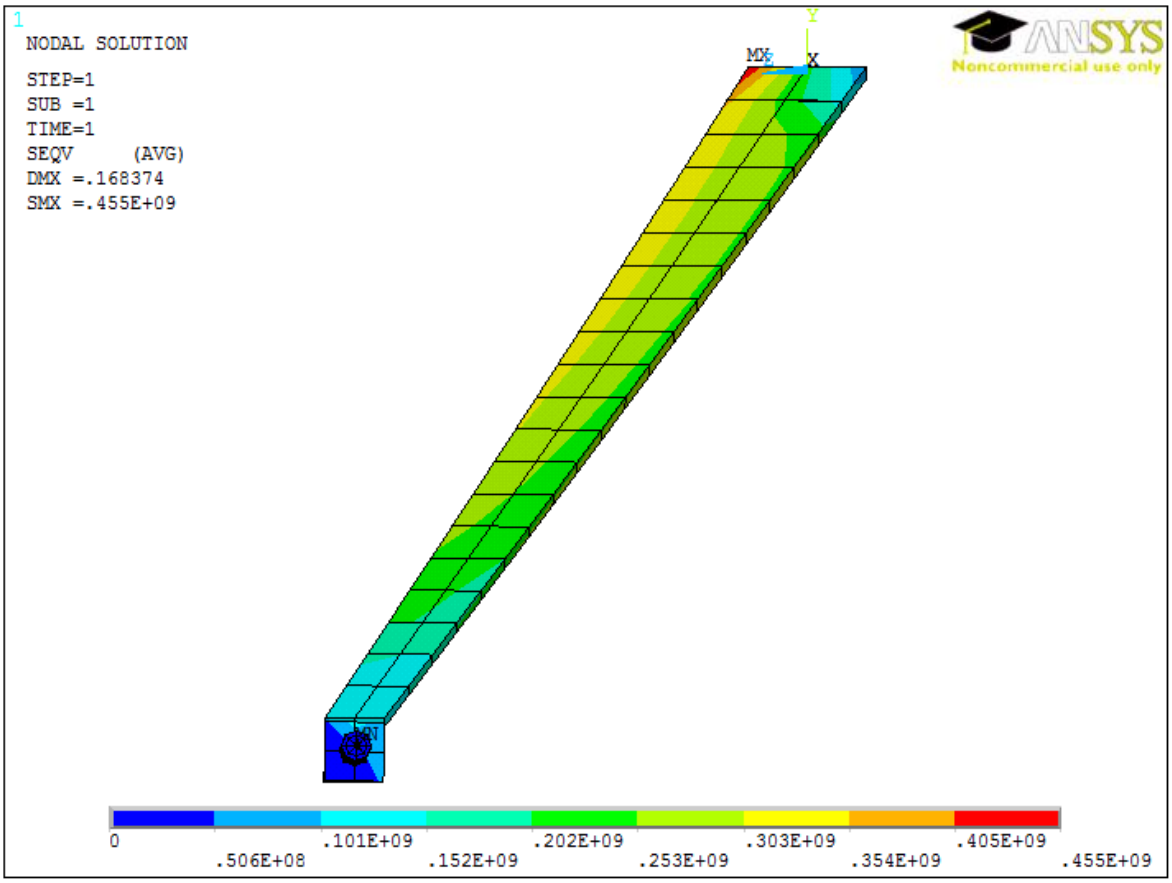

Figure 3.13: Stress distribution on the beam, inclined leg modeled with shell elements. Maximum width is $w_1 = 100mm$, and thickness is tapered from $t_1 = 18mm$ to $t_2 = 13mm$.

stress of $413MPa$ is over the safety value. This means that the gear leg sized in this way is much more flexible than necessary. Thus, the leg must be re-sized to reach the minimum required stroke and lower the stress.
As done previously in the inclined leg case, the ratio $w_1/w2$ has been decreased and at the same time both thicknesses t_1 and t_2 have been increased. The optimal result is found for a width of $w_1 = 110mm$, and a tapered thickness from $t_1 = 18mm$ to $t_2 = 13mm$. The vertical stroke is $S = 65mm$ as required, and the consequent maximum stress is $264MPa$, which gives a safety factor of:

$$n = \frac{503}{264} = 1.9$$

3.3.4 Axle inclination

From the results, the nodal rotations component can be seen. In particular, is interesting to know the rotation at the free end, since that will be the rotation of the wheel axle. While taxing, the wheel must be perpendicular to the ground, thus the axle must have a certain downward inclination when unloaded. To obtain the required rotation, only the a fraction of the weight of the aircraft has been applied to the model. Considering that the main gear carries the 90% of the load, the applied vertical force F is simply obtained with:

$$F = \frac{1}{2} \cdot 0.9W = 0.45W = 795N \tag{3.3.1}$$

As before, a non-linear analysis has been done. The resulting vertical displacement is $15mm$ and the maximum stress is $66MPa$. The rotation at the node at the beginning of the axle is $0.074rad$. This means that the axle must be inclined downward with an inclination of approximately $\gamma = 4°$. The leg has then been re-designed, inclining the end flange and thus the axle. The same analysis has been done, resulting that the axle position is perfectly horizontal (figure 3.16).

$w_1[mm]$	$w_2[mm]$	$t_1[mm]$	$t_2[mm]$	$S[mm]$	$\sigma_{max}[MPa]$	$mass[kg]$
110	50	13	18	65	264	2.6

Table 3.4: Resume of the dimensions of the optimized landing gear leg.

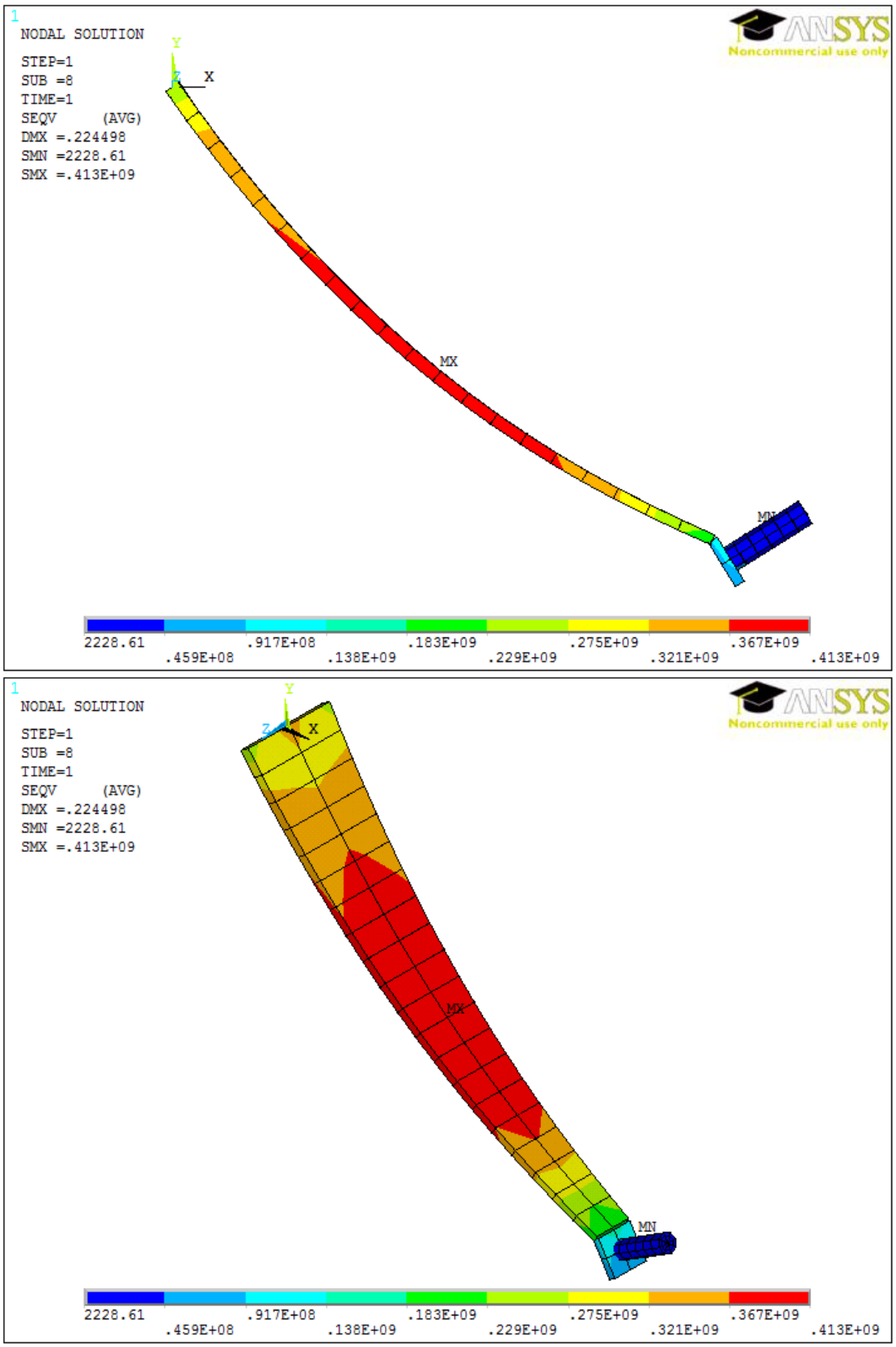

Figure 3.14: Stress distribution, non-linear analysis of the in-plane gear leg. Maximum width is $w_1 = 130mm$, and thickness is tapered from $t_1 = 15mm$ to $t_2 = 10mm$.

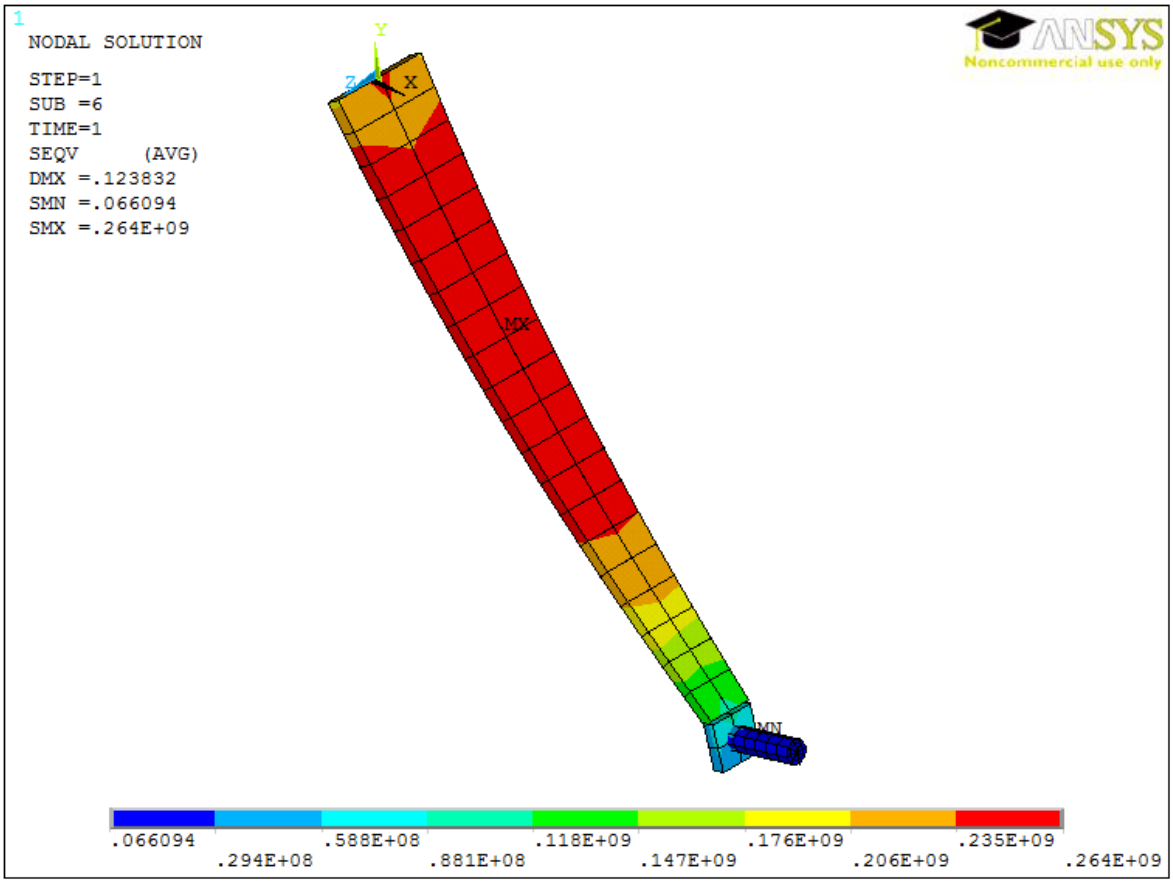

Figure 3.15: Stress distribution, non-linear analysis of the in-plane gear leg. Maximum width is $w_1 = 110mm$, and thickness is tapered from $t_1 = 18mm$ to $t_2 = 13mm$.

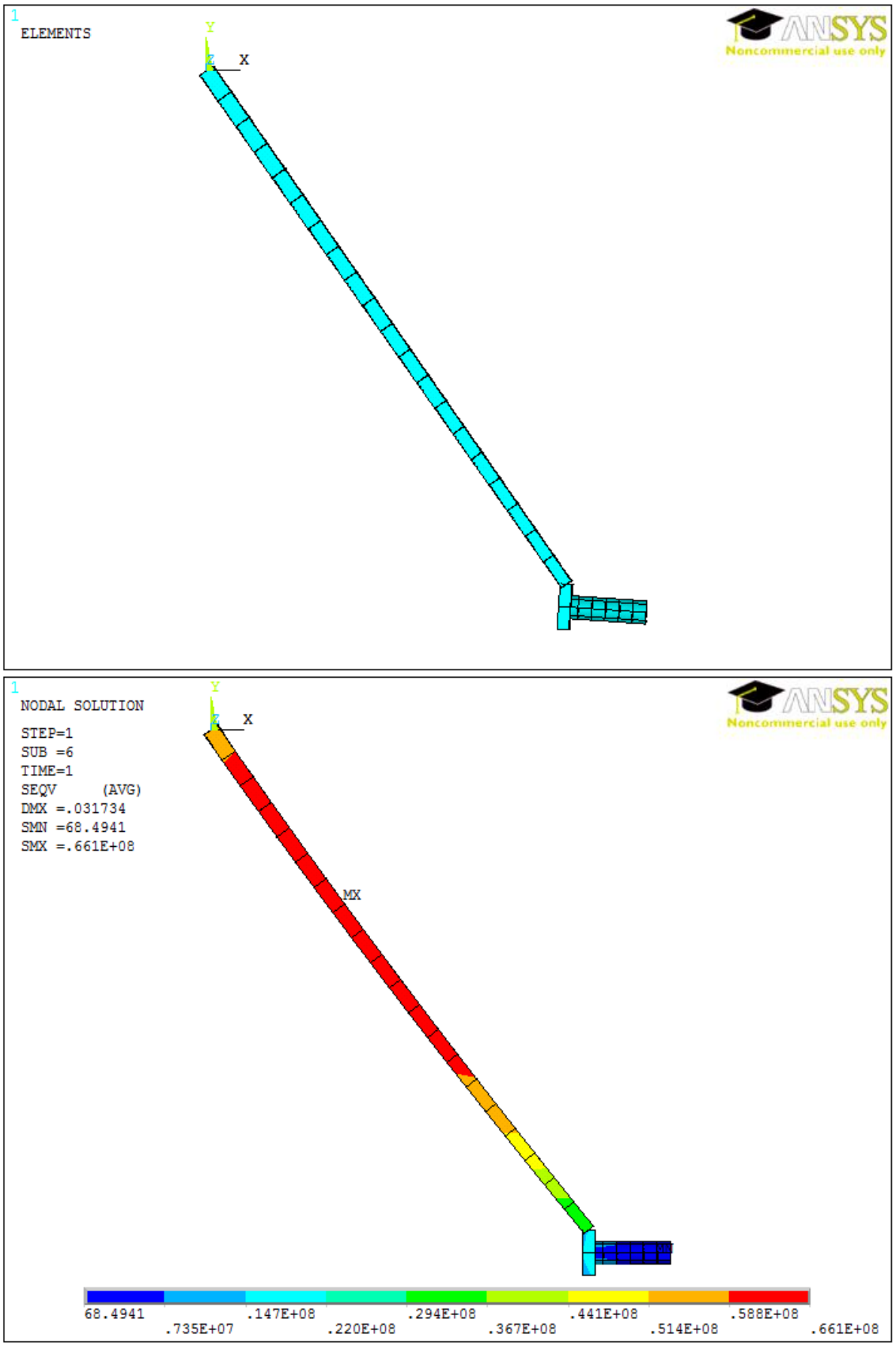

Figure 3.16: Stress distribution, non-linear analysis of the in-plane gear leg during taxiing. Maximum width is $w_1 = 110mm$, and thickness is tapered from $t_1 = 18mm$ to $t_2 = 13mm$. The initial inclination of the flange allows the axle to be parallel to the ground when loaded with the simple weight of the aircraft.

3.4 Fatigue life estimate

A landing gear leg is a component which is highly exposed to fatigue, due to the nature of the loads acting on it. The leg must then be designed taking in account the possible failure due to fatigue, in addition to the static loading that has been verified previously in the chapter. In this section, a method taken from Atzori [6] has been used to estimate the fatigue life of the landing gear leg sized as in table 3.4. The method allows to calculate with a good safety margin the fatigue life of the component without statistical data based on experiments.
The fatigue life is calculated considering two parameters that define this case, the stress amplitude σ_a and the stress ratio R. The stress amplitude is defined as:

$$\sigma_a = \sigma_{max} - \sigma_m \tag{3.4.1}$$

where σ_m is the mean stress value, simply calculated as:

$$\sigma_m = \frac{\sigma_{max} + \sigma_{min}}{2} \tag{3.4.2}$$

In this case, the minimum value of sigma occurs when the gear leg is loaded inversely with respect to the landing case. The only case when this happens is during flight, when the leg deflects downward due to its own weight. However, the stress value in this case is expected to be so small that it may be considered equal to zero. Thus, since $\sigma_{min} = 0$, the expressions $(3.4.1)$ and $(3.4.2)$ give

$$\sigma_m = \sigma_a = \frac{\sigma_{max}}{2} \tag{3.4.3}$$

The stress ratio R is defined as the ratio between σ_{min} and σ_{max}, so in this case its value is $R = 0$.
The first step is to draw the Haigh diagram assuming that the material reaches the fatigue limit at $N = 2 \cdot 10^6$ cycles. The Haigh diagram reports the value of σ_a as a function of the mean stress σ_a for a certain number of cycles. Considering the standard conditions of $R = -1$ ($\sigma_m = 0$) and a survive probability of 50%, the material has an "infinite" fatigue life if the stress amplitude is less than

$$\sigma_{a\infty} = (0.35 \div 0.6)\sigma_R \tag{3.4.4}$$

where $\sigma_u l$ is the ultimate tensile strength. Considering the ultimate strength of Aluminum 7075-T6 which is $\sigma_R = 570MPa$ and assuming for safety that $\sigma_{a\infty} = 0.35\sigma_R$, the following infinite-life stress amplitude is obtained:

$$\sigma_{a\infty} = 0.35 \cdot 570 = 199.5MPa \tag{3.4.5}$$

The curve a in figure 3.17 can now be drawn. This curve shows that the higher the mean stress is, the lower the amplitude below which the fatigue life is infinite. However, this curve must be modified due to internal factors that describe the considered mechanical component. In fact, the curve a is related to a generic specimen of $10mm$ diameter. An effective infinite-life stress amplitude must be calculated considering the surface finishing, component dimensions and possible notch effects. In this case, a good surface finishing is considered, and no notches are present in the design. Thus, the $\sigma_{a\infty}$ must be divided only by a factor K_d representing the effects of size on the fatigue life. In fact, the larger the component is, the more are the probabilities to find defects in the material that may be the cause of fatigue cracking. According to the literature [6], to the leg effective dimensions correspond a factor $K_d = 1.3$. In addition to internal effects, external effects may be considered. The only effect that is worth considering is the way the load is applied. In fact, the curve a is related to a rotating bending test, while the leg is subjected to simple bending. For this reason, $\sigma_{a\infty}$ must be divided by a value of $K_v = 0.8$. The effective infinite-life stress amplitude is then calculated as follows:

$$\sigma_{a\infty_{eff}} = \frac{\sigma_{a\infty}}{1.3 \cdot 0.8} = 191.8MPa \tag{3.4.6}$$

With this value, the correct curve b can be drawn in the haigh diagram. This curve is defined by the equation

$$y = -\frac{\sigma_{a\infty_{eff}}}{\sigma_R}x + \sigma_{a\infty_{eff}} = -0.336x + 191.8 \tag{3.4.7}$$

This curve is used to find the value of the effective infinite-life stress amplitude for the stress ratio $R = 0$. In the Haigh diagram, the condition $R = 0$ is represented by the curve $y = x$. The desired stress amplitude $\sigma_{a\infty(R=0)}$ is found at the intersection between these two curves. Thus, substituting x with y in the expression $(3.4.7)$ gives

$$\sigma_{a\infty(R=0)} = \frac{191.8}{1 + 0.336} = 143.6MPa \tag{3.4.8}$$

This value allows to define a first point of coordinates $(2 \cdot 10^6, 143.6)$ on the Woehler curve. The Woehler represents the relation between the stress amplitude and the number of cycles that define the fatigue life of the component. The curve is reported in a logarithmic diagram, so that the relation appears to be linear. Thus, it is sufficient to obtain only a second point to define the linear relation that allows to calculate the effective fatigue life of the component.

The second point is found for a low number of cycles $N = 10^3$, at which is expected that the failure happens for a value of stress amplitude σ_{a_R} which for $R = 0$ is defined as half the value of the ultimate strength of the material:

$$\sigma_{aR} = \frac{1}{2}\sigma_R = 285MPa \tag{3.4.9}$$

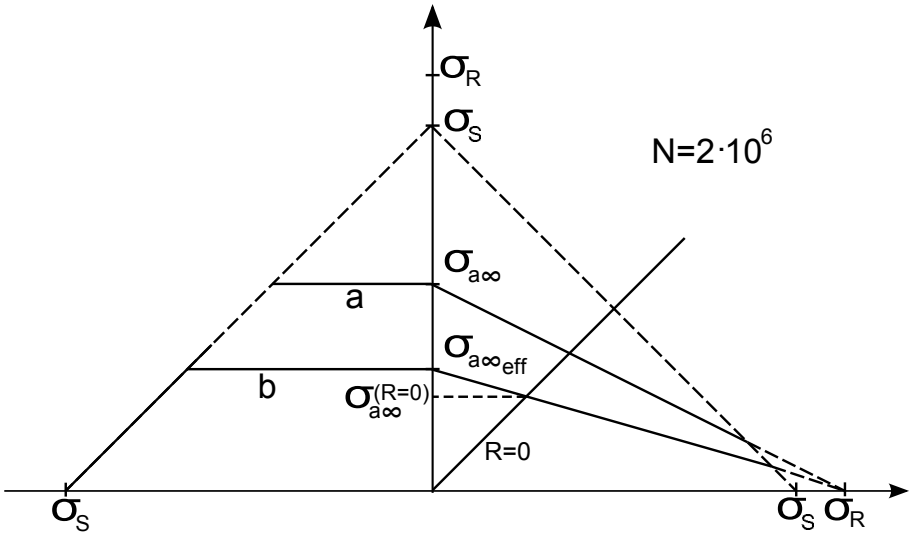

Figure 3.17: Haigh diagram for $N = 2 \cdot 10^6$.

With these two points, the line SG can be drawn in the diagram. This line expresses the fatigue life for a certain stress amplitude with a probability of 50%. To include the most of the possibilities, both σ_{aR} and $\sigma_{a\infty}$ must be divided for a factor of 1.6 according to Atzori. A new line S_dG_d is then created, being a translation of the SG line in the negative σ_a direction. The new stress values that define this line are:

$$\sigma_{aR_d} = \frac{\sigma_{aR}}{1.6} = 178.1MPa \tag{3.4.10}$$

$$\sigma_{a\infty_d} = \frac{\sigma_{a\infty}}{1.6} = 90MPa \tag{3.4.11}$$

These two values are indicated for a probability of survival of 97.5% ([6], paragraph 5.3). The inclination of the line S_dG_d is defined from the parameter k. This parameter can be found considering the linear relation between the logarithms of stress and number of cycles:

$$k = log_{\frac{\sigma_{aR}}{\sigma_{a\infty}}} \left(\frac{2 \cdot 10^6}{10^3} \right) = 11.14 \tag{3.4.12}$$

The general equation of the curve can be written as follows:

$$\frac{N_G}{N} = \left(\frac{\sigma_a}{\sigma_{a\infty_d}} \right)^k \tag{3.4.13}$$

where N is the number of cycle for a generic value of σ_a. Giving this last parameter the value obtained from the finite element analysis

$$\sigma_a = \frac{264}{2} = 132MPa$$

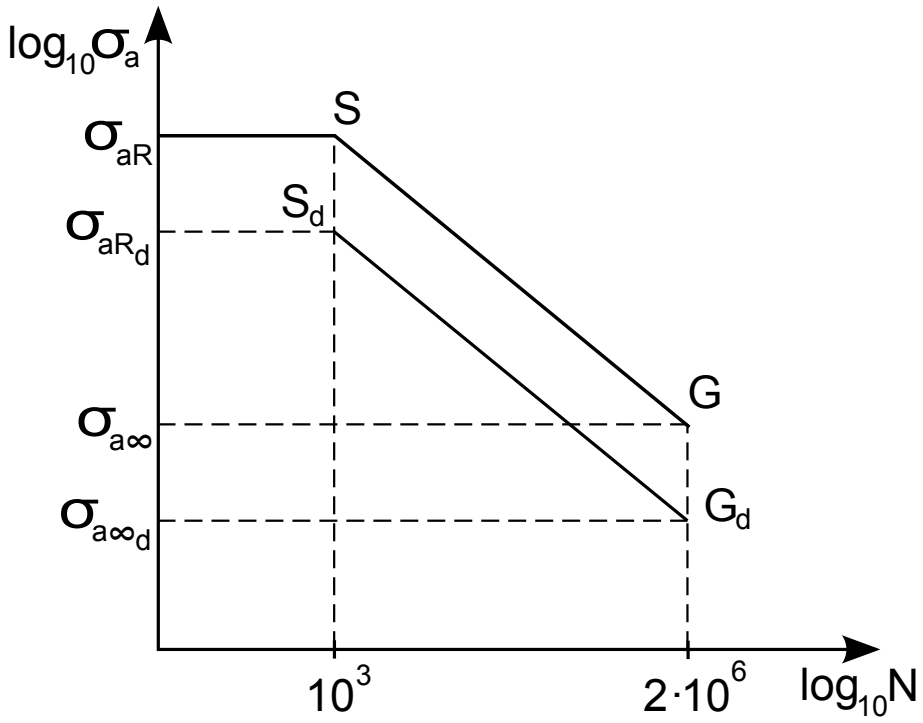

Figure 3.18: Woehler diagram of the component.

the fatigue life is obtained rearranging the 3.4.13:

$$N = \frac{N_G}{\left(\frac{\sigma_a}{\sigma_{a\infty_d}}\right)^k} = 2.8 \cdot 10^4$$

The estimated fatigue life is sufficiently far from the short-life value of 10^3. For this reason, the landing gear leg is expected to operate for a long time, and it is most probable that fatigue will interest other parts of the structure first (such as joints). These parts will require regular inspection, and possibly need to be replaced in the long time.

Chapter 4

Future developments

With the contribution of this work, the design of the Merlo is now close to be completed. However, some additional design and calculations must be carried out. In this short chapter, a list of possible future developments of this project is presented.

4.1 Center of gravity calculation

A very important step is the calculation of the center of gravity of the aircraft. It is necessary to know its location to place properly the wings, the landing gear, the tail and other components. To do it, it is necessary to know the mass and the location of each component with respect of the propeller edge. Thus, the calculation of the c.g. is an iterative process, that will be over only when all the components of the aircraft will be ready to be mounted to the fuselage. At the moment, the calculation is made guessing some of the weights and distances that now cannot be known. Table 4.1 shows the components of the Merlo, their mass, their position and the moment generated by their weight. The moment is calculated as the product of the weight for the distance. The position of the center of gravity is given by:

$$x_{cg} = \frac{\sum_i W_i x_i}{\sum_i W_i} = \frac{\sum_i M_i}{\sum_i W_i} \tag{4.1.1}$$

The values in table 4.1 give a value of $x_{cg} = 1617mm$. This is the horizontal distance calculated from the propeller edge to the center of gravity of the aircraft. If the pilot has a different weight from the value indicated here, the position of the c.g. does not vary significantly. In fact, a variation of $10kg$ in the pilot weight moves the c.g. forward ($-10kg$) or aft ($+10kg$) by just $8mm$. The values in the table must be updated when the components will be definitely designed or chosen.

	mass [kg]	weight [N]	distance [mm]	moment [Nmm]
Propeller	3	29.4	200	$5.880 \cdot 10^3$
Engine	20	196	352	$6.899 \cdot 10^4$
Engine cooler	1.5	14.7	352	$5.174 \cdot 10^3$
Fuel	7.5	73.5	1600	$1.176 \cdot 10^5$
Empty fuel tank	1	9.8	1600	$1.568 \cdot 10^4$
Engine Mount	1.25	12.25	447	$5.476 \cdot 10^3$
Flame retardant panel	0.67	6.54	535	$3.497 \cdot 10^3$
Wings	18	176.4	1620	$2.858 \cdot 10^5$
Pilot	80	784	1760	$1.380 \cdot 10^6$
Fuselage	12.68	124.26	2180	$2.709 \cdot 10^5$
GRS (Parachute system)	11.3	110.74	2400	$2.658 \cdot 10^5$
Back wheel	1	9.8	3900	$3.822 \cdot 10^4$
Tail	3	29.4	3700	$1.088 \cdot 10^5$
Landing gear	7	68.6	1300	$8.918 \cdot 10^4$
Instrumentation	0.5	4.9	1600	$7.840 \cdot 10^3$
Controls	5	49	1600	$7.840 \cdot 10^4$
Total	173.4	1700	-	$2.75 \cdot 10^6$

Table 4.1: Weight, position and moment generated with respect to the propeller edge of the components of the aircraft.

4.2 Aerodynamic developments

Most of the aerodynamics of Merlo have already been studied. However, some aspects may be developed. The pitch stability of the aircraft can be verified with a computational fluid analysis. Both yaw and roll stability can be verified with analytical calculation and with cfd.
An accurate estimate of drag can be done with the cfd, and some performance parameters can be calculated. The maximum speed of the aircraft can be calculated with respect to the chosen propeller type and engine characteristics. The gliding performance of the airplane can be further investigated, testing different wingtip shapes and then different wing surface areas to obtain a higher value of gliding ratio.
The control surfaces must be accurately sized and tested, in order to obtain the right moment that is necessary to make a maneuver in a specific time, according to the norm.

4.3 Structural developments

The structural analysis that has been presented here can be further developed both for wing and landing gear. A more detailed finite element model of the wing can be built, using a thicker mesh. This could be useful for the study of dynamic phenomena like flutter and divergence. A buckling analysis can be performed to investigate the possible failure of the ribs and the plywood reinforcements. The spar box and the spar-fuselage connection must be modeled, to obtain a more realistic behavior of the structure.
A more complete model of the landing gear can be made, modeling the connection to the fuselage. In addition, the contact between the gear and the ground can be made to evaluate the effective landing conditions. This may be done with an explicit dynamics analysis.
The control mechanics must be designed and tested. The required force applied by the pilot must not exceed some specific values given by the norm. The tail and its internal structure must be sized in detail, testing different load conditions. Asymmetric load conditions must be tested, according to the normative.

4.4 Other developments

The power system must be accurately designed and tested, including the fuel storage and transfer system. The required electronic devices must be defined and installed. Actually, the normative must be accurately read and all the aircraft components must be designed to respect it. Last, the flight manual of the airplane must be written.

Appendix A

Codes

Matlab Scripts

Longitudinal_equilibrium.m

This script calculates the airloads required to obtain the longitudinal equilibrium, according to Megson [20].

```
0001 % Matlab code for calculation of longitudinal equilibrium
0002 % According to Megson's Aircraft Structure for Engeneering students,
0003 % chapter 14
0004 clc; clear all; close all;
0005
0006 % Airspeed and load factor for the considered point in the V-n diagram
0007 v=51.31;
0008 n=-2;
0009
0010 W=180*9.81;
0011 AR=7.793; % Aspect ratio
0012 S=3.208;  % Nominal surface
0013 cm=0.665;
0014 lambdac4=3.68*(pi/180);
0015 rho=1.23;
0016 % geometry (referring to Megson, p412, fig 14.6)
0017 a=0.07;
0018 b=0;
0019 c=0;
0020 l=2.1-a;
0021 P=0;
```

```
0022 for i=1:3
0023 L=n*W-P;
0024 CL=(2*L)/(rho*v^2*S);
0025 Cl=CL/(0.9*cos(lambdac4))
0026 Cm=input('Cm =   (positive counterclockwise)  ');
0027 M0=0.5*rho*v^2*S*Cm*cm;
0028 T=D;
0029 P=(L*a-M0)/l;
0030 end
0031 P       % vertical load acting on the horizontal tail
0032 L=n*W-P % vertical load acting on wing
```

Spar.m

This script calculates maximum stress at a specified section for the main spar.

```
0001 format long
0002 syms z F
0003
0004 l=0.815;               % length of the cantilever beam
0005 w1=0.10;               % fixed end width
0006 w2=0.05;               % free end width
0007 Ef=10e9;               % Youngs moduli
0008 Eb=13e9;
0009 h=0.07;
0010 t_f=0.005;             % Fir beam thickness
0011 t_b=0.0012;            % Birch plywood thickness
0012
0013 % Stress calculation
0014 wz=z*(w2-w1)/1.8+w1;
0015 M=-F*(l-z);
0016 Ixf=2*((wz*t_f^3)/12+(h/2-t_f/2)^2*wz*t_f);
0017 Ixb=2*(t_b*h^3)/12;
0018 Eeq=Ef*Ixf+Eb*Ixb;
0019
0020 F=4000;
0021
0022 z=0.6;
0023 s_max_f=-Ef*eval(M)*(h/2)/eval(Eeq) % Max stress on the fir beam
0024 s_max_b=-Eb*eval(M)*(h/2)/eval(Eeq) % Max stress on the birch reinforcement
```

Gear_leg.m

This script calculates the stroke of the landing gear leg and the maximum stress at a specified section.

```
0001 close all; clc; clear all;
0002 format long
0003 syms z F
0004
0005 h=0.566;                      % height from the ground
0006 alpha=0*pi/180;               % side side angle
0007 beta=35*pi/180;               % leg front angle
0008 l=h/(cos(beta)*cos(alpha)); % length of the cantilever beam
0009 w1=0.13;                      % fixed end width
0010 w2=0.05;                      % free end width
0011 E=71.7e9;                     % Youngs modulus
0012 t=0.013;                      % constant thickness of beam
0013 s_yeld=500e6;                % yield strength
0014
0015 mass=(l*t*(w1+w2)/2+0.0127^2*pi*0.09)*2780;
0016
0017 wz=z*(w2-w1)/l+w1;                % beam width as a function of length
0018 Mx=-F*(l-z)*sin(beta)*cos(alpha); % x Moment
0019 My=-F*(l-z)*cos(beta)*sin(alpha); % y Moment
0020 Mz=-F*(l-z)*sin(beta)*sin(alpha); % z Moment
0021 Ix=wz*t^3/12;
0022
0023 % Calculation of the displacement at free end
0024 Ubendingx=(Mx^2)/(2*E*Ix);
0025 Ux=int(Ubendingx,z,0,l);
0026 dispx=diff(Ux,F);
0027
0028 F=2700; % Force acting at the free end
0029 dispxmax=eval(dispx)/sin(beta);
0030 TotalStroke=eval(dispx)
0031
0032 % Calculation of maximum stress on the section
0033 z=0;
0034 x=w1/2;
0035 y=t/2;
0036 sigma_max=-(eval(Mx)*y)/eval(Ix)-(eval(My)*x)/eval(Iy) % Direct stress
```

```
0037 It=w1*t^3/3*(1-0.63*t/w1);
0038 tau_max=-eval(Mz)/It*t % Shear stress
0039 s_max=sqrt(sigma_max^2+3*tau_max^2) % Von Mises Equivalent stress
0040 n=s_max/s_yeld  % Safety factor
```

APDL input files

Wing FEM Analysis

```
0001 FINISH
0002 /CLEAR,START
0003
0004 !----------PREPROCESSING PHASE----------
0005
0006 /PREP7
0007
0008 !--Import the parasolid geometry file--
0009 ~PARAIN,'wingAssembly','x_t','.\Desktop\',SURFACES,0,0
0010 /NOPR
0011 /GO
0012
0013 /PNUM,AREA,1
0014 /REPLOT
0015 NUMMRG,KP,,1e-4
0016 /REPLOT
0017
0018 !--------Material Data--------
0019
0020 !---Silver Fir wood---
0021 !---Wood directions: XYZ=TRL
0022 MPTEMP,1,0
0023 MPDATA,EX,1,,10e9
0024 MPDATA,EY,1,,0.35e9
0025 MPDATA,EZ,1,,1.07e9
0026 MPDATA,PRXY,1,,0.33
0027 MPDATA,PRYZ,1,,0.33
0028 MPDATA,PRXZ,1,,0.33
0029 MPDATA,GXY,1,,0.82e9
0030 MPDATA,GYZ,1,,0.07e9
0031 MPDATA,GXZ,1,,0.67e9
```

```
0032 MPDATA,DENS,1,,400
0033
0034 !---Birch--
0035 !---Wood directions: XYZ=RTL
0036 MPDATA,EX,2,,13e9
0037 MPDATA,EY,2,,0.75e9
0038 MPDATA,EZ,2,,1.17e9
0039 MPDATA,PRXY,2,,0.451
0040 MPDATA,PRYZ,2,,0 !.426
0041 MPDATA,PRXZ,2,,0 !.697
0042 MPDATA,GXY,2,,1.02e9
0043 MPDATA,GYZ,2,,0.255e9
0044 MPDATA,GXZ,2,,1.11e9
0045 MPDATA,DENS,2,,720
0046
0047 !---Flexifoam--
0048 MPDATA,EX,3,,0.108e9
0049 MPDATA,PRXY,3,,0.49
0050 MPDATA,DENS,3,,130
0051
0052 !---Carbon Roving--
0053 MPDATA,EX,4,,80e9
0054 MPDATA,PRXY,4,,0.33
0055 MPDATA,DENS,4,,1600
0056
0057 !---Aluminium--
0058 MPDATA,EX,5,,70e9
0059 MPDATA,PRXY,5,,0.33
0060 MPDATA,DENS,5,,2780
0061
0062 !---Glass Fiber--
0063 MPDATA,EX,6,,15.8e9
0064 MPDATA,EY,6,,4e9
0065 !MPDATA,EZ,6,,4e9
0066 !MPDATA,PRXZ,6,,0.24
0067 MPDATA,PRXY,6,,0.24
0068 !MPDATA,PRYZ,6,,0.24
0069 MPDATA,GXY,6,,4.14e9
0070 MPDATA,GYZ,6,,3.9e9
0071 MPDATA,GXZ,6,,3.9e9
```

```
0072 MPDATA,DENS,6,,1630
0073
0074 !--------Define Elements & Sections--------
0075 !--Carbon Pipe---
0076 ET,1,BEAM188
0077 KEYOPT,1,1,0
0078 KEYOPT,1,2,0
0079 KEYOPT,1,3,2
0080 KEYOPT,1,4,0
0081 KEYOPT,1,6,0
0082 KEYOPT,1,7,0
0083 KEYOPT,1,9,0
0084 KEYOPT,1,11,0
0085 KEYOPT,1,12,0
0086 KEYOPT,1,15,0
0087
0088 SECTYPE,   1, BEAM, CTUBE, CarbonPipe, 0
0089 SECOFFSET, CENT
0090 SECDATA,0.019,0.02,0,0,0,0,0,0,0,0,0,0
0091
0092 SECTYPE,   4, BEAM, CSOLID, Perno, 0
0093 SECOFFSET, CENT
0094 SECDATA,0.012,0,0,0,0,0,0,0,0,0,0,0
0095
0096 !--Shell 181---
0097 ET,2,SHELL181
0098 KEYOPT,2,1,0
0099 KEYOPT,2,3,0
0100 KEYOPT,2,8,0
0101 KEYOPT,2,9,0
0102
0103 SECT,2,SHELL,,LongPrinc0
0104 SECDATA, 0.005,1,0.0,3
0105 SECOFFSET,MID
0106 SECCONTROL,,,, , , ,
0107
0108 SECT,21,SHELL,,LongPrinc1
0109 SECDATA, 0.01,1,0.0,3
0110 SECOFFSET,MID
0111 SECCONTROL,,,, , , ,
```

```
0112
0113 SECT,22,SHELL,,LongPrinc2
0114 SECDATA, 0.015,1,0.0,3
0115 SECOFFSET,MID
0116 SECCONTROL,,,, , , ,
0117
0118 SECT,23,SHELL,,LongPrinc3
0119 SECDATA, 0.020,1,0.0,3
0120 SECOFFSET,MID
0121 SECCONTROL,,,, , , ,
0122
0123 SECT,24,SHELL,,LongPrinc4
0124 SECDATA, 0.025,1,0.0,3
0125 SECOFFSET,MID
0126 SECCONTROL,,,, , , ,
0127
0128 SECT,3,SHELL,,Ribs
0129 SECDATA, 0.01,1,0.0,3
0130 SECOFFSET,MID
0131 SECCONTROL,,,, , , ,
0132
0133 SECT,5,SHELL,,BirchPly
0134 SECDATA, 0.0005,2,0,3
0135 SECDATA, 0.0005,2,90,3
0136 SECDATA, 0.0005,2,0,3
0137 SECOFFSET,MID
0138 SECCONTROL,0,0,0, 0, 1, 1, 1
0139
0140 SECT,6,SHELL,,Skin
0141 SECDATA, 0.00008,6,0,3
0142 SECDATA, 0.00008,6,45,3
0143 SECDATA, 0.00008,6,-45,3
0144 SECDATA, 0.00008,6,90,3
0145 SECDATA, 0.005,3,0,3
0146 SECDATA, 0.00008,6,90,3
0147 SECDATA, 0.00008,6,-45,3
0148 SECDATA, 0.00008,6,45,3
0149 SECDATA, 0.00008,6,0,3
0150 SECOFFSET,MID
0151 SECCONTROL,0,0,0, 0, 1, 1, 1
```

```
0152
0153 !----Add Keypoints
0154 !--LongAnt
0155 K,3001,1.73094,-0.27174,-0.208100
0156 K,3002,1.69372,-0.19297,-2.10600
0157 L,3001,3002,38
0158 K,3003,1.69176,-0.18883,-2.2059
0159 L,3002,3003,5
0160
0161 !--LongTip
0162 K,3004,1.48666,-0.2057,-1.652
0163 K,3005,1.47258,-0.18569,-2.35163
0164 L,3004,3005,14
0165
0166 !--Creating hardpoints to merge the beam nodes with the rib nodes
0167 HPTCREATE,AREA,338,0,COORD,1.72898,-0.26759,-0.3079
0168 HPTCREATE,AREA,349,0,COORD,1.72604,-0.26137,-0.45774
0169 HPTCREATE,AREA,360,0,COORD,1.7231,-0.25515,-0.60758
0170 HPTCREATE,AREA,371,0,COORD,1.72016,-0.24894,-0.75742
0171 HPTCREATE,AREA,382,0,COORD,1.71723,-0.24272,-0.90726
0172 HPTCREATE,AREA,393,0,COORD,1.71429,-0.2365,-1.05711
0173 HPTCREATE,AREA,404,0,COORD,1.71135,-0.23028,-1.20695
0174 HPTCREATE,AREA,415,0,COORD,1.70841,-0.22406,-1.35679
0175 HPTCREATE,AREA,426,0,COORD,1.70547,-0.21785,-1.50663
0176 HPTCREATE,AREA,437,0,COORD,1.70253,-0.21163,-1.65648
0177 HPTCREATE,AREA,448,0,COORD,1.6996,-0.20541,-1.80632
0178 HPTCREATE,AREA,459,0,COORD,1.69699,-0.19919,-1.95616
0179 HPTCREATE,AREA,478,0,COORD,1.69372,-0.19297,-2.106
0180 HPTCREATE,AREA,1,0,COORD,1.69176,-0.18883,-2.2059
0181 HPTCREATE,AREA,439,0,COORD,1.48666,-0.2057,-1.652
0182 HPTCREATE,AREA,450,0,COORD,1.48364,-0.20141,-1.80192
0183 HPTCREATE,AREA,461,0,COORD,1.48063,-0.19713,-1.95184
0184 HPTCREATE,AREA,470,0,COORD,1.47761,-0.19284,-2.10176
0185 HPTCREATE,AREA,1,0,COORD,1.4756,-0.18998,-2.20171
0186 HPTCREATE,AREA,2,0,COORD,1.47258,-0.18569,-2.35163
0187
0188
0189 !------MESH-----
0190 !--Meshing Carbon Pipes--
0191 LSEL,S,,,7
```

```
0192 LSEL,A,,,9
0193 LATT,4,,1,,,,1
0194 LMESH,ALL
0195
0196 !--Meshing Axle--
0197 LSEL,ALL
0198 LSEL,S,,,8
0199 LATT,5,,1,,,,4
0200 LMESH,ALL
0201
0202 ALLSEL,ALL
0203
0204 !--Meshing Spars--
0205 !--Areas Defining the ribs--
0206 ASEL,U,,,338,478
0207 ASEL,U,,,1,3
0208
0209 !--Areas Defining the plywood renforcements--
0210 ASEL,U,,,286,337
0211
0212 !--Areas Defining the skin--
0213 ASEL,U,,,4,9
0214 ASEL,U,,,190,237
0215 ASEL,U,,,142,165
0216
0217 APLOT
0218
0219 !--Local coordinate system
0220 CSKP,11,0,26,151,24,1,1,
0221
0222 ASEL,S,,,11
0223 ASEL,A,,,14
0224 AATT,1,,2,11,24
0225 ASEL,A,,,141
0226 ASEL,A,,,129
0227 AATT,1,,2,11,24
0228 ASEL,S,,,140
0229 ASEL,A,,,128
0230 AATT,1,,2,11,23
0231 ASEL,S,,,139
```

```
0232 ASEL,A,,,127
0233 AATT,1,,2,11,22
0234 ASEL,S,,,136,138
0235 ASEL,A,,,124,126
0236 AATT,1,,2,11,21
0237
0238 ASEL,S,,,118,123
0239 ASEL,A,,,130,135
0240 ASEL,A,,,166,189
0241 ASEL,A,,,17
0242 ASEL,A,,,20
0243 AATT,1,,2,11,2
0244
0245 ASEL,S,,,118,141
0246 ASEL,A,,,166,189
0247 ASEL,A,,,11
0248 ASEL,A,,,14
0249 ASEL,A,,,17
0250 ASEL,A,,,20
0251 LSLA,S
0252 LPLOT
0253 LESIZE,ALL,0.06
0254 AMESH,ALL
0255 EPLOT
0256
0257 ALLSEL,ALL
0258
0259 ASEL,S,,,10
0260 ASEL,A,,,12,13
0261 ASEL,A,,,15,16
0262 ASEL,A,,,18,19
0263 ASEL,A,,,21
0264 ASEL,A,,,93,94
0265 ASEL,A,,,69,70
0266 ASEL,A,,,117
0267 ASEL,A,,,33
0268 ASEL,A,,,57
0269 ASEL,A,,,45
0270
0271 LSLA,S
```

```
0272 LPLOT
0273 LESIZE,ALL,0.06
0274 AATT,1,,2,11,2
0275 AMESH,ALL
0276
0277 ALLSEL,ALL
0278 ASEL,U,,,338,478
0279 ASEL,U,,,1,3
0280 ASEL,U,,,286,337
0281 ASEL,U,,,4,9
0282 ASEL,U,,,190,237
0283 ASEL,U,,,142,165
0284 ASEL,U,,,10
0285 ASEL,U,,,12,13
0286 ASEL,U,,,15,16
0287 ASEL,U,,,18,19
0288 ASEL,U,,,21
0289 ASEL,U,,,118,141
0290 ASEL,U,,,166,189
0291 ASEL,U,,,11
0292 ASEL,U,,,14
0293 ASEL,U,,,17
0294 ASEL,U,,,20
0295 ASEL,U,,,93,94
0296 ASEL,U,,,69,70
0297 ASEL,U,,,117
0298 ASEL,U,,,33
0299 ASEL,U,,,57
0300 ASEL,U,,,45
0301 LSLA,S
0302 LPLOT
0303 LESIZE,ALL,0.06
0304
0305 CSKP,12,0,151,153,152,1,1,
0306
0307 AATT,1,,2,12,2
0308 AMESH,ALL
0309 ALLSEL,ALL
0310
0311 !--Meshing Plywood--
```

```
0312 ASEL,S,,,286,337
0313 ASEL,A,,,22,117
0314 ASEL,A,,,15,16
0315 ASEL,A,,,18,19
0316 ASEL,A,,,10
0317 ASEL,A,,,12,13
0318 ASEL,A,,,21
0319
0320 LSLA,S
0321 LPLOT
0322 LESIZE,ALL,0.06
0323 AATT,2,,2,12,5
0324 AMESH,ALL
0325 ALLSEL,ALL
0326 /PSYMB,ESYS,1
0327 EPLOT
0328
0329 !--Meshing Ribs--
0330 ASEL,S,,,338,478
0331 ASEL,A,,,1,3
0332
0333 APLOT
0334 LSLA,S
0335 LSEL,A,,,19
0336 LSEL,A,,,11
0337 LPLOT
0338 LESIZE,ALL,0.05
0339 AATT,3,,2,,3
0340 AMESH,ALL
0341 ALLSEL,ALL
0342
0343 !--Meshing Skin--
0344 CSYS,0
0345
0346 !--Creating hardpoints to merge the wing and tip nodes
0347 HPTCREATE,LINE,19,,COORD,1.4233611528,-0.1738902630,-2.0999118295
0348 HPTCREATE,LINE,19,,COORD,1.3929719411,-0.1827964540,-2.0996856515
0349 HPTCREATE,LINE,19,,COORD,1.4535845148,-0.1689749318,-2.1003002916
0350 HPTCREATE,LINE,19,,COORD,1.5037796956,-0.1650440318,-2.1011210103
0351 HPTCREATE,LINE,19,,COORD,1.5499322415,-0.1642798537,-2.1019938488
```

```
0352 HPTCREATE,LINE,19,,COORD,1.5960609514,-0.1659578706,-2.1029675184
0353 HPTCREATE,LINE,19,,COORD,1.6420323651,-0.1700848687,-2.1040396851
0354 HPTCREATE,LINE,19,,COORD,1.6877345759,-0.1765417811,-2.1052032169
0355 HPTCREATE,LINE,19,,COORD,1.7331495307,-0.1847768951,-2.1064348758
0356 HPTCREATE,LINE,19,,COORD,1.7782814819,-0.1944414000,-2.1077202770
0357 HPTCREATE,LINE,11,,COORD,1.4215989277,-0.2162948897,-2.1016361685
0358 HPTCREATE,LINE,11,,COORD,1.3916664265,-0.2142112039,-2.1009630989
0359 HPTCREATE,LINE,11,,COORD,1.4515705504,-0.2174371890,-2.1022709576
0360 HPTCREATE,LINE,11,,COORD,1.5015736274,-0.2181289055,-2.1032796501
0361 HPTCREATE,LINE,11,,COORD,1.7772458967,-0.2039172619,-2.1080930244
0362 HPTCREATE,LINE,11,,COORD,1.7312631795,-0.2056718917,-2.1072645968
0363 HPTCREATE,LINE,11,,COORD,1.6853623322,-0.2089979205,-2.1065029528
0364 HPTCREATE,LINE,11,,COORD,1.6394902273,-0.2127113841,-2.1057579423
0365 HPTCREATE,LINE,11,,COORD,1.5935694602,-0.2157443535,-2.1049837523
0366 HPTCREATE,LINE,11,,COORD,1.5475885891,-0.2176328511,-2.1041609135
0367
0368 ASEL,S,,,4,9
0369 ASEL,A,,,118,237
0370 LSEL,S,,,568,579
0371 LSEL,A,,,16,18
0372 LSEL,A,,,585,596
0373 LSEL,A,,,12,14
0374
0375 LESIZE,ALL,0.05
0376
0377 AATT,6,,2,,6
0378 AMESH,ALL
0379 ALLSEL,ALL
0380 NUMMRG,NODES
0381
0382 !---Fluid Solid Interface--
0383 !--Selecting the skin elements
0384
0385 !ASEL,S,,,4,9
0386 !ASEL,A,,,118,237
0387 !ESLA,S
0388 !NSLE,S
0389 !LSLA,S
0390 !KSLL,S
0391
```

```
0392 !--Writing the mesh to be imported into FLUENT--
0393
0394 ! CDWRITE,DB,Wing_surf,cdb,
0395
0396 !-------LOADS------
0397 /FACET,NORML
0398 !---Constraints--
0399 ASEL,S,,,10,21,
0400 ASEL,A,,,286,289,
0401 DA,ALL,UX
0402 DA,ALL,UY
0403
0404 LSEL,S,,,23
0405 LSEL,A,,,26
0406 LSEL,A,,,30
0407 LSEL,A,,,40
0408 LSEL,A,,,33
0409 LSEL,A,,,36
0410 LSEL,A,,,762
0411 LSEL,A,,,758
0412
0413 DL,ALL,,ALL
0414 ALLSEL,ALL
0415
0416 DK,3001,ALL
0417
0418 !---PRESSURE LOAD---
0419
0420 /INPUT,'loadA','cdb','.\Desktop\',, 0
0421 /PSYMB,ESYS,0
0422
0423 !------------SOLUTION PHASE------------
0424 FINISH
0425 /SOL
0426 ANTYPE,0
0427 /STATUS,SOLU
0428 SOLVE
0429
0430 /POST1
0431 PRNSOL,U,COMP
```

```
0432 PLDISP,2
0433
0434 !----------Structure Plot--------
0435 !---------POSTPROCESSING PHASE------
0436 !----Results for the Spars----
0437 ESEL,S,MAT,,1
0438 ESEL,A,MAT,,2
0439 PLNSOL, S,EQV, 0,1.0
0440
0441 !----Results for the Plywood----
0442 PLNSOL, S,EQV, 0,1.0
0443
0444 !----Results for the Ribs----
0445 ESEL,S,MAT,,3
0446 PLNSOL, S,EQV, 0,1.0
0447
0448 !----Results for Skin----
0449 ESEL,S,MAT,,6
0450 PLNSOL, S,EQV, 0,1.0
0451
0452 !----Results for the Beams----
0453 ESEL,A,TYPE,,1
0454
0455 /SHRINK,0
0456 /ESHAPE,1
0457 /EFACET,1
0458 /RATIO,1,1,1
0459 /CFORMAT,32,0
0460 /REPLOT
0461 PLNSOL, S,EQV, 0,1.0
```

Landing gear leg FEM analysis, beam model

This input file performs a non-linear analysis on the landing gear leg modeled with beam elements. To perform a linear analysis, it is enough to change the solver type in the solution phase.

```
0001 FINISH
0002 /CLEAR,START
0003
0004 !----------PREPROCESSING PHASE----------
```

```
0005 /PREP7
0006 *SET,h,0.65
0007 *SET,alpha,0*3.1415/180
0008 *SET,beta,30*3.1415/180
0009 *SET,l,h/(cos(beta)*cos(alpha))
0010 *SET,t1,0.02
0011 *SET,t2,0.015
0012 *SET,w1,0.08
0013 *SET,w2,0.03
0014
0015 !----------Element Data----------
0016 ET,1,BEAM188
0017 KEYOPT,1,3,2
0018 SECTYPE,   1, BEAM, RECT, , 0   !--Large section
0019 SECOFFSET, CENT
0020 SECDATA,t1,w1,0,0,0,0,0,0,0,0,0,0  !--Base,Height
0021 SECTYPE,   2, BEAM, RECT, , 0   !--Small section
0022 SECOFFSET, CENT
0023 SECDATA,t2,w2,0,0,0,0,0,0,0,0,0,0  !--Base,Height
0024 SECTYPE,3,TAPER, ,taper         !--Taper section
0025 SECDATA,1,0,0,0
0026 SECDATA,2,l*cos(alpha)*sin(beta),-l*cos(alpha)*cos(beta),l*sin(alpha)
0027 SECTYPE,   4, BEAM, CSOLID, , 0 !--Axle section
0028 SECOFFSET, CENT
0029 SECDATA,0.0127,0,0,0,0,0,0,0,0,0,0,0
0030
0031 !----------Material Data----------
0032 !--Aluminium 2024-T3---
0033 MPTEMP,,,,,,,,
0034 MPTEMP,1,0
0035 MPDATA,EX,1,,73.1e9
0036 MPDATA,PRXY,1,,0.33
0037 MPDATA,DENS,1,,2780
0038
0039 !----------Creating Keypoints----------
0040 K,1,0,0,0
0041 K,2,l*cos(alpha)*sin(beta),-l*cos(alpha)*cos(beta),l*sin(alpha)
0042 K,3,l*cos(alpha)*sin(beta)+0.09,-l*cos(alpha)*cos(beta),l*sin(alpha)
0043
0044 !----------Creating Lines----------
```

```
0045 L,1,2,20
0046 L,2,3,6
0047
0048 !----------Mesh----------
0049 LSEL,S,,,1
0050 LATT,1,2,1,,,,3
0051 LSEL,S,,,2
0052 LATT,1,2,1,,,,4
0053 LSEL,ALL
0054 LMESH,ALL
0055
0056 !---------Boundary conditions----------
0057 DK,1, , , ,0,ALL, , , , , ,
0058
0059 !---------Loads----------
0060 FK,2,FY,2700/2
0061 FK,3,FY,2700/2
0062
0063 !------------SOLUTION PHASE------------
0064 FINISH
0065 /SOL
0066 ANTYPE,0
0067 NLGEOM,ON
0068
0069 AUTOTS,ON
0070 NSUBST,5,1000,1
0071 OUTRES,ALL,ALL
0072
0073 SOLVE
0074
0075 FINISH
0076 /POST1
0077 PRNSOL,U,COMP
0078 PLDISP,2
0079
0080 !----------Structure Plot--------
0081 /SHRINK,0
0082 /ESHAPE,1
0083 /EFACET,1
0084 /RATIO,1,1,1
```

```
0085 /CFORMAT,32,0
0086 /REPLOT
0087 PLNSOL,S,EQV, 0,1.0
```

Landing gear leg FEM analysis, shell model

This input file performs a non-linear analysis on the landing gear leg modeled with shell elements. To perform a linear analysis, it is enough to change the solver type in the solution phase.

```
0001 FINISH
0002 /CLEAR,START
0003 !----------PREPROCESSING PHASE----------
0004 /PREP7
0005 *SET,h,0.566
0006 *SET,alpha,0*3.1415/180
0007 *SET,beta,35*3.1415/180
0008 *SET,delta,0*3.1415/180
0009 *SET,l,h/(cos(beta)*cos(alpha))
0010 *SET,t1,0.018
0011 *SET,t2,0.013
0012 *SET,w1,0.11
0013 *SET,w2,0.05
0014 !----------Element Data----------
0015 ET,1,SHELL181
0016 KEYOPT,1,3,2
0017 ET,2,BEAM188
0018 KEYOPT,1,3,2
0019 !----------Material Data----------
0020 !--Aluminium 2024-T3---
0021 MPTEMP,,,,,,,,
0022 MPTEMP,1,0
0023 MPDATA,EX,1,,71.7e9
0024 MPDATA,PRXY,1,,0.33
0025 MPDATA,DENS,1,,2780
0026 !----------Sections----------
0027
0028 *dim,tapered,table,2,,,x
0029 tapered(1,0)=0,l*cos(alpha)*sin(beta)
0030 tapered(1,1)=t1,t2
0031 SECTYPE,1,SHELL,,
```

```
0032 SECDATA, t1,1,0.0,3
0033 SECOFFSET,MID
0034 SECFUNCTION,%tapered%
0035
0036 SECTYPE,   2, BEAM, CSOLID, , 0 !--Axle section
0037 SECOFFSET, CENT
0038 SECDATA,0.0127,0,0,0,0,0,0,0,0,0,0,0
0039
0040 !----------Creating Keypoints----------
0041 K,1,0,0,w1/2
0042 K,2,0,0,-w1/2
0043 K,3,l*cos(alpha)*sin(beta),-l*cos(alpha)*cos(beta),l*sin(alpha)+w2/2
0044 K,4,l*cos(alpha)*sin(beta),-l*cos(alpha)*cos(beta),l*sin(alpha)-w2/2
0045 K,5,l*cos(alpha)*sin(beta),-l*cos(alpha)*cos(beta)-0.05,l*sin(alpha)+w2/2
0046 K,6,l*cos(alpha)*sin(beta),-l*cos(alpha)*cos(beta)-0.05,l*sin(alpha)-w2/2
0047 K,7,l*cos(alpha)*sin(beta),-l*cos(alpha)*cos(beta)-0.05/2,l*sin(alpha)
0048 K,8,l*cos(alpha)*sin(beta)+0.09*cos(delta),...

-l*cos(alpha)*cos(beta)-0.09*sin(delta)-0.05/2,l*sin(alpha)
0049
0050 !----------Creating Lines----------
0051 L,1,2,2
0052 L,3,4,2
0053 L,2,4,20
0054 L,3,1,20
0055 AL,1,3,2,4
0056 L,3,5,2
0057 L,4,6,2
0058 L,5,6,2
0059 AL,2,5,7,6
0060 L,7,8,6
0061 !----------Mesh----------
0062
0063 AMESH,ALL
0064 LSEL,S,,,8
0065 LATT,1,,2,,,,2
0066 LMESH,ALL
0067 LSEL,ALL
0068 NUMMRG,NODES
0069
```

```
0070 /SHRINK,0
0071 /ESHAPE,1
0072 /EFACET,1
0073 /RATIO,1,1,1
0074 /CFORMAT,32,0
0075 /REPLOT
0076 !---------Boundary conditions----------
0077 D,1,ALL
0078 D,2,ALL
0079 D,3,ALL
0080 !---------Loads----------
0081 F,74,FY,2700
0082 !------------SOLUTION PHASE------------
0083 FINISH
0084 /SOL
0085 ANTYPE,0
0086 NLGEOM,ON
0087
0088 AUTOTS,ON
0089 NSUBST,10,1000,1
0090 OUTRES,ALL,ALL
0091
0092 SOLVE
0093
0094 FINISH
0095 /POST1
0096 PRNSOL,U,COMP
0097 PLDISP,2
0098 PLNSOL,S,EQV, 0,1.0
```

Bibliography

[1] Ron Alexander, *Aircraft Wood*, Sport Aviation, December 1998. `http://www.sportair.com/articles`

[2] US Army-Navy-Civil Committee, *Design of Wood Aircraft Structures*, ANC Bulletin 18, June 1944.

[3] John D. Anderson Jr., *Aircraft Performance and Design*, WCB/McGraw-Hill, 1999.

[4] John D. Anderson Jr., *Fundamentals of Aerodynamics*, 3rd ed., McGraw-Hill, 2001.

[5] ANSYS Inc. ANSYS Help Manual, Release 14.0, 2011.

[6] B. Atzori, *Appunti di Costruzioni di Macchine*, Edizioni Libreria Cortina, Padova 1999.

[7] D. Baldon, *Design e Validazione Strutturale Fusoliera di Aereo Ultraleggero*, Tesi di laurea magistrale in Ingegneria Aerospaziale, Padova 2013.

[8] Decreto del Presidente della Repubblica, 9 luglio 2010, n. 133. Nuovo regolamento di attuazione della legge 25 marzo 1985, n. 106, concernente la *Disciplina del Volo da Diporto o Sportivo*.

[9] Federal Aviation Administration, *Federal Aviation Regulations*, Title 14 of the Code of Federal Regulations.

[10] F. Ferus, *Calcolo dei Carichi Aerodinamici e Verifica Strutturale di un Aereo Ultraleggero.*, Tesi di laurea magistrale in Ingegneria Aerospaziale, Padova 2013.

[11] ANSYS Inc. Fluent Theory Guide, Release 14.0, 2011.

[12] Forest Products Laboratory, *Wood handbook - Wood as an engineering material*. General Technical Report FPL-GTR-190, April 2010.

[13] L. Gori, *Progetto e Verifica di Alcuni Componenti Strutturali di un Velivolo Ultraleggero*, Tesi di laurea magistrale in Ingegneria Aerospaziale, Padova 2013.

[14] S. F. Hoerner, *Fluid-Dynamic Drag. Theoretical, Experimental and Statistical Information*, 1965.

[15] Helmut Quabeck's website, `www.hq-modellflug.de/`.

[16] A.K. Kundu, *Aircraft Design*, Cambridge University Press, 2010.

[17] A. Lausetti, *L' aeroplano. Progetto, strutture, installazioni*, Levrotto e Bella.

[18] S. Lenci, *Lezioni di Meccanica Strutturale*, Seconda Edizione, Pitagora Editrice, Bologna 2009.

[19] MatWeb website, `http://www.matweb.com`.

[20] T. H. G. Megson, *Aircraft Structures for Engineering Students*, 4th ed., Butterworth-Heinemann, 2007.

[21] T. H. G. Megson, *Structural and Stress Analysis*, Butterworth-Heinemann, 1996.

[22] Profili2 website, `www.profili2.com`.

[23] J. Ramsay and E. Macdonald, *Timber Properties of Minor Conifer Species. A report to the Forestry Commission*, Research Agency of the Forestry Commission, UK, May 2013.

[24] Daniel P. Raymer, *Aircraft Design: A Conceptual Approach*, 4th ed., AIAA Education Series, American Institute of Aeronautics and Astronautics, 2006.

[25] Xfoil website, `http://web.mit.edu/drela/Public/web/xfoil`.